THESIS FOR THE DEGREE OF DOCTOR OF PHILOSOPHY

PHOTOINDUCED ELECTRON AND ENERGY TRANSFER IN Π–CONJUGATED SYSTEMS

MÉLINA GILBERT GATTY

CHALMERS

DEPARTMENT OF CHEMISTRY AND CHEMICAL ENGINEERING
CHALMERS UNIVERSITY OF TECHNOLOGY
GOTHENBURG, SWEDEN 2015

Photoinduced Electron and Energy Transfer in Π–Conjugated Systems
Mélina Gilbert Gatty
ISBN: 978-91-7597-219-0

Doktorsavhandlingar vid Chalmers tekniska högskola
Ny serie nr 3900
ISSN 0346-718X

Department of Chemistry and Chemical Engineering
Chalmers University of Technology
SE-412 96 Gothenburg
Sweden
Telephone + 46 (0)31-772 1000

Front cover: Four different aspects of photoinduced electron and energy transfer in π–conjugated systems mimics of the natural photosynthetic complexes are covered in this thesis. Going from the top left hand corner to the bottom right hand corner are illustrations of: control of electron transfer in a porphyrin hexamer–fullerene dyad, a self–assembled porphyrin tetramer–fullerene dimeric array, electron transfer mediated by a porphyrin bridge in a donor–bridge–acceptor system and a schematic structure of an anthracene dendrimer model system for fast exciton migration.

Back cover: Photograph by Peter Sandin.

Printed by Chalmers Reproservice
Gothenburg, Sweden 2015

A MES PARENTS, FRANÇOISE ET DIDIER,

PHOTOINDUCED ELECTRON AND ENERGY TRANSFER IN Π–CONJUGATED SYSTEMS

MÉLINA GILBERT GATTY
Department of Chemistry and Chemical Engineering
Chalmers University of Technology

ABSTRACT

Photosynthesis is a fascinating process that provides food and oxygen. In this thesis, focus is on understanding and controlling the early processes of photosynthesis, namely photoinduced energy and electron transfer. Indeed, mimicking these processes in synthetic systems could open to a wide range of applications going from renewable energy production to molecular devices for information exchange. In this work, covalently linked π–conjugated systems provide a means to get a better understanding of the mechanisms and factors that govern transfer of charge and energy in molecular systems.

Photoinduced electron transfer (ET) is investigated in series of donor–acceptor dyads $\mathbf{P_n–C_{60}}$ and triads $\mathbf{Fc–P_n–C_{60}}$ employing butadiyne–linked zinc porphyrin oligomers denoted $\mathbf{P_n}$ (n = 1–8) as photoactive electron donor and π–conjugated bridging structures (wires). In the triads, temperature dependence study of the recombination of the long–range charge separated state $\mathbf{Fc^{\bullet+}–P_n–C_{60}^{\bullet-}}$ provides new insights into the mechanistic nature of the charge transport linked to its wire–like behavior. At high temperatures (> 280 K), the weakly distance–dependent charge transport arises from coherent electron tunneling for the entire series. At low temperatures, crossover to incoherent hole hopping accompanied by a stronger distance dependence of the charge transport is observed in long $\mathbf{Fc–P_n–C_{60}}$ (n = 2–4). Being able to tune the ET rate in donor–acceptor systems is another property which is highly desirable for applications of molecules in actual devices. Here, in the long $\mathbf{P_n–C_{60}}$ (n = 4, 6) dyads, we demonstrate the possibility of varying the rate of electron transfer between the photoexcited porphyrin oligomer ($\mathbf{^1P_n^*}$) and the fullerene ($\mathbf{C_{60}}$) by either optical or chemical control of the conformation of the porphyrin chain. Additionally, we show that temperature could potentially be used to control the conformation of the porphyrin oligomer. Below 170 K, all studied systems $\mathbf{P_n}$, $\mathbf{P_n–C_{60}}$ and $\mathbf{Fc–P_n–C_{60}}$ spontaneously form highly–ordered planar aggregates.

The thesis also discusses photoinduced excitation energy transfer (EET) in the $\mathbf{P_n}$ systems and two anthracene dendrimers. In the latter, despite weak through–bond electronic coupling, signs of an ultrafast EET between the anthracene dendrons are observed by time–resolved fluorescence anisotropy. For the $\mathbf{P_n}$ systems, pump intensity–dependent transient absorption measurements reveal at early times (< 30 ps) singlet–singlet annihilation that is the characteristic of partially coupled systems.

Keywords: electron transfer, energy transfer, exciton coupling, conformational analysis, molecular wire, self–assembly, conjugated porphyrin oligomers, anthracene dendrimers, fs spectroscopy, ps spectroscopy, fluorescence anisotropy

LIST OF PUBLICATIONS

The thesis is based on the work described in the following papers:[1]

I. Hopping vs. Tunneling Mechanism for Long–Range Electron Transfer in Porphyrin Oligomer Bridged Donor–Acceptor Systems
Mélina Gilbert Gatty, Axel Kahnt, Louisa J. Esdaile, Marie Hutin, Harry L. Anderson and Bo Albinsson,
*J. Phys. Chem B.***2015**, DOI: 10.1021/jp5115064.

II. Conformational Gating of Charge Separation in Porphyrin–Oligomer–Fullerene Systems
Mélina Gilbert, Louisa J.Esdaile, Marie Hutin, Katsutoshi Sawada, Harry L. Anderson and Bo Albinsson,
J. Phys. Chem C **2013**, 117 (50), 26482–26492.

III. Self–Assembly of Linear Porphyrin Oligomers into Well–Defined Aggregates
Joakim Kärnbratt, Mélina Gilbert, Johannes K. Sprafke, Harry L. Anderson and Bo Albinsson,
J. Phys. Chem C **2012**, 116 (37), 19630–19635.

IV. Conjugated Anthracene Dendrimers with Monomer–Like Fluorescence
Karl Börjesson, Mélina Gilbert, Damir Dzebo, Bo Albinsson and Kasper Moth-Poulsen,
RSC Adv. **2014**, 4, 19846–19850.

V. Singlet–Singlet Annihilation in Linear and Circular Butadiyne–linked Porphyrin Oligomers
Mélina Gilbert Gatty, Joakim Kärnbratt, Harry L. Anderson and Bo Albinsson,
Manuscript in preparation.

[1] Papers are published before August 2014 with the name Mélina Gilbert and after 2014 with the name Mélina Gilbert Gatty.

CONTRIBUTION REPORT

Paper I. Performed the temperature–dependent steady–state fluorescence measurements. Performed analysis and interpretation of the fluorescence and transient absorption data. Wrote the paper.

Paper II. Designed and performed all experiments. Performed analysis and interpretation of the fluorescence data. Wrote the paper.

Paper III. Performed some of the temperature–dependent absorption measurements and helped in writing in the paper.

Paper IV. Designed and performed the steady–state and time–resolved fluorescence anisotropy measurements. Performed analysis and interpretation of the fluorescence anisotropy data. Wrote the paper except the synthesis part.

Paper V. Designed and performed some of the power–dependent femtosecond transient absorption measurements. Performed analysis and interpretation of the transient absorption data. Wrote the manuscript.

PUBLICATIONS NOT INCLUDED IN THIS THESIS

Photo–induced Charge and Energy Transfer in Molecular Wires
Mélina Gilbert and Bo Albinsson,
Chem. Soc. Rev. **2015**, 44, 845–862.

Steady–state and Time–resolved Thioflavin–T Fluorescence can report on Morphological Differences in Amyloid Fibrils formed by Aβ (1–40) and Aβ (1–42)
David J. Lindberg, Moa S. Wranne, Mélina Gilbert Gatty, Fredrik Westerlund and Elin K. Esbjörner,
Biochem. Biophys. Res. Com. **2015**, 458, 418–423.

Opportunities in nanometer sized Si wires for PV Applications
Jaswinder Kaur Mann, Rufi Kurstjens, Geoffrey Pourtois, Mélina Gilbert, Frederic Dross and Josef Poortmans,
Prog. Mater. Sci. **2013**, 58, 1361–1387.

TABLE OF CONTENTS

LIST OF ABBREVIATIONS AND SYMBOLS

ET	Electron Transfer
EET	Excitation Energy Transfer
PET	Photoinduced Electron Transfer
D–A	Donor–Acceptor
D–B–A	Donor–Bridge–Acceptor
RC	Reaction Center
PSI	Photosystem I
PSII	Photosystem II
P	Porphyrin
C	Carotenoid
Q	Quinone
OPE	Oligo–p–Phenylene Ethynylene
fl_n	Oligo–p–fluorene
ph_n	Oligo–p–phenylene
xy_n	Oligo–p–xylene
P_n	Butadiyne–linked zinc porphyrin oligomers
C_{60}	Fullerene
Fc	Ferrocene
TA	Transient Absorption

SYMBOLS IN SPECTROSCOPY

λ	Wavelength
ν	Frequency
$\bar{\nu}$	Wavenumber
c	Speed of light
h	Planck's constant
ε	Molar absorptivity
τ	Lifetime
Φ	Quantum yield
k	Rate constant

SYMBOLS IN ELECTRON TRANSFER

ΔG^0	Driving force
$\Delta G^{\neq}$	Activation energy
λ	Reorganization energy
V	Electronic coupling
k_B	Boltzmann's constant
ΔE	Tunneling energy barrier
R_{DA}	Donor–Acceptor separation distance
β	Attenuation factor

1 INTRODUCTION

Environment and Energy are two main challenges of this 3rd Millennium. While both problems arise from the way we have produced and consumed energy, they are now increasingly threatening the way we live, or even more, life and civilization on Earth.

Today the annual world energy consumption is estimated to ca. 140 x 10^3 TWh and is forecasted to reach 195 x 10^3 TWh by 2030.[1] At present, most of this energy comes from burning fossil fuels like oil and coal, which also generates 70 % of the carbon dioxide (CO_2) emissions that drive climate change. In the last twenty years, raising concerns on the climate change, reflections on our place in the natural world and our obligations to the generations to come, have come to the general agreement: we need urgently environmentally friendly and carbon–neutral energy sources to limit climate change. This problem is not a new one and one could say that we have been slow to respond to it. As featured by Richard Hamblyn in The Art of Science: A natural history of ideas,[2] already in 1895 in an address presented at the Royal Academy of Science, Svante Arrhenius foresaw the effects of increasing concentration of atmospheric CO_2 on the greenhouse effect and on climate, i.e. upon the surface's temperature of the Earth. He estimated that doubling of the CO_2 concentration in the atmosphere will raise the earth's temperature by 5 ºC.[3] Arrhenius did not explicitly link the use of fossil fuels to the climate change. It was only in the late 1980s that James E. Hansen affirmed publicly at the United States Congress the causal association between excessive burning of fossil fuels (i.e. build up of atmospheric CO_2 and other gases) and global warming.[4] His statement at the Congress made the headline in the New York Times: "Global Warming Has Begun, Expert Tells Senate".[5] Since then the use of polluting energy sources such as fossil fuels has been frequently debated and gained attention of the public realm. Fossil fuel resources are also not inexhaustible. Although it has taken millions of years for natural photosynthesis to accumulate such sources, in only 100 years most of the reserves have been consumed by mankind.

But we are lucky: the Earth is flooded everyday by a considerable amount of sunlight. To give some numbers, the solar energy that hits the Earth corresponds to ca. 108 x 10^7 TWh per year. In comparison to our current energy use, this gives a ratio between the annual solar flux and the current demand equal to ca. 7740. Solar light energy is clearly enough to meet our current and future needs. Thus, one solution to our energy and environmental problems would be to use sunlight to produce our fuels, i.e. solar fuels. Here one of the challenges arises from the fact that sunlight is dispersed and hence needs to be "captured" in an effective way. Moreover, while solar energy is "free", the development of systems which enable conversion of solar energy into other forms of energy such as electrical, chemical or electrochemical comes with a certain cost. In the last 20 years, multiple technologies have been developed to harvest solar energy and convert it into electricity, such as semiconductor–based solar cells[6] (e.g. silicon or gallium–arsenide based ones) or dye–sensitized solar cells[7-9] (DSSCs). However, most of them possess considerable drawbacks that hinder their global deployment. In short, the higher energy cost of such technologies compared to fossil fuels and the lack of

storage systems for electricity either for mobile applications (e.g. cars) or during dark periods are two main drawbacks that makes us still rely on the past photosynthesis (i.e. biomass and fossil fuels). But we can be hopeful just at the time when the first round–the–world solar flight, Solar Impulse®, is taking place.[10] We are already able to convert light–to–electricity and need to perform this conversion in a cheaper and more efficient way while adding versatility in the nature of the outcome energy (e.g. chemical, electrochemical).

Turning sunlight into other forms of energy is what Nature has been doing for millions of years via the photosynthesis in green plants and bacteria. Any photosynthetic system is able to convert sunlight into chemical energy. This conversion is realized via a series of light triggered step–wise energy and electron transfer processes between different chromophores. The final outcome of this "chain" of reactions is a long–lived charge–separated state with sufficient potential energy for water oxidation into molecular oxygen and carbon dioxide reduction into sugar. All reactions rely on a rather complex machinery which, in term of conversion efficiency, is also rather inefficient (often less than 1%).[11] But Nature can be an excellent source of inspiration for production of solar fuels such as hydrogen gas H_2. Indeed water oxidation produces not only molecular oxygen but also hydrogen ions (i.e. protons) whose in an artificial photosynthetic system could be further reduced to generate hydrogen gas. In that way, hydrogen gas could be produced from water and sunlight, and could remain cheap to produce. Part of the storage problem from which the already existing light–to–electricity conversion technologies suffer (*vide supra*) could also be solved since energy is then stored chemically (i.e. in the form of chemical bonds) in a synthetic energy carrier, e.g. hydrogen. Finally, combustion of hydrogen only produces water. Artificial photosynthesis has the potential to solve both the environmental and energy challenges. Giacomo Ciamician, an Italian professor of Chemistry was among the first to publicly express his beliefs in artificial photosynthesis for solar fuels' production. Although he had only his balcony to test his idea on photoinduced reactions, Giacomo Ciamician saw the ingenuity in the green plants' photosynthesis and its technological potential. In 1912, he gave a rather avant gardist lecture entitled "The Photochemistry of the Future" in which some statements still holds today.[12] After raising the problem of limited reserves of coal (today fossil fuels), he proposed the production of fuels via artificial photochemical reactions and pointed out a first problem "*how to fix solar energy through suitable photochemical reactions. To do this it would be sufficient to be able to imitate the assimilating processes of plants"* which is exactly the aim of artificial photosynthesis. He also postulated the existence of photocatalyst that could enable endo–energetic processes such as the production of oxygen from a water and carbon dioxide mixture. In 2015, more than hundred years after Ciamician's lecture, efficient artificial photosynthetic devices are yet not available.

Although we have now a much better understanding of the natural photosynthesis,[13-16] designing molecular systems that mimic the natural sequence of energy and electron transfer processes is not so simple to accomplish; and even more challenging is moving

to actual functioning artificial photosynthetic devices. The designed molecular systems must (i) significantly absorb over the visible part of the solar spectrum (ii) possess good electron donor and acceptor entities enabling the formation of a long–lived charge–separated state and (iii) possess properties for integration in devices (e.g. self–assembly properties or covalent interactions with other materials). To fulfill all these criteria, one relies on supramolecular (i.e. multicomponent) systems and coordination compounds (e.g. ruthenium, platinum complexes).[17-20] Thus, over the last two decades, considerable efforts have been devoted to the synthesis of electron donor–acceptor (D–A) mimics of the more complicated natural photosynthetic system.[17, 19, 21-22] Most of these D–A systems have been primarily investigated with the aim of creating charge separated states that live long enough to drive secondary redox reactions.[23-27] From a fundamental point of view, simple donor–acceptor model systems are also ideal systems to get more insights into excitation energy (EET) and electron (ET) transfer processes, i.e. to sort out the molecular parameters (e.g. geometry, electronic structure) that govern their kinetics and efficiencies. In the literature, a vast variety of D–A supramolecular systems has been reported employing e.g. porphyrins,[28-31] phthalocyanines,[32] phenotiazines,[33-36] coordination compounds[19-20, 37] as electron donor and e.g. fullerenes,[28, 38-42] graphene,[43-44] perylene imides[33-34] as electron acceptor.

Exploring how charge or energy moves in donor–acceptor systems provides guideline knowledge that not only applies to the design of efficient molecular systems for artificial photosynthesis, but also the design of molecular scale electronics. The 20th century may be seen as the golden era of the silicon–based technology for information processing. However, at the dawn of the 21st century, this technology seems to have already reached some limitation in term of device size with the smallest transistor reported at 22 nm (Intel® 22 nm Technology). It is difficult to decrease further the size of a single transistor without the use of expensive technologies (e.g. e–beam lithography). Part of the size limitation lies in the approach used to produce such structures, that is conventionally a top down approach namely photolithography. How to go beyond the 22 nm? This question has attracted much interest since there are many reasons why creating smaller devices will be advantageous. First, this allows confining more devices in a smaller space, hence realizing more functions. Second, "constructing smaller" means also using less material which saves natural resources. One answer to the above question is to use molecules to replace components (e.g. wires,[45] transistors,[46] switches[47-48]) in today's electronics.[49-52] Indeed the size of molecules is well beyond the 22 nm and ranges from few angstroms to several tens of angstroms. Even macroscopic size can be achieved with polymers. The way molecules can be assembled is also of interest. They assemble from the bottom up. In other words, assembling a molecular–based device will be similar to realizing a LEGO® construction. Even better, what if these molecules could self-assemble (i.e. spontaneously come together)? Here Nature is also inspiring in the way that all molecular components in the natural photosynthetic system come together to realize rather complex functions.

Regardless of the targeted applications, either for artificial photosynthesis or molecular electronics, of utmost importance is to understand how the donor and acceptor components in supramolecular systems interact. It means identifying the molecular properties that control the signal transmission between the donor and the acceptor, i.e. how fast electrons or excitation energy move between the donor and acceptor. Ultimately such studies, either theoretical or experimental, provide essential knowledge for applied research on how to design controllable molecular systems in which one can tune the flow of electrons or energy.

In this work, two series of multichromophoric systems have been investigated. In particular, their photophysical properties have been characterized, and their ability to mediate either electron and/or energy transport has been probed. In these systems, the excitation energy (EET) and electron transfer (ET) reactions were triggered using light excitation, and hence are so called photoinduced. The first series is a series of zinc porphyrin oligomers linked at their *meso* positions by 1,3–butadiyne denoted $\mathbf{P_n}$, spanning from monomer $\mathbf{P_1}$ (2.4 nm) to octamer $\mathbf{P_8}$ (12 nm). These conjugated porphyrin oligomers have a rod–like structure but are not strictly conformationally constrained systems. The second series consists of two generations of conjugated anthracene dendrimers denoted **G1** and **G2** containing 3 and 9 anthracene units, respectively. In contrast to the linear conjugated porphyrin oligomers, these anthracene dendrimers are structurally constrained 3D systems due to large steric hindrance. In general, the objective of this thesis is to gain more insights on the relationship between molecular properties (e.g. electronic structure, conformational distribution) and electronic communication in multichromophoric systems.

The papers included in this thesis are presented in two acts. The first act discusses Papers I-III and focuses on photoinduced electron transfer reactions in donor–acceptor systems employing conjugated porphyrin oligomers as the photoactive electron donor (Chapter 5). Paper I introduces a series of donor–bridge–acceptor (D–B–A) systems, $\mathbf{Fc–P_n–C_{60}}$, in which conjugated porphyrin oligomers $\mathbf{P_n}$ of different lengths (n = 1–4, 6) bridge a ferrocene (**Fc**) donor group and a fullerene $\mathbf{C_{60}}$ acceptor group. Our aim was to establish the causal relation between the observed wire–like properties (i.e. weakly distance–dependent electron transfer rates) and the nature of the charge transport mechanism (i.e. tunneling or hopping). Following Paper I, Papers II-III are discussed. Both papers investigate conformational dynamics effects on the photophysical properties of conjugated porphyrin oligomers. Common goal of these two papers was to identify how such effects might be of use to control intra– or inter–molecular processes: electron transfer in long donor–acceptor dyads ($\mathbf{P_n–C_{60}}$) in Paper II and self-assembly of $\mathbf{P_n}$ in Paper III, respectively. The second act is based on the results in Papers IV and V and compares the photophysical properties of the linear conjugated porphyrin oligomers with the ones of the anthracene dendrimers (Chapter 6). Special emphasis is put on understanding the influence of the linker topology on inter–chromophore communication, i.e. how individual chromophores communicate electronically with each other.

2 BEING INSPIRED BY NATURE

Nature possesses remarkable machineries for conversion of solar energy into chemical energy and hence, provides hints for fuel production based on solar energy. Taking the green plants' photosynthesis *as an example, this chapter attempts to give first a brief description of the natural photosynthesis. We will see that photosynthesis is a rather complex and interdisciplinary phenomenon that is triggered by a multitude of photoinduced energy transfer coupled to electron transfer reactions.*[13] *Since the natural photosystem is quite complex, approaches to avoid complexity in mimicking molecular systems have been developed. The second part of this chapter describes some of these approaches in view of applications in artificial photosynthesis and molecular electronics. Further, self–assembly is described as a tool to construct artificial molecular devices, such as devices capable of artificial photosynthesis. Finally, porphyrin–based molecular wires are introduced as simple model systems for photoinduced electron and energy transfer studies.*

2.1 THE NATURAL PHOTOSYNTHESIS: A COMPLEX MACHINERY

In any natural photosynthetic systems, photosynthesis starts with absorption of light by an antenna system, typically containing chlorophyll molecules which have high molar absorptivity ~10^5 $M^{-1}cm^{-1}$. The energy stored in the excited states of these molecules is then funneled by fast energy transfer to a reaction center (RC). This occurs in a stepwise manner, i.e. the excitation energy moves from one chromophore to another, and reaches the RC within 10–100 ps.[14-15, 53] In the reaction center, the excitation energy initiates a cascade of electron transfer reactions which creates a long–lived charge–separated state. Thus, it is in the RC that the electronic excitation is converted into an electrochemical potential. The process then continues with the so–called "dark" reactions of photosynthesis generating a chemical potential. For oxygenic photosynthetic systems, this refers to the oxidation of water into oxygen and protons and the reduction of carbon dioxide to carbohydrates (or sugars) or other kinds of chemically stored energy.

The green plants' photosynthesis

In green plants' photosynthesis, water oxidation and carbon dioxide reduction require two reactions centers, known as Photosystem I (PSI) and Photosystem II (PSII), to work in series. In PSII, water oxidation occurs and generates molecular oxygen and protons, while reduction of carbon dioxide into sugar is performed in PSI. The overall photosynthetic process often called "Z–scheme" is illustrated in Figure 2.1.

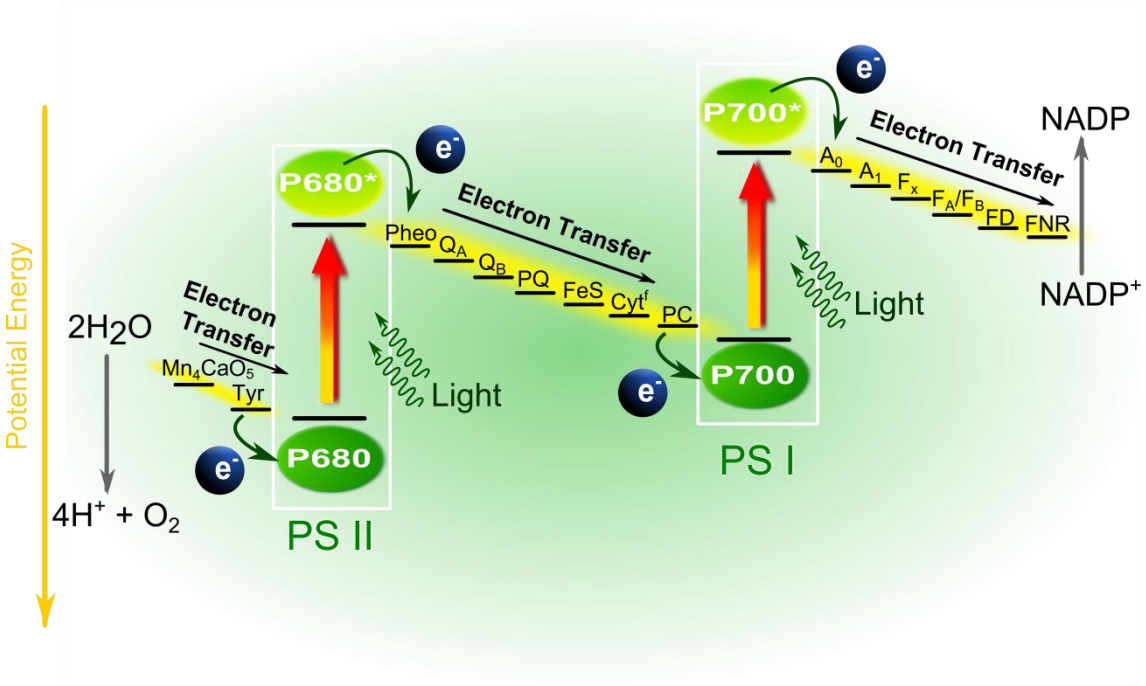

Figure 2.1 Simplified schematic of the charge–separation processes in the green plants' photosynthesis. P680: pigment (chlorophyll) absorbing at 680 nm; P700: pigment (chlorophyll) absorbing at 780 nm; Mn_4CaO_5: manganese calcium oxide cluster; Tyr: tyrosine; Pheo: Pheophytin; Q_A: primary plastoquinone electron acceptor; Q_B: secondary plastoquinone electron acceptor; PQ: plastoquinone; FeS: iron sulphur protein; Cyt^f: cytochrome f; PC: plastocyanin; A_0: primary electron acceptor of PSI; A_1:phylloquinone; F_x, F_A, F_B: three separate iron sulphur centers; FD: ferredoxin; FNR: ferredoxin NADP oxido reductase; NADP: Nicotinamide Adenine Dinucleotide Phosphate. Adapted from reference 54.

In PSII, direct photon excitation or, more commonly excitation energy transfer from the antenna system promotes the pair of chlorophylls P680, often called "special pair" to an electronic excited state $P680^*$ which rapidly donates an electron to the nearby acceptor Pheophytin, creating an initial charge–separated state. Thus, electrochemical energy is generated from electronic excitation. However, this first charge–separated state is vulnerable since it can easily be lost though backward ET processes. To avoid such recombination processes, a series of rapid down–hill electron transfer processes follow that moves away the electron from the initial donor P680. In the meantime, in PSI, another chlorophyll–like pigment P700 is promoted to its electronic excited state $P700^*$ by energy transfer from the antenna system. An initial charge–separated state is formed by electron transfer from $P700^*$ to A_0 the primary acceptor of PSI and subsequently followed by a series of electron transfer reactions to hinder its recombination as in PSII. This generates a strong reducing species, NADPH, which provides electrons for the reduction of CO_2 into sugars or other organic molecules. Finally, P700 in PSI is regenerated by electron transfer from $P680^*$ to the oxidized $P700^{\bullet+}$ via the intermediate electron transfer steps described above. P680 in PSII is regenerated through oxidation of Tyrosine and subsequently Mn_4CaO_5 by $P680^+$. Thus, common to PSI and PSII is the cascade of fast down–hill electron transfer steps that enables spatial separation of the

charges (electron and hole). To give a number, electrons and holes are separated by ~30 Å within less than 1 ns. This of course has an energy cost, but creates charge–separated states that live long enough to carry out the dark reactions of photosynthesis which are typically slow (i.e. tens of seconds) due to their dependence on molecular diffusion.

Parts of the beauty of the natural photosynthesis lay in the way that energy transfer reactions are coupled to electron transfer reactions to adjust the ultrafast dynamics of light harvesting to the slow biological reactions. The natural chromophores not only harvest light efficiently but are also compatible for interaction with the rest of the systems.[55] Here "compatible for interaction" refers to their specific arrangement that enables efficient and directed energy transfer in the antenna system and down–hill electron transfer in the reaction center. For example, the groups of Van Grondelle,[56-57] Scholes and Fleming[16] have demonstrated that structural organization of the chromophores in the antenna systems is one determining factor for the directionality and the rates of energy transfer. Along with the large number of components involved, all the structural requirements turn any natural photosynthetic system into a complex machinery difficult to reproduce artificially. Further, one may wonder why such complex machinery is required for photosynthesis.

The water oxidation reaction

On the PSII side, water oxidation into molecular oxygen and protons is a four–electron process (reaction 2.1). It involves two water molecules and implies the removal of four electrons (i.e. two electrons per water molecule) and the transfer of four protons.

$$2H_2O \rightarrow O_2 + 4H^+ + 4e^- ; E^0 = + 0.82 \text{ eV vs NHE at pH 7} \qquad 2.1$$

This means that at least four photons are required to reach sufficient electrochemical potential, and hence drive the dark reactions in PSII. In other words, four successive photoinduced charge separation should take place at a single reaction center. Once more the natural photosynthetic system is remarkable, since the catalyst Mn_4Ca cluster can be oxidized stepwise by Tyr^+ and the intermediates generated live long enough for oxygen to be produced after four charge–separation processes. It has also been shown that the natural photosynthetic system is able to adapt the antenna size per reaction center depending on the light conditions to guarantee an optimal rate of photo–excitation of the reaction center.[58] Finally, it is interesting to have a look to the photosynthetic overall efficiency. As mentioned earlier, PSI and PSII work in series, this means that in total, eight photons are required to release one molecule of oxygen and reduce one carbon dioxide molecule. Hence, for the formation of one glucose molecule $C_6H_{12}O_6$, 48 photons need to be absorbed. Not only the number of absorbed photons matters, formations of the photo-excited states $P680^*$ and $P700^*$ impose also some conditions on the energy of the absorbed photons which must exceed 1.83 eV (i.e. $\lambda_{exc} < 680$ nm) in order to excite P680. In term of energy conversion efficiency, both the large number of photons and the type of photon (i.e. photons of about 1.8 eV) required put considerable

limitations on the overall photosynthetic efficiency with a maximum of ~9 %. Additional losses induced by photodamage and saturation (i.e. excessive excitation) brings the energy–conversion efficiency of the natural photosynthesis down to few percent.[11] Thus, considering the fact that photosynthesis only requires sunlight as power and water and carbon dioxide as raw materials to produce fuels, it can be seen as a successful system for energy production and storage. However, it is of low efficiency.

If artificial photosynthesis should become one viable solution for renewable energy production, much simpler molecular systems need to be developed and a more efficient light–to–chemical energy conversion needs to be achieved. Another important difference is the reaction of interest which is the water splitting reaction not into protons and molecular oxygen, but into molecular hydrogen and oxygen using sunlight (reaction 2.2).

$$2H_2O + 4\ h\lambda/c \rightarrow 2H_2 + O_2\ ;\ \Delta G^0 = 4.92\ eV \qquad 2.2$$

If the electronic absorption spectrum of water and the solar spectrum did overlap, dissociation of water could take place by direct absorption of sunlight. However, this is not the case ("fortunately"): water absorbs significantly only in the far UV at wavelengths shorter than 170 nm. The most convenient (or less energy costly) way to realize reaction 2.2 using sunlight is via two multi–electron processes,

$$2H_2O + 2e^- \rightarrow H_2 + 2OH^-\ ;\ E^0 = -0.41\ eV \text{ vs NHE at pH 7} \qquad 2.3$$

$$2H_2O \rightarrow O_2 + 4H^+ + 4e^-\ ;\ E^0 = +0.82\ eV \text{ vs NHE at pH 7} \qquad 2.4$$

Here in reaction 2.4, one can recognize the water oxidation reaction that occurs in the natural photosystem PSII. As it happens in PSII, four successive photoinduced charge separations will be necessary. Reactions 2.3 and 2.4 put also some conditions on the HOMO–LUMO gap of the chromophore with a thermodynamic threshold of 1.23 eV. Further, if we assume that each reaction has a driving force of 0.3 eV, chromophores that have a HOMO–LUMO gap of more than 1.83 eV (i.e. preferably absorbs in the visible region of the electromagnetic spectrum at wavelengths below 677 nm) should be ideal. Note that this last condition is fulfilled by the special pair P680 in PSII (*vide supra*), hence the numerous studies on synthetic dyes which are P680–like molecules.

2.2 AVOIDING COMPLEXITY BY CREATING SIMPLE MODEL SYSTEMS

Althougth considerable knowledge on the structures of natural photosystems has been acquired in the last 20 years, as illustrated by the number of papers on the crystal structure of e.g. PSII presenting a continuous improvement in resolution,[59-67] it remains impossible to envisage an identical reproduction of the natural complexes using current

chemical synthesis. Nevertheless, as discussed above, the natural light–harvesting antenna and reaction center structures can be of inspiration for developing light–harvesting devices and photoinduced charge separation devices. Nature provides proven examples of the utility of combining several molecular systems in an organized architecture to realize different photoinduced reactions. Hence, considerable efforts have been devoted to the construction of simpler multi–component systems mimicking of natural photosynthetic systems. These simpler systems not only provide means to study the fundamentals of energy and electron transfer processes but also allow for exploration of the different functions that can be photoinduced in molecules (e.g. wires, switches and transistors) depending on how molecules make use of the photon energy. In the design of electron donor–acceptor systems, the sometimes called supramolecular approach has been extensively used. This approach presents several advantages. By linking covalently donor and acceptor molecular groups, one avoids the problem of having diffusion limited EET and ET reactions and replaces intermolecular communication by intramolecular communication. Another advantage is the sufficient structural constraint that such D–A molecules possess. This allows for control of both donor–acceptor distance and orientation.

2.2.1 TOWARDS ARTIFICIAL PHOTOSYNTHESIS

To mimic the charge–separation function of the reaction center, a primary requirement is an electron donor that absorbs efficiently in the visible region and a suitable electron acceptor. The second requirement is the formation of a long–lived charge–separated state in which electrochemical potential is stored for sufficiently long time to carry out slower chemical reactions (*vide supra*). Among the first molecular systems mimicking the initial charge separation step of photosynthesis was a simple donor–acceptor dyad, **P–Q**, consisting of a porphyrin molecule (**P**) as electron donor covalently linked to a quinone (**Q**).[68] Upon photo–excitation of the porphyrin, the charge–separated state, $\mathbf{P^{\bullet+}–Q^{\bullet-}}$, was generated. This charge–separated state could hold 1.4 eV, i.e. most of the intrinsic energy of the porphyrin singlet excited state (1.9 eV). However, $\mathbf{P^{\bullet+}–Q^{\bullet-}}$ was too short–lived (τ = 100 ps) to carry out redox reactions. Recalling how in Nature long–lived charge separated state are generated, triad systems have been synthesized that employ a secondary donor/acceptor to further separate spatially electrons and holes. Such approach was first used by the groups of Gust and Moore who reported a carotenoid–porphyrin–quinine triad (**C–P–Q**) obtained by appending to **P–Q** an additional electron donor, the carotenoid group (**C**).[69] Upon photo–excitation of the porphyrin in **C–P–Q**, an initial charge–separated state, $\mathbf{C–P^{\bullet+}–Q^{\bullet-}}$, forms and subsequently undergoes charge–shift creating the final long–lived charge–separated state, $\mathbf{C^{\bullet+}–P–Q^{\bullet-}}$ (τ = 57 ns). They also demonstrated that further addition of electron donors and acceptors to form tetrad (**C–P–Q1–Q2**) and pentad (**C–ZnP–P–Q1–Q2**) could lead charge–separated states with lifetimes as long as 55 μs for the pentad with a quantum yield of 0.83.[23] Since these first reports, a large number of D–A systems have been reported in literature aiming at: generating long–lived charge–separated states

whose energy can be used to perform water oxidation;[70-72] coupling artificial antenna and reaction center functions within one molecular system;[73-74] coupling electron transfer and proton transfer;[27, 75-77] coupling the one–photon photoinduced charge separation with the multi–electron water splitting (reaction 2.4).[18, 26, 78]

2.2.2 TOWARDS MOLECULAR WIRES FOR LONG–RANGE ELECTRON AND ENERGY TRANSFER

Just as donor–acceptor systems can be used in artificial reaction centers to convert light into electrochemical potential, they can also be applied in molecular electronics for information exchange. In this context, the simplest electronic component is probably the wire whose function is to electrically interconnect two devices. Thus, it is not surprising that researchers have first investigated the possibility of creating wires based on molecules instead. By covalently linked a donor–acceptor couple with a molecular bridge (B), donor–bridge–acceptor (D–B–A) systems can be formed that are comparable to an electrical circuit where D and A are the input/output components and B represents the electrical interconnection. As in electrical circuitry, achieving the desired output e.g. voltage or intensity requires an understanding of how the different components operate not only individually but also when connected to each other. This knowledge can be used to control the output. Likewise, the chromophores (D, B, A) can be studied individually. When assembled in D–B–A, the weak coupling between the donor and acceptor imposed by the bridge separation makes it possible to selectively excite the donor or the acceptor. This may trigger electron or/and energy transfer reactions. The final "output" is then either the formation of a long–range charge–separated state $D^{\bullet+}$–B–$A^{\bullet-}$ in the case of electron/hole transfer or emission of a photon by the acceptor in case of energy transfer.

In the viewpoint of molecular wire applications, the goals are slightly different from the ones of artificial photosynthesis. A first goal is the ability to transport charge or energy over long distances, i.e. few tens of nanometers with high efficiency. In this regard, most studies aim at establishing knowledge on the appearance of weakly distance–dependent wire–like charge (or energy) transport in molecules. In practice, the distance dependence of ET or EET in D–B–A is investigating by measuring the rate of ET or EET as a function of the donor–acceptor distance, R_{D-A}. R_{D-A} is simply varied by modifying the number of rigid repeating units composing the bridge, i.e. "the molecular wire". In the case of ET, the results of such distance dependence studies are often presented in a plot of ln k_{ET} vs R_{D-A} and a single exponential decay constant in agreement with the McConnell model (*vide infra*) called the attenuation factor β is reported. The β–values describe how fast the electron transfer rate decreases with the distance; hence ideally values as close as to zero as possible are desirable as they would enable charge transport over almost infinite distances. In the literature, a multitude of D–B–A systems capable of electron transfer have been reported. Among them, D–B–A systems employing π–conjugated bridges consisting of identical repetitive molecular

motifs covalently connected have emerged as the most promising candidates for long–range energy/charge transport. For a list of D–B–A systems employing π–conjugated bridges, please see e.g. our recent review "Photo–induced Charge and Energy Transfer in Molecular Wires".[79] The β–values in these D–B–A systems span a wide range from 0.8 $Å^{-1}$ to < 0.01 $Å^{-1}$.[28-29, 33-34, 39, 80-87] However, it was realized quite early that the information contained in these β–values was of rather limited use when it came to provide guidelines for designing molecular systems with pre–defined conduction properties. For the same bridge structure, several studies reported different β–values and hence revealing the non–specificity of the β–value to a particular bridge structure and instead its dependence on the entire D–B–A ensemble.[29, 34, 40, 82, 86, 88-89] The β–values are not directly comparable to the conductivity (or resistance), i.e. the material–specific property used in electronic circuitry. Thus, in the last ten years, focus has been put on understanding the role played by the molecular bridge in charge transport, i.e. tunneling energy gap effects. A second goal that is seeked in molecular wire applications is the possibility to control charge or energy transport. In this context, conformational effects on electron/energy transfer rates in D–B–A molecules have attracted much interest. The following sections provide examples of D–B–A molecules in which tunneling energy gap effects and conformational effects on charge and energy transport could be investigated in a systematic way.

Tunneling energy gap effects in D–B–A molecules

Several groups have devoted much effort to the design of D–B–A systems that enables to elucidate the role played by the bridge in charge transport. One important outcome of these studies is the experimental evidence of tunneling energy gap effects that explain in part why β–values are not bridge–specific. The bridge energetics does influence the kinetics (i.e. distance dependence of charge transport) and the nature of the charge transport between the donor and acceptor, in accordance with the prediction of the McConnell model (equations 3.24 and 3.25). By bridge energetics, one designate the tunneling energy gap between the donor and bridge for electron transfer ΔE_{DB} (or energy gap between the acceptor and the bridge for hole transfer ΔE_{BA}). Different experimental approaches have been taken to show the dependence of k_{ET}, hence β on the tunneling energy gap, ΔE. For example, Albinsson and co–workers designed a series of D–B–A molecules **ZnP–RB–AuP$^+$** employing an oligo–p–phenylene ethynylene (**OPE**)–based bridge (**RB**) of constant length to link the porphyrin donor (**ZnP**) to the electron acceptor (**AuP$^+$**). They could tune the tunneling energy gap for charge separation, ΔE_{CS}, by replacing the central benzene of the **OPE**–based bridge by either naphathalene (**NB**) or anthracene (**AB**) while maintaining a constant R_{DA}. As a result, when going from anthracene (**AB**) to naphthalene (**NB**) to benzene (**3B**), ΔE_{CS} increases due to increasingly higher lying singlet excited state of the bridge unit (see Figure 2.2). Very nicely, the measured ET rates also followed the same trend: k_{ET} = 2.54 x 10^9 s^{-1} for **3B**, 4.48 x 10^9 s^{-1} for **NB** and 3.03 x 10^{10} s^{-1} for **AB**.[29, 81, 90]

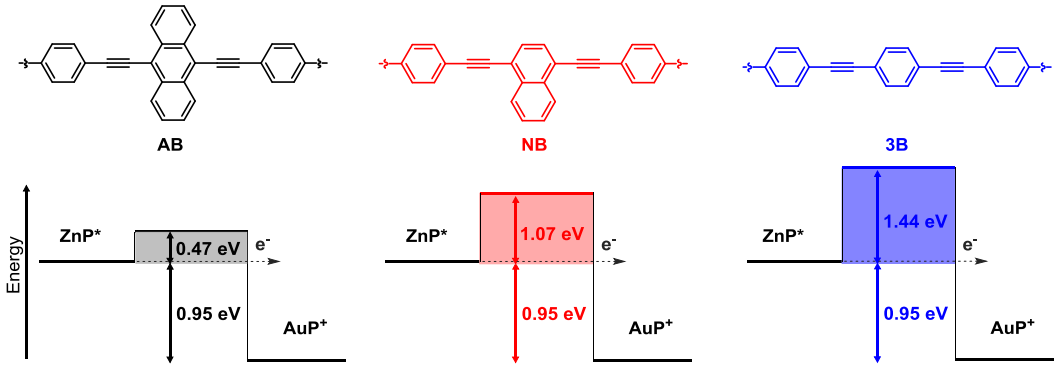

Figure 2.2 (top) Molecular structures of the **OPE**–based bridge in the series of **ZnP–RB–AuP**$^{+}$ with **RB** = **AB**, **NB** or **3B**. The donor–acceptor distance was 26.5 Å in the three D–B–A systems. (bottom) Schematic energy diagrams for charge separation via electron transfer in these systems. Note that the energy barriers are not the true energy barriers but are crude estimates from the donor–acceptor LUMOs. Reproduced from Ref. 79 with permission from The Royal Society of Chemistry.

Other well suited systems for investigating tunneling energy gap effects are D–B–A systems employing oligo–p–xylenes (**xy$_n$**) as bridge unit. Oligo–p–xylenes bridges possess nearly length–independent (redox) energies which makes them interesting systems to test theoretical predictions of superexchange transport.[91-92] Indeed, the McConnell model, i.e. equations 3.23 and 3.25 for the electronic coupling and attenuation factor, respectively assumes a constant tunneling energy gap. Wenger and co–workers synthesized two series of D–B–A systems employing oligo–p–xylenes to bridge two different hole donor/acceptor couples. The first series **PTZ–xy$_n$–Re** (n = 1–4) used phenothiazine (**PTZ**) as hole acceptor and rhenium(I) tricarbonyl phenanthroline (**Re**) as hole donor. In the second series **PTZ–xy$_n$–Ru** (n = 1–4), the hole donor was replaced by ruthenium(II) tris(2,2'-bypiridine) (**Ru**). As a result of the change of donor, the tunneling energy barrier for hole transfer differed significantly in both series: ΔE_{BA} = 0.25 eV for **PTZ–xy$_n$–Re** and ΔE_{BA} = 0.45 eV for **PTZ–xy$_n$–Ru**. In agreement with equation 3.25, such ΔE_{BA} difference led to a much stronger distance dependence of the hole transfer rates for the **PTZ–xy$_n$–Ru** series (β = 0.52 Å^{-1}) with respect to the **PTZ–xy$_n$–Re** series (β = 0.77 Å^{-1}).[82]

Of interest is also the implication of these studies for the appearance of wire–like charge transport, i.e. a low β–value. A small tunneling energy barrier between the donor (or acceptor) and the bridge should lead to a low β–value (equation 3.25). Hence matching the energy levels of the donor/acceptor and the bridge has been considered as one condition to achieve wire–like charge transport. This pushes the ET processes in a new charge transport regime, i.e. in the incoherent hopping regime, where the electron or hole may temporally reside on the bridge before reaching the acceptor. A more exhaustive description of charge transport mechanisms in D–B–A systems is provided in chapter 3. Wire–like charge transport was successfully observed by Wasielewski and co–workers in a **PTZ–fl$_n$–PDI** series consisting of a perylene imide–type (**PDI**) hole acceptor linked to phenotiazine (**PTZ**) using fluorene bridges (**fl$_n$**) (n = 2–4).[34] In this

D–B–A series, the energy level of the acceptor approximately coincided with the bridge energy level and led to a nearly constant tunneling energy barrier that was small enough ($\Delta E \sim 0.15$ eV) for hole transport to occur in the incoherent hopping regime. The hole transport via incoherent hopping resulted in a very small β–value ($\beta = 0.093$ Å^{-1}). However, the systematic implication of a wire–like behavior in D–B–A systems with charge transport in the incoherent hopping regime has recently been questioned. In order to favor hopping charge transport, Wasielewski and co–workers voluntarily created a down–hill energy gradient within a series of fluorenone–bridged D–B–A molecules.[87] They effectively observed electron transfer in the hopping regime but this unexpectedly did not preclude a strong distance dependence of the ET rates with $\beta = 0.34$ Å^{-1}. Thus, designing D–B–A systems with pre–defined wire–like properties is not so simple and remains quite a challenge.[87, 93-94] In chapter 5, mechanistic criteria for the appearance of wire–like properties in a series of porphyrin oligomer–bridged donor–acceptor systems **Fc–P$_n$–C$_{60}$** (n = 1–4, 6) are further discussed.

Conformational effects on ET and EET rates in D–B–A molecules

π–conjugated bridged D–B–A molecules possess often sufficient structural constraint to control the distance between the donor and the acceptor. However, the bridge in such systems often remains a dynamic entity. For example, in π–conjugated bridges made of planar units, each unit may rotate in and out of the plane depending on the linkage topology, giving rise to a multitude of rotational conformers. In other words, the dihedral angles between the planes of two consecutive bridge units (φ_m), but also the dihedral angle between the donor or acceptor plane and the plane of the first bridge unit (ω_{DB} or ω_{BA}) may vary as illustrated in Figure 2.3. Several groups have investigated how variation of these dihedral angles influences the electronic communication in D–B–A molecules. In particular, they demonstrated that the inter–bridge dihedral angle imposed often an angular dependence to the inter–bridge coupling, V_{BB}, hence an angular dependence of the overall donor–acceptor electronic coupling, V_{DA}, and a conformational gating of the observed ET rates (equations 3.23 and 3.24, respectively). This property is particularly interesting since applying structural constraints to the bridge in D–B–A molecules could in principle enable the control of the ET rates. Such effects, if controlled by some kind of external stimuli, could open the possibility to use molecular systems for switching or memory purposes.[47, 95]

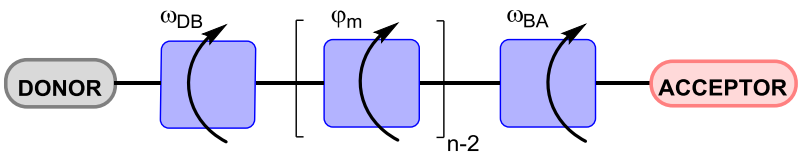

Figure 2.3 Schematic block diagram of a D–B–A system consisting of planar bridge subunits. The different dihedral angles used to describe the conformational geometry of the bridge are indicated. Adapted from Ref. 79 with permission from The Royal Society of Chemistry.

One challenge in conformational studies is that variation of dihedral angles (ω_{DB}, φ_m or ω_{BA}) may affect several parameters, i.e. V_{BB} and bridge energetics and hence tunneling energy barriers. In addition, conformational effects are also solvent–and temperature–dependent. This renders interpretation of the kinetics more difficult. For example, Wasielewski and co–workers investigated the influence that bridge dynamics has on the ET rates in oligo–p–phenylenevinylene bridged D–B–A molecules with tetracene as donor and pyromellitimide as acceptor.[96] In these D–B–A molecules, conformational effects led to a complex temperature dependence of the ET rates which did not follow Marcus predictions (equation 3.20). They demonstrated that in all D–B–A molecules, torsional motion in the excited state between the tetracene donor and the first bridge phenyl ring governed the overall donor–acceptor electronic coupling. In the longer systems containing a vinyl group, the "picture" became even more complex with additional intra–bridge torsional motions between the vinyl group and the phenyls contributing to the conformational gating of V_{DA} and the ET rates. In a more simple approach, Wenger et al. compared the ET rates of a series of D–B–A molecules employing structurally similar bridges but with different intra–bridge dihedral angles.[97] The series of D–B–A molecules had a rhenium complex as hole donor and phenothiazine as hole acceptor connected by either two phenyls (**ph$_2$**), two xylenes (**xy$_2$**) or a fluorene group (**fl$_1$**). R_{DA} was identical in the three systems. However, they measured an increase in hole transfer rates, k_{HT}, when going from **xy$_2$** (k_{HT} = 0.5 x 10^8 s^{-1}; ΔE_{DB} = 0.25 eV) to **ph$_2$** (k_{HT} = 2.6 x 10^8 s^{-1}; ΔE_{DB} = 0.54 eV) to **fl$_1$** (k_{HT} = 5.3 x 10^8 s^{-1}; ΔE_{DB} = 0.16 eV), that could not solely be explained by tunneling energy gap effects. In fact, they found that variation of the dihedral angle between the two phenyl planes ($\varphi_{ph\text{-}ph}$ = 65º for **xy$_2$**, 35º for **ph$_2$**, 6º for **fl$_1$**) among the compared D–B–A molecules strongly affected the electronic coupling between neighboring bridge sites, and hence V_{DA} and k_{HT} (equations 3.23 and 3.24). They concluded that only the combined effects of the tunneling energy gap and conformation of the bridge could explain the observed kinetic trend in this series. Similar effects of the inter–bridge dihedral angle on ET and EET rates have been reported in oligo–p–phenylene–bridged D–B–A systems by the groups of Scandola[98] and De Cola[99], respectively.

Influence of the bridge conformation on EET processes has also been largely investigated.[100-105] Harriman and co–workers were among the first to demonstrate experimentally that the donor–acceptor electronic coupling for intramolecular triplet excitation energy transfer (TEET) is function of the dihedral angle between adjacent bridge units.[100-101] They synthesized a series of ruthenium (II)/osmium(II) $(tpy)_2$ donor–acceptor complexes linked by ethynylene–substituted biphenyl bridges. To control the dihedral angle between the two phenyl units, φ, they used a tethering strapped chain linking respectively the *ortho* position of the first phenyl to the *ortho* position of the second phenyl (Figure 2.4). Varying the number of carbon atoms in the strapped chain modified the angle φ but kept a fixed donor–acceptor distance. Their measured transfer rates, k_{TEET}, hence V_{DA} displayed a strong dependence on φ, i.e. the conformation of the bridge. For example, at the largest dihedral angle of 90º (i.e. when the phenyl planes are perpendicular to each other), V_{DA} dropped drastically due to a

complete breakdown of the π–conjugated pathway between the two phenyls, and so did the transfer rate which decreased by a factor 80. The strap approach was also used by Osuka and co-workers for systematic control of the dihedral angle between directly linked meso–meso diporphyrins.[104] They demonstrated the strong correlation between the dihedral angle and the extent of π–conjugation and in turn the resulting two–photon absorption properties of these porphyrin dimers.

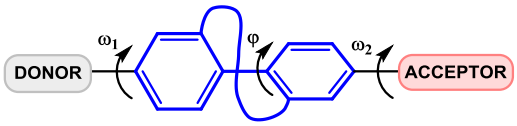

Tethered strap approach

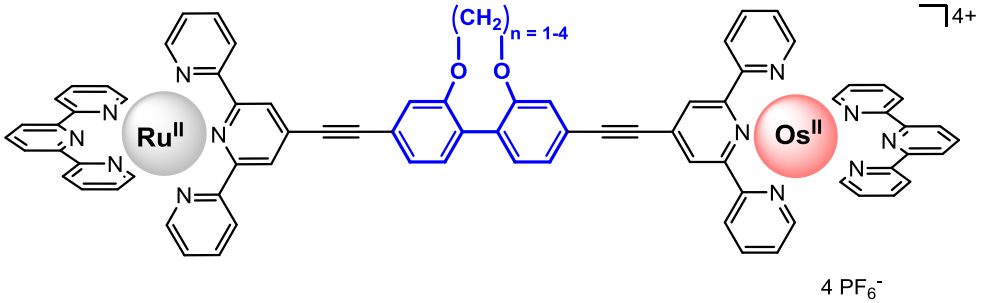

Donor-Bridge-Acceptor with the strapped bridge

Figure 2.4 (top) Schematic of the tethered strap approach proposed for systematic control of the intra–bridge dihedral angle, φ. (bottom) Molecular structure of one D–B–A system with a tethered strapped bridge studied by Harriman and co–workers. Adapted from Ref. 79 with permission from The Royal Society of Chemistry.

Synthetically less demanding, temperature control of the bridge conformational distribution was also proposed by Albinsson et al.[102] to investigate the impact of bridge disorder on TEET in D–B–A molecules. In their work, the D–B–A molecules were linked by **OPE** bridges of different lengths. The temperature dependence of the distance–dependent k_{TEET} was measured from room temperature to 80 K. The resulting β–value was found to be strongly temperature–dependent. To explain such temperature–dependence of the β–value, they developed in parallel a theoretical model for the calculation of V_{DA} based on a Boltzmann distribution of conformations.[106-107] Their theoretical model demonstrated the conformational gating of the electronic coupling, i.e. its dependence on the dihedral angle φ, and hence the conformational dependence of the β–value. Moreover, this model could successfully be used to reproduce the experimentally measured temperature–dependence of the β–value over the entire temperature range 80 – 200 K.

2.3 TAKING THE "NM TO MACROSCOPIC SCALES" STEP WITH MOLECULES USING SELF–ASSEMBLY

We have seen that covalently–linked D–B–A systems are useful model systems to study the dependence of ET and EET rates on donor–acceptor distance, electronic coupling and orientation. However, such systems often cover distances of only few nanometers.[108] This limits their field of applications. Few exceptions have been reported in the literature.[109-113] For example, giant *meso–meso*–linked zinc porphyrin oligomers with micrometer molecular length have been synthesized by Osuka et al.[110] But the resulting structures showed a high degree of conformational flexibility with the longest oligomer (ca. 0.85 mm) adopting a snakelike bent structure. Likewise, most of the long covalent systems reported in the literature suffer from a lack of rigidity that disrupts the electronic communication along the chain.[111] Further, they often required complex synthetic chemistry. Despite powerful synthetic strategies recently developed to build large supramolecules (e.g. template–directed synthesis for long porphyrin oligomers and iterative synthetic methods),[110, 112-114] it remains difficult to synthesize micrometer–sized molecules containing various functional entities. One simpler approach to build complex molecular architectures which can achieve microscopic size is self–assembly.[115-116] By self–assembly, the pre–existing components in a "mixture" spontaneously come together, i.e. are able to form more complex and ordered structures by molecular recognition. The molecular components are hold together by non–covalent or weakly covalent interactions such as π–π stacking, hydrogen bonds and metal coordination bonds. Thus self–assembly is less demanding in term of synthesis as it is based on molecular recognition properties, i.e. geometrical (molecular shapes) and chemical (intermolecular interactions) complementarities. Once more, Nature offers several examples of self–assembled systems.[117-118] For example, the special pairs P680 and P700 in the RC of PSII and PSI, respectively possess a dimer structure that relies on π–π stacking interactions between two chlorophyll *a* macrocycles.[62, 117] In synthetic self–assembled molecular ensembles, for the "molecular–legos" to spontaneously organize themselves the way we want, one need to have the appropriate molecular recognition properties. Hence it initially requires a smart design of the different molecular–legos. The idea is to start with the synthesis of functional building blocks as simple as possible (i.e. involving a minimum number of covalent bonds) which possess the appropriate molecular recognition property for self–assembly. In regard to the production of functional devices, self–assembly is one practical strategy proposed for coupling energy and electron transfer in artificial photosynthetic devices and for generating molecular ensembles capable to sustain charge and energy transport over micrometer distances. In this context, a fundamental question needs to be addressed: Can charge and energy transport between non–covalent molecular structures occur as efficiently as in covalent structures? Wasielewski and co–workers have addressed this question and investigated ET and EET in several self–assembled molecular ensembles.[119] As "molecular–legos", they used primarily perylene–dicarboximide (**PDI**) and its derivatives. For example, they synthesized a light harvesting block consisting of

a central **PDI** chromophore appended with four peripheral **PDI** chromophores that self–assembled into ordered dimers via π–π stacking.[120] More interestingly, they demonstrated efficient energy transfer between the stacked monomers occuring on a time scale (ca. 5 ps) comparable to the one observed in the light harvesting systems of green plants. To create functional artificial photosynthetic systems, one requirement is the ability to perform in series the light harvesting and charge separation functions within in a single molecular ensemble. This can be achieved by self–assembly as demonstrated by the groups of Gust[74] and Wasielewski.[121] Gust et al. constructed an antenna/reaction center heptad complex consisting of two components, i.e. a circular hexad antenna system bearing two zinc porphyrins and a fullerene electron acceptor bearing pyridil groups.[74] Both components spontaneously come together by metal–ligand interactions between the zinc porphyrins and the fullerene acceptor. The excitation energy was found to funnel very efficiently from the antenna system to the porphyrins, where charge separation subsequently occurred by donation of an electron to the fullerene. In the work of the Wasielewski group,[121] the self–assembly of the light harvesting system and the reaction center arose from π–π interactions between monomers consisting of a **PDI** derivative core decorated by four **PDI** molecules. Such monomers form spontaneously a π–stacked dimer, in which the peripheral **PDI** array acts as an antenna and the PDI derivative core dimer bio–mimics the "special pair" of the RC. As in the natural reaction center, they also showed that charge separation only occurred in the dimeric system.

2.4 CONJUGATED PORPHYRIN OLIGOMERS

2.4.1 MOTIVATION

In this work, porphyrins are used as covalent building blocks to the formation of multiporphyrin systems. Porphyrins are planar 18π–electron conjugated macrocycles formed by four pyrrole units and four methine carbons. They are analogous to the chlorophyll molecules present in the natural photosynthetic antenna and reaction center but their structure is simpler and so is their synthesis (Figure 2.5).

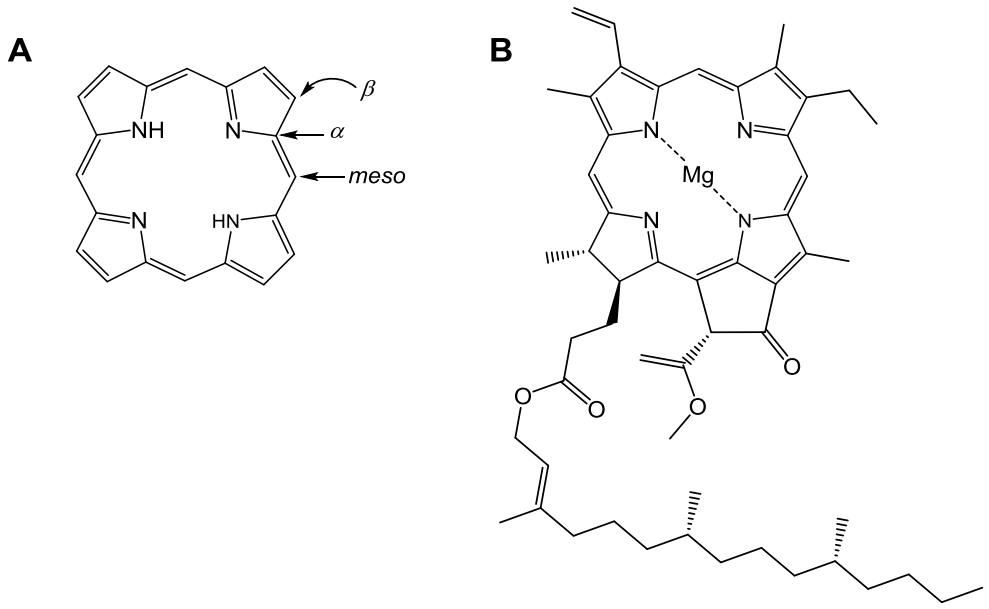

Figure 2.5 (A) Molecular structure of a free–base porphyrin indicating the peripheric positions for substitution: *α, β, meso*. (B) Molecular structure of chlorophyll *a*.

Just as chlorophyll molecules, porphyrins are good light harvesters with high molar absorption coefficient in the visible region ($\varepsilon \sim 4.2 \times 10^5$ $M^{-1}cm^{-1}$ at 442 nm for the zinc porphyrin monomer **P_1** studied in this work, see Chapter 6 Figure 6.2). Figure 2.6 shows as an example the ground–state absorption spectrum of zinc tetraphenylporphyrin (**ZnTPP**) measured in toluene. This spectrum is characteristic of metalloporphyrins with a strong Soret band centered at 430 nm and less intense Q–bands that extend from ca. 520 nm to ca. 650 nm. The Soret band corresponds to the electronic transition $S_0 \rightarrow S_2$ and Q–bands arise from the electronic transition $S_0 \rightarrow S_1$. Porphyrins are also photochemically and thermally stable. But one particularly interesting property of porphyrins is the sensitivity of their electronic structure to substitutions at peripheral positions, namely *α, β* and *meso* (Figure 2.5). Substitutions at these positions perturb their conjugated electronic system and result often in unusual electronic and optical properties. In particular, in multiporphyrin arrays, such perturbations enable to access a wide absorption range from visible to the near–infrared region of the spectrum. Moreover, the redox properties of the free–base porphyrin can easily be tuned by coordination of metal cations generating derivatives with good electron donor or acceptor properties. In the last decade, the versatile, unusual electronic and optical behavior of biomimetic porphyrin–based systems has attracted much interest. A wide range of multiporphyrin systems have been synthesized in view of potential applications in artificial photosynthesis, molecular electronics and non–linear optics.[122] Yet another interesting property is their ability to self–assemble via π–π and/or metal–ligand interactions. This enables to create large ordered arrays with architectures going from simple linear structures to cyclic[123] and box[124-126] structures. Finally, the large size of the porphyrin macrocycle (~24 Å) allows for building molecular wires covering longer distances with a minimum of covalent linkages. This, in addition with their relatively

simple synthesis, makes multiporphyrin arrays particularly interesting systems for long–range electron and energy transport studies.

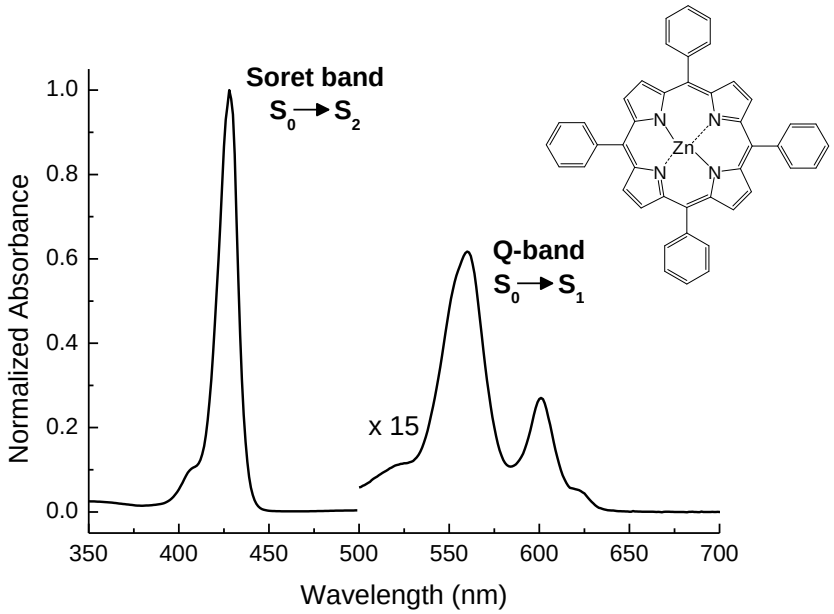

Figure 2.6 Ground–state absorption spectrum of zinc tetraphenylporphyrin (**ZnTPP)** in toluene. Inset: Molecular structure of **ZnTPP**.

2.4.2 PORPHYRIN–BASED MOLECULAR WIRES

To construct multiporphyrin arrays, individual porphyrins may be connected either directly to each other or using a linker. Over the last 40 years, a multitude of linear multiporphyrin arrays have been synthesized, whose structures vary essentially in the type of linker and the porphyrin linkage topology (i.e. *α*, *β* or *meso*). As linkers, mostly conjugated motifs have been employed including phenyls,[127-128] alkenes[129] or alkynes[108, 130-131] since they enable to some extent electronic interactions between neighboring porphyrins. In these multiporphyrin systems, special emphasis has been put on establishing structure–property relationships. In particular, it has been shown that both the type of linker and the porphyrin linkage topology govern the dihedral angle between neighboring porphyrins, and hence the inter–porphyrin electronic communication and their photophysical properties.[114, 132]

As the simplest way to assemble linear porphyrin oligomers, directly *meso–meso* linked porphyrin oligomers have been thoroughly investigated by Osuka and co-workers.[133] In these oligomers, the porphyrins are not strongly conjugated. Indeed, steric hindrance with the *β*–substituents pushes the individual porphyrins in a nearly–orthogonal arrangement. Such orthogonal arrangement precludes orbital interactions between the porphyrins, and leads to a disruption of the π-conjugation along the porphyrin oligomers. As a result, through–space electronic communication, i.e. exciton coupling, dominates in these weakly conjugated systems and governs their photophysical properties. This exciton coupling arises from the coulombic interaction between

transition dipole moments of adjacent porphyrins and can be viewed as their collective behavior. In the oligomers containing of two or more units, exciton coupling simply manifests by spectral changes in the Soret bands of their absorption spectra. The Soret band splits into two bands whose energy and relative intensity depend on the number of porphyrin units. As illustrated in Figure 2.7, such splitting can be explained by the molecular exciton theory developed by Kasha in the point dipole approximation.[134] Considering first the zinc porphyrin monomer, two perpendicular and degenerate transitions, denoted B_x, B_y contribute to the Soret band. Addition of a second porphyrin at the *meso* position leads to four transition dipole moments that may contribute to the Soret band. According to Kasha's exciton model, the transition moment is then given by the different combinations of these individual transition dipole moments. However, taking into account the orthogonality of the porphyrin planes, three transitions are allowed: B_x, B_y and B_z. While the two electronic transitions B_x, B_y remain degenerate, the electronic transition B_z is red–shift with respect to B_x, B_y due to exciton coupling arising from the coplanar head–to–tail (→ →) configuration of the transition moments, hence the splitting of the Soret band.

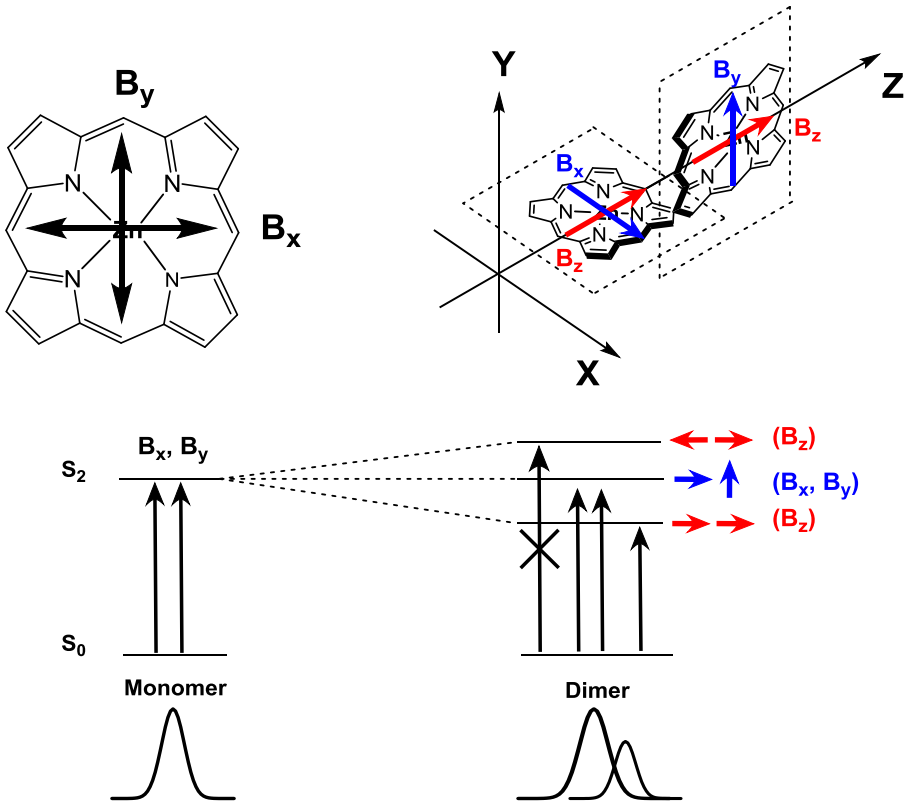

Figure 2.7 Schematic diagram of exciton coupling in directly *meso–meso* linked zinc porphyrins. Adapted with permission from ref 135. Copyright (2009) American Chemical Society.

By appending an energy acceptor to directly linked porphyrin oligomers of different lengths, Osuka and co–workers investigated also their ability to function as molecular photonic wire for energy transfer.[133] Their results revealed remarkably fast excitation

energy transfer with rate constants varying from $(2.5\ ps)^{-1}$ for the monomer to $(108\ ps)^{-1}$ for the 24–mer covering a distance of ~109 Å (~11 nm). In this regard, directly linked porphyrin oligomers successfully resemble the natural antenna complexes where fast excitation energy migration occurs despite negligible electronic delocalization due to a lack of bonds between individual chromophores. Fast and efficient energy transfer in multiporphyrin arrays due to excitonic interactions was also demonstrated by Lindsey and co–workers. They designed molecular photonic wires for energy transfer consisting of *meso–meso* diphenylethyne–linked porphyrin oligomers.[128, 136] Likewise directly linked porphyrin arrays, adjacent porphyrins in these oligomers adopted an orthogonal configuration that minimized electronic delocalization and prevented competitive electron transfer quenching to occur.

Although weakly conjugated porphyrin oligomers are promising candidates for molecular photonics applications, disruption of the π–conjugation in these oligomers is a considerable obstacle to long–range charge transport. Electrons or holes are very unlikely to travel long distance via through–space interactions. Instead their transport requires through–bond electronic communication. Thus, porphyrin oligomers need to be assembled using conjugated motifs that favor the extension the π–conjugation over the entire oligomer. In this effort, different strategies have been employed that again differ by the linker motif and the porphyrin linkage topology (*β–β*, *meso–meso*, *meso–β*). For example, the groups of Therien[130] and Anderson[131] synthesized zinc porphyrin dimers linked at their *meso* position by ethyne and butadiyne linkers, respectively (Figures 2.8A and 2.8B). In both cases, this type of bond linkage allows a coplanar arrangement of the porphyrin macrocycles, and hence merging of the π–conjugated system of individual components along the entire dimers. This leads to a strong interporphyrin electronic coupling (i.e. electronic delocalization) in the ground state. Such electronic delocalization effects manifest by a strong alteration of the Q–band in the ground–state absorption spectra of these oligomers. Upon lengthening of the oligomer, the Q–band gradually red-shifts and intensifies.[132] In the excited state, electronic delocalization is further enhanced due, to on average, more planar conformation of the oligomers with respect to their ground state.[137-138] Influence of the porphyrin linkage topology on the electronic coupling in ethyne–and butadiyne–linked porphyrin dimers was also investigated by Therien et al., which demonstrated that the *meso–meso* connectivity always offered larger π–overlap, hence maximal electronic coupling.[132] Other strategies used to form strongly conjugated porphyrin oligomers consist in fusing individual porphyrins either directly by triple *meso–meso*, *β–β*, *β–β* bonds[139] or via an aromatic linker.[140-141] In the literature, these porphyrin oligomers are often referred as to "porphyrin tapes". In particular triply linked *meso–meso*, *β–β*, *β–β* porphyrin arrays have been synthesized and investigated by the group of Osuka (Figure 2.8C). In contrast to alkyne-linked porphyrin oligomers, porphyrin tapes, as their name implies, are strictly planar oligomers and displayed even stronger electronic delocalization with Q–bands red–shifted up to ca. 3000 nm for a 12–mer fused array.

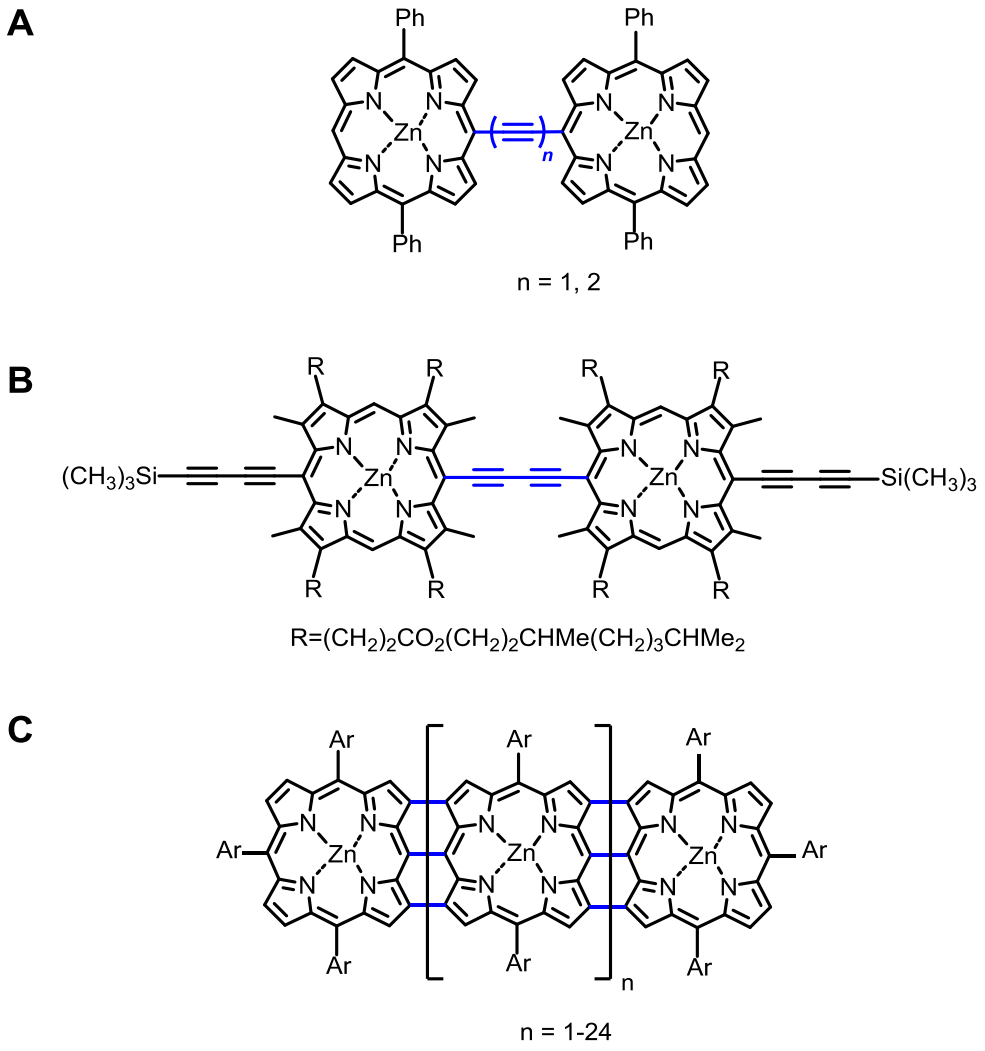

Figure 2.8 Molecular structures of strongly conjugated porphyrin oligomers synthesized by the groups of (A) Therien,[130] (B) Anderson[131] and (C) Osuka.[111] Adapted from Ref. 79 with permission from The Royal Society of Chemistry.

Alkynes and alkene–linked porphyrin oligomers have demonstrated ability to mediate electron transfer over long distances. This has been characterized experimentally by several groups.[93, 142-146] For example, hole delocalization over more than 50 Å in a *meso–meso* ethyne–linked porphyrin pentamer has been reported by Therien and co-workers.[142] Our group investigated electron transfer processes in a homologous series of D–B–A systems $\mathbf{Fc^{\bullet+}–P_n–C_{60}^{\bullet-}}$ (n = 1, 2, 4) where $\mathbf{P_n}$ designate *meso–meso* butadiyne–linked porphyrin oligomers, $\mathbf{P_n}$ (n = 1, 2, 4), to bridge a ferrocene electron donor and a fullerene electron acceptor. In these series, charge recombination of $\mathbf{Fc^{\bullet+}–P_n–C_{60}^{\bullet-}}$ revealed to be remarkably efficient even for the tetramer (R_{DA} = 65 Å). Recently, electron transfer studies in single–molecule wires have become more and more *en vogue* to characterize the charge transport properties of molecular wires. In these studies, the molecular conductance is measured, a property which can be related to the electronic coupling in D–B–A molecules. The molecular conductance is probed by direct electrical measurements by placing single molecules between two metallic

contacts, typically an STM tip and a metal surface.[147-148] In particular, Nichols and co–workers have measured the conductance of single butadiyne–linked porphyrin oligomers and demonstrated their wire–like behavior ($\beta = 0.04$ Å^{-1}).[143-144] In a similar work, the group of Therien have shown the quasi–ohmic behavior of ethyne–linked porphyrin oligomers.[146] Although this type of electron transfer studies have shown some similarities with photo–induced electron transfer studies in the parameters influencing charge transport (i.e. tunneling energy barrier and conformational orientation), electron transfer in single–molecules wires remains a distinct subject with its own challenges.[149-150]

3 THEORY

The World would be rather bland without color. Absorption and reflection of light by objects shape daily our vision of the world. Light–matter interactions are also essential to life; as we have seen in chapter 2, the natural photosynthesis is initially triggered by light absorption. In this chapter, focus is on how light interacts with matter and on the processes that may follow light absorption. By light, I designate radiated energy that can cause electronic excitation, i.e. promote a molecule from its electronic ground state to one of its electronic excited states. In terms of wavelength, λ, this corresponds to the region that extends from the near UV to the visible region to the near IR, i.e. λ between 200 nm and 1000 nm. First, the criteria for absorption are briefly stated, and then the fate of electronically excited states is discussed. Finally, a short introduction to electron and energy transfer theory is given. For a more in–depth description of concepts in photophysics and the energy and electron transfer theories, please see e.g. the text–books by Hollas,[151] Atkins[152] and Balzani.[153-154]

3.1 LIGHT–MATTER INTERACTIONS

Absorption of light by a molecule A in its electronic ground state, can be described by the following reaction,

$$A + hc/\lambda \rightarrow A^* \qquad 3.1$$

where A^* represents the molecule in an electronically excited state. The absorbed photon is represented by its energy given by hc/λ, where h is the Planck's constant, c the speed of light and λ the wavelength. For reaction 3.1 to occur, several criteria need to be fulfilled.

Molecules consists of atoms, which themselves consist of nuclei and electrons. By treating molecules quantum mechanically, their electronic configuration can be described by a set of stationary electronic states with discrete energy. Associated to each of these stationary states is a wave function Ψ_i. Solving the Schrödinger's equation (equation 3.2), i.e. determining Ψ_i, gives access to the energy of each stationary state.

$$\hat{H}_0 \Psi_i(r) = E \Psi_i(r) \qquad 3.2$$

where $\hat{H}_0$ is the energy or Hamiltonian operator and represents the sum of the kinetic and potential energies of both electrons and nuclei of the molecule. This distribution of electrons into discrete energy levels leads to the first criterion for light absorption (equation 3.3): the energy of the incident photon must match the energy difference between an initial (*i*) and a final state (*f*) of the molecule. This first criterion is often referred to as the Einstein–Bohr's frequency condition or resonance condition.

$$hc/\lambda = \Delta E = E_f - E_i \qquad 3.3$$

where E_i and E_f designate the energies of an initial (*i*) and a final state (*f*) of the molecule, respectively. This first criterion gives the energy of the electronic transition or wavelength at which the measured absorption spectrum of the molecule may display an absorption band (*vide infra*). It also explains why increasing light intensity does not affect the wavelength of absorption. While this condition is necessary, it solely does not suffice for light absorption. Further, it does not provide any information on the probability for the electronic transition to occur (i.e. intensity of the transition). In other words, it lacks explanation on why some transitions are strong (i.e. allowed) and why some transitions are barely observable (i.e. forbidden).

In reaction 3.1, light is considered as a flow of individual photons. Considering now its undulating nature, light is described as a continuum of waves or electromagnetic radiation characterized by an electric ($\vec{E}$) and magnetic ($\vec{B}$) field oscillating in time and space in directions perpendicular to each other and to the direction of light propagation. Light can through its electrical component strongly interact with distribution of charged particles such as loosely bonded valence electrons (i.e. outer electrons) in molecules. This may result in a distribution of charges that differs from the one in absence of light, leaving the molecule with a different overall electronic configuration. Such small perturbation of the charge distribution induced by light can be described using time–dependent perturbation theory. Light absorption is approximated by applying a small perturbation to the system and equation 3.2 can be re–written with an additional perturbation operator $\hat{H}'$.

$$(\hat{H}_0 + \hat{H}')\Psi_i(r, t) = E\,\Psi_i(r, t) \qquad 3.4$$

The wave–function Ψ_i (r, t) describing the electronic state of the molecule is now time–dependent. The perturbation operator $\hat{H}'$ is expressed as a scalar product of $\vec{E}(t)$ and the dipole moment operator $\hat{\mu}$ which represents the spatial charge distribution of the molecule according to equation 3.6.

$$\hat{H}' = \left|\vec{E}(t) \cdot \hat{\mu}\right| \qquad 3.5$$

$$\hat{\mu} = e \sum_{j}^{N} q_j \vec{r}_j \qquad 3.6$$

where q_j is the charge of the particle *j* and $\vec{r}_j$ its position vector distance. From equations 3.5 and 3.6, one can state the second criterion for light absorption: the probability of the transition to occur is maximal when the electric field component of the incident light and the dipole operator of the molecule (i.e. dipole induced by light in the molecule) point towards the same direction.

Here the perturbation, i.e. the electric field, disturbs rather weakly the system that is the energies of the stationary electronic states remain unaffected. As a result, the

time–dependent wave function may be expressed as a linear combination of the wave functions of the unperturbed system, as shown in equation 3.7,

$$\Psi(r, t) = \sum a_k (t)\ \Psi_i (r) \qquad 3.7$$

where the coefficients $a_k (t)$ "carry" the time–dependence. When the perturbation is removed, the system may occupy an electronic final state $\Psi_f (r)$ which differs from the initial one described by $\Psi_i (r)$ (i.e. before perturbation). The probability P_{fi} to find the system in a final state $\Psi_f (r)$ is given by the square of the corresponding coefficients $[a_f (t)]^2$, which is proportional to the square of the integral $\int \Psi_f (r)\ \hat{\mu}\ \Psi_i (r)\, d\tau$ taken over all space.

$$P_{fi} \propto \left| \int \Psi_f (r)\ \hat{\mu}\ \Psi_i (r)\, d\tau \right|^2 = \left| \vec{\mu}_{fi} \right|^2 \qquad 3.8$$

In equation 3.8, the integral is the so–called transition dipole moment $\vec{\mu}_{fi}$ which can be viewed as a dipole induced by light represented by a vector aligned in the direction of the electron flow. From equation 3.8, the third criterion for a transition to occur can be derived, that is the integral $\int \Psi_f (r)\ \hat{\mu}\ \Psi_i (r)\, d\tau$ (i.e. $\vec{\mu}_{fi}$) should be non–zero. Mathematically, it can be shown that this integral over all space will vanish if the product under the integral is an antisymmetric function and will not vanish for a symmetric function. Here, for electronic transitions, the symmetry of $\Psi_f (r)$ and $\Psi_i (r)$ is related to the symmetry of the orbitals, which can be determined using Group Theory. Moreover, since the dipole moment operator $\hat{\mu}$ is a vector in the x or y or z directions, all its components are antisymmetric functions. Thus, based on the symmetry of the overall product $\Psi_f (r)\, \hat{\mu}\, \Psi_i (r)$, it is possible to determine if a transition is allowed or forbidden. In addition, if the integral $\int \Psi_f (r)\ \hat{\mu}\ \Psi_i (r)\, d\tau$ is large, the transition will be highly probable (i.e. strong), while barely observable for a small overlap of its three components.

From the above discussion, three criteria have been identified as governing the probability for an electronic transition to occur, i.e. intensity of absorption band. Taking solely these criteria into account, this leads to all the intensity of a transition concentrated in a sharp band. However, this is generally not what is observed in molecules. Instead, the absorption bands have often their intensity spread out over a wide range of wavelength. This can be understood by introducing the Franck–Condon factor. In between the electronic stationary states lie also more closely spaced levels, namely the vibrational levels of the molecules (see the Jablonski diagram in Figure 3.1). At room temperature, the molecules populate mainly the lowest vibrational level of the ground state. However, upon light absorption, the energy of the photon is sufficient enough that molecules are not only promoted to higher electronic states but also to higher vibrational levels in the excited state. This means that in the expression of the transition dipole moment (equation 3.8), the overlap between the vibrational (nuclear) wave functions of the two states involved in the transition must also be taken into

account. This renders the picture drawn above slightly more complex. However, one may recall the time scale at which light absorption takes place. Light absorption, i.e. rearrangement of the electron distribution, occurs on a time scale of ~10^{-15} s that is much faster than vibrational motions (10^{-12} s). Thus the nuclei positions remain identical before and after light absorption (Condon approximation). Under this condition, the transition dipole moment may be expressed using the well–known Born Oppenheimer approximation. Under this approximation, one may separate nuclear and electronic motions and re–write the overall wave function $\Psi_i(r, R)$ as a three–component product where R designate the nuclear coordinates and r the electron coordinates: electronic $\varphi_i(r, R)$, nuclear $\theta_i(R)$ and spin S_i.

$$\Psi_i (r, R) = \varphi_i (r, R) \cdot \theta_i (R) \cdot S_i \qquad 3.9$$

Since the nuclei positions remain the same before and after light absorption, in the expression of the transition dipole moment, $\hat{\mu}$ only applies to the electronic wave function. The expression for $\vec{\mu}_{fi}$ becomes then,

$$\vec{\mu}_{fi} = \int \varphi_i (r, R)\, \hat{\mu}\, \varphi_f (r, R)\, d\tau_e \int \theta_i(R)\, \theta_f (R)\, d\tau_N \int S_i S_f d\tau_S \qquad 3.10$$

From equation 3.10 one can visualize which terms determine the integrated intensity (i.e. probability) and the shape of the absorption band. In the first term, one recognizes the electronic transition moment. The third term is the spin integral overlap, i.e. the overlap between the spin wave functions of the initial and final states. Since the spin wave functions of states with different multiplicity (e.g. singlet and triplet) are orthogonal, this integral will vanish whenever the transition implies a change in spin multiplicity and the transitions are said to be spin–forbidden. For example, this integral will be zero for singlet → triplet transitions, leading to the overall cancellation of the transition dipole moment for these transitions. Both, the first and third terms contribute the integrated intensity of the absorption. The second term is the so–called Franck–Condon factor. This term "carries" the responsibility for the shape of the absorption band. It corresponds to the vibrational (nuclear) overlap between the vibrational excited state wave function and the ground state lowest vibrational level wave function. If the potential energy surfaces of the ground state and excited state were identical, this term will sum up to 1 and all the intensity of the transition will be concentrated in a sharp band corresponding to the vertical transition 0–0 (i.e. between the lowest vibrational levels of the excited and ground states). However, this is generally not the case in molecules, where both the bond strength and the geometry of the excited state are often different from the ground state. Vibronic excitation (vibration and electronic excitation) of the molecule gives raise instead to a vibronic absorption band structure, i.e. a distribution of the integrated intensity of the electronic transition over several vibronic peaks. The intensity of each vibronic peak is related to the Franck–Condon factor and depends on the overlap between the nuclear wave functions of the corresponding excited and ground state vibrational levels. For an example of

absorption spectra showing clear vibronic structure of the absorption band, see e.g. the absorption spectra of the anthracene dendrimers (Figure 6.2). Note that such a vibronic structure of the absorption band often vanishes due to temperature and solvent effects. Finally, some forbidden transitions may have a substantial intensity due to break down of the Condon approximation and vibronic coupling.

3.2 THE ELECTRONIC EXCITED STATE AS A NEW MOLECULE

The electronic excited state is energy–rich compared to the ground state. To have an idea of the energy gain in the excited state, it is useful to look at the photon energy. The photon energy ranges from 4.41×10^{-19} J to 2.36×10^{-19} J for the excitation wavelength range 450–840 nm used in this work. For comparison to chemical bond energies, one may express the photon energy in kJ per mole of photons. This corresponds to 266 kJ/mol at 450 nm and to 142 kJ/mol at 840 nm. Such energies are of the same order of magnitude as bond energies, e.g. 413 kJ/mol for C–H, 348 kJ/mol for C–C, 293 kJ/mol for C–N. Thus it is no surprise that the behavior of the excited state may strongly differ from the ground state. In regard to its different charge distribution and high energy content, the electronic excited state can be viewed as a new molecule with distinct photo–physical (e.g. absorption spectrum), reactivity (e.g. association) and redox properties. The high energy content of excited states also renders excited states molecules much less stable than ground–state molecules. They can deactivate by several photochemical and/or photophysical processes. According to the gold book of IUPAC, photochemical processes refer to chemical reactions that occur in the electronically excited states (e.g. isomerization) and are caused by light absorption while photophysical processes designate processes in which relaxation of the excited state occurs through radiation and/or radiationless transitions without any chemical change.[155] In my work, deactivation of the electronic excited states mostly occurs via photophysical processes, while quenching (i.e. electron transfer) is classified as a photochemical process. The following section only presents photophysical deactivation processes, while keeping in mind that electron transfer may compete with these processes depending on the system studied.

3.2.1 EXCITED–STATE DEACTIVATIONS

A common way to present photophysical deactivation pathways of electronically excited states is using a schematic energy–level diagram, so–called Jablonski diagram (Figure 3.1).[156]

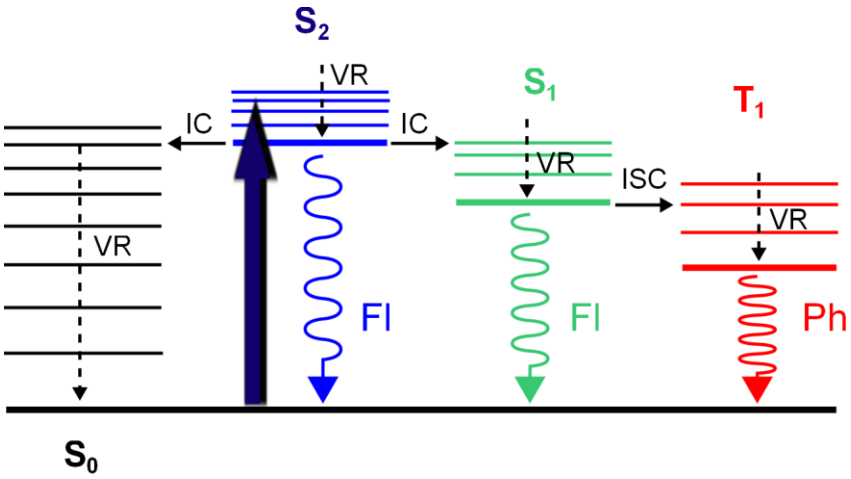

Figure 3.1 Jablonski diagram showing non–radiative (→) and radiative (⇝) deactivation pathways for an excited state. Here, upon light absorption, the molecule initially in a singlet ground state S_0 is promoted to higher vibrational levels of the second singlet excited state S_2. The abbreviations are explained in the text.

In their ground state, most molecules are singlets accordingly denoted S_0 where all electron spins are paired. The electronic excited states populated by photo–excitation are also singlets (*vide supra*) denoted S_1, S_2… The more closely spaced levels associated to each electronic state are the vibrational levels. Depending on the energy of the absorbed photon, the initially populated excited state is either the n–vibrational level of S_1 or S_2…. The molecule first dissipates its excess of energy via fast vibrational relaxation mechanisms (VR) and populates lower vibrational levels of the excited state according to a Boltzmann distribution. The energy is lost as heat through collisions with the surrounding molecules or the solvent. In solution, VR is quite fast, i.e. from tens of femtoseconds to tens of picoseconds. This means that, in general, all other deactivation processes occur from the equilibrated excited states. The excess of energy is then released via different competing deactivation pathways classified into non–radiative and radiative processes. Internal conversion (IC) and intersystem crossing (ISC) are both non–radiative decay processes and do not imply absorption or emission of photon. They occur between isoenergetic vibrational levels of different electronic states, hence no energy is lost. The resulting state is a vibrationally excited state that further relaxes via vibrational relaxation. Thus, IC and ISC are represented as horizontal arrow lines (→) in the Jablonski diagram. Difference between IC and ISC lies in the spin state of the levels involved. Internal conversion moves the molecule between isoenergetic vibrational levels of electronic states of the same multiplicity: for example, $S_1 \rightarrow S_0$ in Figure 3.1. In contrast to IC, intersystem crossing involves electronic states of different multiplicity. For example, from the S_1 state, the molecule can spin flip its electron and move to the triplet excited state T_1. The probability of IC and ISC processes (i.e. the rates) is dependent on the Franck–Condon factor and the spin overlap (*vide supra*). Since the change of spin in transitions is formally forbidden, intersystem crossing (i.e. $S_1 \rightarrow T_1$) is much slower than internal conversion (i.e. $S_1 \rightarrow S_0$).

Competing with the non–radiative IC and ISC are radiative processes that lead to emission of photons. Radiative processes involve vertical transitions (⇝) between electronic excited states and the ground state. The excess energy is released in the form of photons with energy matching the energy difference between the two electronic states. Once more, one distinguishes photon emission from transitions between states of same spin multiplicity and different spin multiplicity. Singlet emission such as e.g. $S_1 \rightsquigarrow S_0$ is called fluorescence (Fl) and takes place on the nanosecond time scale. Photon emission occurring from a triplet state, such as $T_1 \rightsquigarrow S_0$ is called phosphorescence (Ph). Similar to intersystem crossing (*vide supra*), triplet emission is a spin–forbidden transition, hence less probable and much slower (i.e. typically microseconds to milliseconds or even seconds for organic molecules). In Figure 3.1, note that photon emission is voluntarily represented as potential deactivation pathway only from S_1 and T_1. Indeed, due to usually fast internal conversion processes within each high excited state (S_n, T_n, n> 1) and fast vibrational relaxation, *the emitting level of a given multiplicity is the lowest excited level of that multiplicity (*Kasha's rule[157]). While most molecules obey this rule, exceptions exist, e.g. azulene,[158] some porphyrins[159] and some phthalocyanines[160] for which emission from the S_2 state is observed.

In the special case of a donor–acceptor couple, the donor excited state may be quenched via energy and/or electron transfer to the acceptor. In that sense, the excess energy stored in the excited state may be used to perform reactions which thermodynamically will not be possible from the ground state. For example, in the natural photosynthesis, the energy stored in the excited states triggers a cascade of electron transfer steps that ultimately results in a charge–separated state with sufficient energy for water splitting and carbon dioxide reduction (*vide supra*).

3.2.2 RATES, LIFETIMES AND QUANTUM YIELDS

We have seen that Jablonski diagrams are particularly useful to map the different pathways that deactivate electronically excited states. Highlighted by such energy level diagrams is also the competition between these pathways. Whether the excited state will follow a particular pathway *i* will depend on the relative probability of this pathway with respect to the others. For an ensemble of molecules, this is the rate constant k_i of the pathway *i* with respect to others that tells us about the probability of this pathway to occur (i.e. a transition). Intimately linked to the rate constants of the different deactivation pathways is the lifetime τ of the excited state.

All deactivation pathways presented in Figure 3.1 are intramolecular reactions, hence assuming first–order decay of the excited state population $N(t)$ as in equation 3.11 is appropriate.

$$\frac{dN(t)}{dt} = -\sum_j k_j \, N(t) = -\frac{N(t)}{\tau} \qquad 3.11$$

$\sum_j k_j$ is the sum over all the rate constants that depopulate the excited state. According to equation 3.11, the lifetime τ can be expressed as

$$\tau = \frac{1}{\sum_j k_j} = \frac{1}{k_f + \sum k_{nr}} = \frac{1}{k_f + k_{IC} + k_{ISC}} \qquad 3.12$$

In equation 3.12, k_f is the fluorescence rate constant. $\sum k_{nr}$ represents the sum over the rate constants of non–radiative processes. In Figure 3.1, this sum consists of k_{IC} the rate constant of internal conversion and k_{ISC} the rate constant of intersystem crossing. The probability of the excited state to deactivate through the given process *i*, i.e. quantum yield of the deactivation process *i*, denoted Φ_i, is then given by,

$$\Phi_i = \frac{k_i}{\sum_j k_j} = k_i \times \tau \qquad 3.13$$

Most non–radiative processes have rate constants and quantum yields that are not directly accessible experimentally. In constrast, radiative processes, i.e. fluorescence and phosphorescence can be experimentally measured. Photon emitted from electronically excited states can not only be detected but also counted using different experimental techniques named fluorescence spectroscopy. Further experimental details on fluorescence spectroscopy are given in chapter 4. From such experiments, two quantities are often determined: the fluorescence lifetime τ_f and the fluorescence quantum yield Φ_f. τ_f describes how fast the fluorescence intensity of an ensemble of molecules decays over time, while Φ_f represents the number of photons emitted per photons absorbed. Both are directly related to the radiative rate constants and the sum of the non–radiative rate constants through equations 3.14 and 3.15. Combining both equations enable to evaluate k_f and k_{nr} from the experimental values of Φ_f and τ_f, according to equations 3.16 and 3.17, respectively.

$$\Phi_f = \frac{k_f}{\sum_j k_j} = \frac{k_f}{k_f + \sum k_{nr}} \qquad 3.14$$

$$\tau_f = \frac{1}{k_f + \sum k_{nr}} \qquad 3.15$$

$$k_f = \frac{\Phi_f}{\tau_f} \qquad 3.16$$

$$k_{nr} = \frac{(1 - \Phi_f)}{\tau_f} \qquad 3.17$$

Indirectly fluorescence spectroscopy can also provide valuable information on electron and energy transfer processes in donor–acceptor systems. The excited state is then further depopulated by energy or electron transfer. In equations 3.14 and 3.15, $\sum k_{nr}$ increases due to the additional reaction rates associated to energy or electron transfer. It results in both a lower fluorescence quantum yield and a shorter fluorescence lifetime compared to the same molecular system without acceptor group.

3.3 ELECTRON TRANSFER THEORY

The electron transfer (ET) reactions described in this thesis are intramolecular electron transfer reactions. In electron donor–acceptor (D–A) systems, this reaction consists of the transfer of an electron between the electron donating (D) and accepting (A) parts of the molecular system. In this work, ET reactions are triggered using light excitation by selectively exciting either the donor or the acceptor. These reactions are called photoinduced electron transfer reactions and can be described by the following reaction,

$$D\text{–}A + hc/\lambda \rightarrow D^{*}\text{–}A \xrightarrow{k_{ET}} D^{\bullet+}\text{–}A^{\bullet-} \qquad 3.18$$

Here, the donor is initially excited and the ET reaction is the transfer of an electron from the donor excited state D^{*} to the ground state acceptor A. The product of the ET reaction is the charge–separated state, $D^{\bullet+}$–$A^{\bullet-}$.

3.3.1 MARCUS THEORY

Just as chemical reactions, electron transfer reactions can be described by motion of atoms along potential energy surfaces. Here, the potential energy surfaces are the ones of the photo–excited reactant D^{*}–A and the ET product $D^{\bullet+}$–$A^{\bullet-}$ (reaction 3.18) as function of the reaction coordinate (Figure 3.2). The reaction coordinates include the vibrational (nuclear) coordinates of the reacting molecules and the position and orientation of the solvent molecules. Since electron transfer is a dark reaction, it will only occur at the configuration of the reacting system (reaction coordinate/potential energy) that satisfies both energy conservation and Franck–Condon conditions. These conditions are fulfilled at the crossing point between the two surfaces, the so–called transition state TS. Indeed at the TS, both the reactant and the product have classically the same energy. Moreover, the transfer occurs at fixed positions of the atoms, and hence the Franck–Condon principle is also satisfied. At the transition state, the electronic coupling between the donor and the acceptor, V_{DA} causes a splitting of the two surfaces (Figure 3.2). The extent of this splitting, i.e. the electronic coupling will in part determine the probability of D^{*}–A to cross over the "mountain pass" and form $D^{\bullet+}$–$A^{\bullet-}$. Other factors intervene in an electron transfer "journey". At the beginning of the ET journey, the reacting D^{*}–A is in a valley (the lower left region of Figure 3.2). Hence to reach TS, D^{*}–A needs to first distort along the reaction coordinate from its equilibrium position to the transition state, i.e. changes in bond lengths. This requires energy called activation energy, $\Delta G^{\neq}$. Formation of $D^{\bullet+}$–$A^{\bullet-}$ is also characterized by a change in dipole moment with respect D^{*}–A. As pointed out first by Libby,[161] this charge–separated state is formed initially in a "unsuitable" solvent environment, i.e. the surrounding solvent molecules do not have time to rearrange on the short time scale of ET to accommodate the changes in polarization. Reorganization of the solvent molecules to bring $D^{\bullet+}$–$A^{\bullet-}$ to its equilibrium state again requires energy that is involved

in the reorganizational energy denoted λ. In Figure 3.2, λ corresponds to the energy to bring the reactant to the nuclear and solvent configuration of the final (i.e. equilibrated) product. Finally, the rate of electron transfer will depend on the driving force or standard free energy of the reaction, ΔG^0.

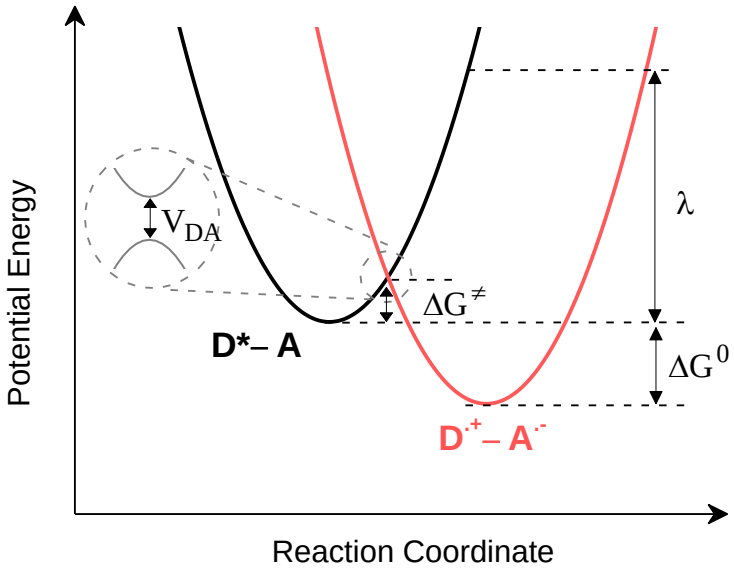

Figure 3.2 Schematic of the potential energy surfaces of the initial state and the charge–separated state showing the factors governing electron transfer processes: the driving force ΔG^0, the activation energy $\Delta G^{\neq}$, the reorganizational energy λ and the electronic coupling V_{DA}.

Depending on the extent of splitting or electronic coupling V_{DA}, electron transfer reactions are classified into adiabatic and diabatic. When there is sufficient electronic coupling between the donor and the acceptor, large splitting of the potential energy surfaces at TS results in a lower surface and an upper surface. At TS, D^*–A then moves along the lower surface from the reactant to the product side. These electron transfer reactions are called adiabatic reactions and are not further discussed in this thesis. When V_{DA} is instead very weak (diabatic ET reactions), crossing from the lower surface on the reactant side to the lower one on the product side becomes less probable. For weak electronic coupling, the rate of transition between two potential energy surfaces may then be predicted by the Fermi Golden Rule,

$$k_{if} = (2\pi/\hbar)\, V_{if}^2\, FCWD \qquad 3.19$$

In equation 3.19, V_{if} is the overlap integral between the wave functions of the initial and final states upon a small perturbation coupling these two states. FWCD is the Franck–Condon weighted density of states. It describes the influence of nuclear (i.e. vibrational) modes. Assuming that the potential energy surfaces of D^*–A and $D^{\bullet+}$–$A^{\bullet-}$

are parabolas with equal curvatures, Marcus predicted that the appropriate Fermi Golden Rule leads to[162-163]

$$k_{ET} = \sqrt{\frac{\pi}{\hbar^2 \lambda k_B T}} V_{DA}^2 \exp\left(-\frac{(\Delta G^0 + \lambda)^2}{4\lambda k_B T}\right) \qquad 3.20$$

with the activation energy $\Delta G^{\neq}$ is equal to $(\Delta G^0 + \lambda)^2/4\lambda$.
The photoinduced electron transfer reactions investigated in this work involve weakly coupled donor–acceptor systems and hence are considered under non–adiabatic conditions. Thus, the Marcus equation referred to in Papers I–II is equation 3.20.

Another prediction of Marcus is the inverted region which derives from the quadratic dependence of the activation energy on the sum of the driving force and reorganization energy.[164] Looking at the variation of $\Delta G^{\neq}$ with ΔG^0: when ΔG^0 is decreased from zero to a negative value, the activation energy decreases, until it fully vanishes for $\Delta G^0 = -\lambda$. However, when the driving force becomes even more negative, i.e. $\Delta G^0 < -\lambda$, the activation energy starts to increase again. The decrease of $\Delta G^{\neq}$ with increasingly negative ΔG^0 is the expected trend in chemical reactions and is often referred to as the normal region in ET. However, the increase of the activation energy for large driving forces was quite surprising and was termed "the inverted region". Both regions can be visualized in Figure 3.3 along with the consequences on the resulting electron transfer rates (i.e. plot of $\ln k_{ET}$ as a function of ΔG^0). Clear experimental evidence of the inverted region has been long time lacking although theoretically predicted. The first experimental evidence of the inverted region was provided in the mid–80s by Closs and Miller.[165-166]

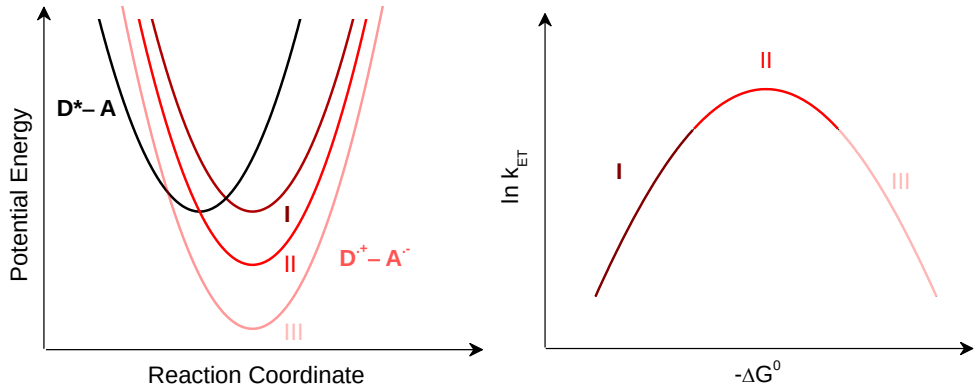

Figure 3.3 Schematic of (left) the potential energy surfaces of the excited states D^*–A and $D^{\bullet+}$–$A^{\bullet-}$ and the charge–separated states $D^{\bullet+}$–$A^{\bullet-}$ for different ET regimes with (**I**) $\Delta G^0 > -\lambda$, (**II**) $\Delta G^0 = -\lambda$ and (**III**) $\Delta G^0 < -\lambda$; (right) the corresponding variation of the ET rate, $\ln k_{ET}$ with $-\Delta G^0$.

The driving force

As illustrated in Figure 3.2, the driving force, ΔG^0 corresponds to the energy difference between the lowest vibronic levels of the donor excited state D^*–A and the charge separated state $D^{\bullet+}$–$A^{\bullet-}$. Forming $D^{\bullet+}$–$A^{\bullet-}$ from D^*–A is downhill in energy. The system loses energy ($\Delta G^0 < 0$), and hence ET is thermodynamically favorable from photoexcited states. In contrast, the same reaction from the ground state will be highly unlikely to occur. ΔG^0 may be estimated from the redox potentials of the donor/acceptor couple and from the energy stored in the excited state using the Rehm–Weller equation,[167]

$$\Delta G^0 = e\,(E_{ox} - E_{red}) - E_{0\text{–}0} - \frac{e^2}{4\pi\varepsilon_0 R_{DA}} + \frac{e^2}{4\pi\varepsilon_0}\left(\frac{1}{\varepsilon_S} - \frac{1}{\varepsilon_S^{ref}}\right)\left(\frac{1}{2R_D} + \frac{1}{2R_A}\right) \qquad 3.21$$

where E_{ox} is the oxidation potential of the donor and E_{red} is the reduction potential of the acceptor. $E_{0\text{–}0}$ is the energy of the 0–0 transition of the donor, i.e. the energy difference between the thermally relaxed excited state and ground state of the donor. The oxidation and reduction potentials can be experimentally determined by e.g. cyclic voltammetry. $E_{0\text{–}0}$ can be estimated spectroscopically, preferably from the wavelength corresponding to the intersection of the normalized absorption and emission spectra. The third term in equation 3.21 is a coulombic stabilization term, and hence a function of the inverse of the donor–acceptor distance, R_{DA}. Finally, the fourth term is a correction factor that may be used when electrochemical and spectroscopic measurements are carried out in different solvents. ε_S and ε_S^{ref} are the dielectric constants of the solvent in which the spectroscopic and electrochemical measurements were conducted, respectively. R_D and R_A are the radii of the donor and acceptor, respectively.

The reorganization energy

Both the reactant and solvent nuclear modes contribute to the reorganization energy, λ, which can then be expressed as the sum of two independent parts, i.e. λ_{in} and λ_{out},

$$\lambda = \lambda_{in} + \lambda_{out} = \lambda_{in} + \frac{e^2}{4\pi\varepsilon_0}\left(\frac{1}{2R_D} + \frac{1}{2R_A} - \frac{1}{R_{DA}}\right)\left(\frac{1}{n^2} - \frac{1}{\varepsilon_S}\right) \qquad 3.22$$

λ_{in} represents the reorganization of the inner (reactant) nuclear modes, i.e. changes in bond lengths and bond angles that D^*–A undergoes when moving from the reactant to the product nuclear configuration. λ_{out} involves the reorganization of the outer (solvent) nuclear modes which accompany ET and accommodate changes in polarization around the donor/acceptor couple. In most cases, in polar solvents, λ_{out} is the dominant term in the expression of λ for electron transfer reactions. By approximating the donor and acceptor to spheres, λ_{out} can be estimated from the refractive index n and the dielectric constant of the solvent ε_S.[168] This expression for λ_{out} implies that λ_{out} will be particularly large in polar solvents and when R_{DA} is large.

3.3.2 ELECTRON TRANSFER IN DONOR–BRIDGE–ACCEPTOR SYSTEMS

In D–B–A systems, due to the large distance separating the donor/acceptor couple, electron transfer occurs preferentially through–bond, mediated by the bridge. Two alternative mechanisms for through–bond ET are generally proposed: namely the coherent tunneling or incoherent hopping mechanism (Figure 3.4). In coherent tunneling, electronic communication between the donor and acceptor is sustained by interaction of the initial and final states of the system with high energy virtual states of the bridges. Such electronic communication is often described by the superexchange model (*vide infra*) which assumes donor and acceptor states energetically well separated from the bridge states (i.e. large injection energy barrier ΔE).[169-171] Thus, no bridge state is ever populated during electron or hole transfer. In contrast, the incoherent hopping mechanism implies real intermediate bridge states in the electron or hole transport between the donor and acceptor. Thus, it is often observed for nearly resonant donor/acceptor and bridge states (i.e. low ΔE) or downhill energy gradient within the D–B–A system. Since bridge states are temporarily populated during transport, the incoherent mechanism is often referred to as thermally activated hopping.[172-173] In many D–B–A systems, both mechanisms are expected to contribute to the transfer and this has been observed experimentally by several groups.[83, 90, 174]

For the coherent electron tunneling mechanism, mixing of the donor/acceptor states with virtual bridge states is described by the so–called superexchange model.[170-171, 175] For a bridge consisting of n identical subunits $\mathbf{B_n}$ as in Figure 3.4, this model relates the total donor/acceptor electronic coupling V_{DA} to localized electronic interactions between neighboring individual subunits according to equation 3.23,

$$V_{DA} = \frac{V_{DB}V_{BA}}{\Delta E}\left(\frac{V_{BB}}{\Delta E}\right)^{n-1} \qquad 3.23$$

where V_{DB} and V_{BA} are the electronic coupling of the bridge to the donor and acceptor, respectively. V_{BB} represents the interaction between adjacent bridge subunits and ΔE is the injection energy barrier between the relevant donor/acceptor and bridge localized states (Figure 3.4). The reciprocal dependence of the total electronic coupling on the injection barrier was experimentally demonstrated by Albinsson and co–workers by treating the bridge in a series of OPE–based bridge D–B–A systems as a single chromophore.[29] Moreover, if the electronic coupling between bridge subunits is small compared to the injection energy barrier (i.e. $V_{BB} << \Delta E$) and the donor–acceptor distance is directly proportional to the length of one subunit R_0 (i.e. $R_{DA} = nR_0$), an exponential distance dependence of V_{DA} and the rate k_{ET} is obtained,

$$k_{ET} = k_0 \exp(-\beta R_{DA}) \qquad 3.24$$

where k_0 is the limiting rate at donor–acceptor contact. β is the so–called attenuation factor, that is, within this approximation, given by equation 3.25.

$$\beta = \frac{2}{R_0} \ln \left| \frac{\Delta E}{V_{BB}} \right| \qquad 3.25$$

Equation 3.25 implies that β is a parameter specific to the donor–bridge–acceptor ensemble involved, as it has been shown experimentally by several groups.[29, 81-82] Typically, β–values are larger for D–B–A systems connected by non–conjugated bridges than by π–conjugated bridges.[79, 176] In the search for efficient long–range electron transfer, β–values have been extensively used as quality factor. In particular, empirical β–values have been used to report on the distance dependence of ET occurring via the incoherent hopping mechanism, although this mechanism is not expected to give rise to an exponential distance dependence of the transfer rates.

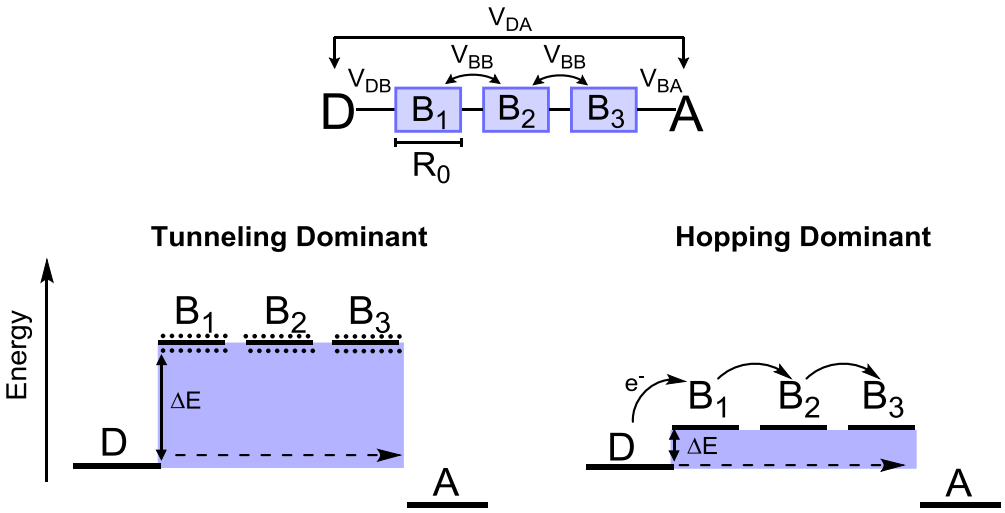

Figure 3.4 Schematic comparison of the tunneling (left) and hopping (right) mechanisms in a D–B–A system here shown for electron transfer. The McConnell superexchange model for electron tunneling through molecular structures is illustrated in the top drawing. For the tunneling model, the bridge virtual states are represented as dashed lines; while in the hopping model, the local bridge states are drawn as solid lines. ΔE_{DB} represents the tunneling energy barrier for electron injection onto the bridge. Note that R_{DA} is the donor–acceptor distance measured along the wire and not through space. Adapted from Ref. 79 with permission from The Royal Society of Chemistry.

3.4 ENERGY TRANSFER THEORY

The energy transfer processes in this work are intramolecular non–radiative energy transfer between identical chromophores and are referred to as excitation energy transfer (EET) or excitation energy migration. They can be described by the following reaction,

$$A_1{-}A_2 + hc/\lambda \rightarrow A_1^*{-}A_2 \xrightarrow{k_{EET}} A_1{-}A_2^* \qquad 3.26$$

where A_1^* and A_2^* are localized isoenergetic electronic excited states. Excitation migration does not affect the fluorescence lifetime of A_1–A_2 but may yield to a depolarization of its fluorescence.

In the following discussion, for more clarity, I use the notations D and A to designate the energy donor and acceptor, respectively. Note that reaction 3.26 implies weakly coupled multichromophoric systems. The excitation energy transfer rates, k_{EET}, can thus be predicted by the appropriate Fermi Golden Rule,

$$k_{EET} = (2\pi/\hbar) \left| \int \Psi_{D\text{-}A^*} \, \hat{H}' \, \Psi_{D^*\text{-}A} \, d\tau \right|^2 \text{FWCD} \qquad 3.27$$

where $\Psi_{D^*\text{-}A}$ and $\Psi_{D\text{-}A^*}$ are the wave functions of the initial D^*–A and D–A^* final states, respectively. $\hat{H}'$ denotes the electronic coupling operator between the two excited states D^* and A^*. The FWCD–term consists of the sum of the vibrational overlap integrals at thermal equilibrium. Since electronic coupling may occur through–space (i.e. coulombic) or through–bond (i.e. electron exchange), $\hat{H}'$ can be divided into two parts, coulombic $\hat{H}_c'$ and electron exchange $\hat{H}_e'$. Depending on the donor–acceptor system (e.g. donor–acceptor distance, relative orientation of the donor and acceptor or spin of the involved states), through–space or through–bond electronic coupling may dominate. This leads to two alternative mechanisms by which EET may occur: a coulombic mechanism commonly known as FRET (Förster Resonance Energy Transfer) and an electron exchange mechanism called Dexter energy transfer (Figure 3.5).

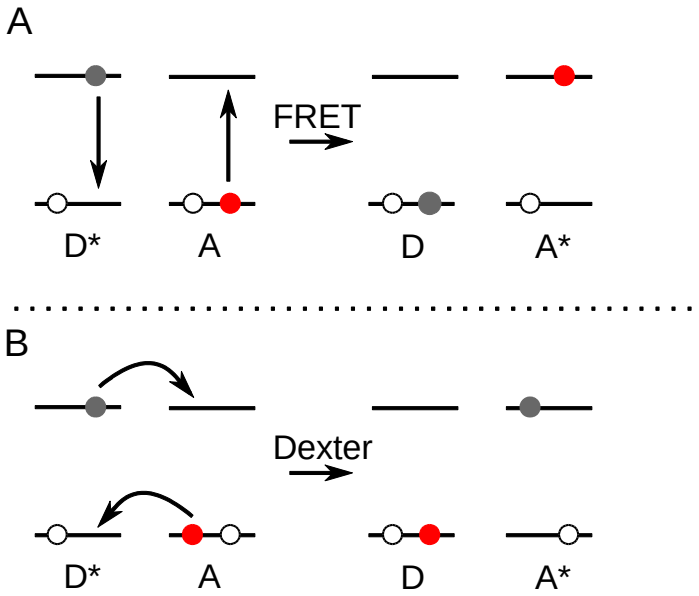

Figure 3.5 Schematic comparison of (A) FRET and (B) Dexter energy transfer mechanisms. Adapted from reference 153.

Förster Resonance Energy Transfer

In FRET, the coulombic interaction arises from the fact that a chromophore in the excited state generates an electric field. Likewise light, this electric field can perturb the charge distribution of neighboring chromophores. Thus, the interaction between the donor and acceptor in FRET is regarded as the interaction between two transition dipoles, i.e. one on the donor and one on the acceptor. Hence, it follows the same selection rules as the transition dipole moments associated to the transitions $D^* \rightarrow D$ and $A \rightarrow A^*$, e.g. resonance condition, no change in spin (*vide supra*). In this work, the energy transfer reactions involve identical chromophores (reaction 3.26); hence the resonance condition is always fulfilled. Since the same selection rules as for absorption and emission transitions apply, it also means that faster FRET rates will be obtained in donor–acceptor couples that have strong radiative transitions (i.e. large transition dipole moments). This is clearly seen in the expression of the FRET energy transfer rate k_{EET}^F predicted by Förster theory that includes the fluorescence quantum yield Φ_D, the lifetime τ_D of the donor and an overlap integral J_F between the emission spectrum of the donor $I_D(\bar{\nu})$ and the molar absorptivity spectrum of the acceptor $\varepsilon_A(\bar{\nu})$,[177-178]

$$k_{EET}^F = 8.8 \times 10^{-25} \frac{\kappa^2 \Phi_D}{n^4 R_{DA}^6 \tau_D} J_F \qquad 3.28$$

where

$$J_F = \frac{\int \left(\frac{I_D(\bar{\nu})\, \varepsilon_A(\bar{\nu})}{\bar{\nu}^4} \right) d\bar{\nu}}{\int I_D(\bar{\nu})\, d\bar{\nu}} \qquad 3.29$$

Note that in J_F, normalization is done on the emission spectrum of the donor. This means that J_F is independent of the oscillator strength of the donor. Equation 3.29 also shows how directional energy transfer may be achieved in a multichromophoric system. Energy transfer will be directed towards the acceptor chromophore whose absorptivity spectrum overlaps the most with the donor emission spectrum.[179] Hence, faster EET will be obtained in systems where the chromophores are spatially arranged according to their transition energy gaps, i.e. in a downhill energy gradient.

In equation 3.28, another important parameter is κ^2 which reflects the directional nature of the dipole–dipole interaction. Its value varies between zero for perpendicular transition dipole moments and four for collinear transition dipole moments. *n* is the solvent refractive index and finally R_{DA} is the donor–acceptor distance.

Dexter energy transfer

As mentioned above, Dexter energy transfer is a through–bond energy transfer mechanism, which can be described as a double–electron transfer process (Figure 3.5).[180] In contrast to FRET, it requires overlap between the donor and acceptor orbitals.

The rate for Dexter energy transfer, k_{EET}^{D}, can be expressed according to the Fermi Golden rule by,

$$k_{EET}^{D} = (2\pi/\hbar) \left| \int \Psi_{D\text{-}A^*} \; \hat{H}_e' \, \Psi_{D^*\text{-}A} \, d\tau \right|^2 J_D \qquad 3.30$$

where

$$\left| \int \Psi_{D\text{-}A^*} \; \hat{H}_e' \, \Psi_{D^*\text{-}A} \, d\tau \right|^2 J_D = V_{DA}^{EET}(0) \exp\left(-\frac{\beta^{EET}}{2} (R_{DA} - r_0) \right) \qquad 3.31$$

and J_D is the Dexter overlap integral between the emission spectrum of the donor and the molar absorptivity spectrum of the acceptor:

$$J_D = \frac{\int I_D(\bar{\nu}) \, \varepsilon_A(\bar{\nu}) \, d\bar{\nu}}{\int I_D(\bar{\nu}) \, d\bar{\nu} \int \varepsilon_A(\bar{\nu}) \, d\bar{\nu}} \qquad 3.32$$

In equation 3.31, V_{DA}^{EET} denotes the donor–acceptor electronic coupling for exchange energy transfer, $V_{DA}^{EET}(0)$ is the donor–acceptor electronic coupling taken at the contact distance r_0 and β^{EET} is the attenuation factor for exchange energy transfer. Likewise the electronic coupling for electron transfer, V_{DA}^{EET} decays exponentially with the donor–acceptor distance R_{DA} and so does the energy transfer rate k_{EET}^{D}. Hence, Dexter energy transfer dominates mostly at short distances, provided that the donor and acceptor molecular orbitals overlap. In contrast, FRET whose rate decays with the sixth power of R_{DA} (equation 3.28) can occur with an appreciable rate for much longer donor–acceptor separation distances.

Another important difference between Dexter energy transfer and FRET is highlighted by equation 3.32. In the expression of J_D, the normalization is not only made on the emission spectrum of the donor but also on the absorptivity spectrum of the acceptor. This implies that the Dexter energy transfer rate is in contrast to FRET, independent of the oscillator strengths of the donor and acceptor. This means that triplet–triplet energy transfer via Dexter mechanism is not forbidden as it is in FRET.

4 PUT THE THEORY TO WORK: IN PRACTICE

Since Ciamician's time and his experiments on the balconies of his Bologna institute, our experimental labs have evolved. We are not anymore limited to outdoor experiments with the Sun as the only convenient light source for investigating photoinduced energy and electron transfer processes. More reliable and convenient light sources have been developed along with detection systems. Spectroscopy designates all experimental techniques based on light–matter interactions described in the previous chapter 3.[151] *In this work, all experimental techniques used are spectroscopic techniques. The difference between these techniques lies in the type of light (continuous or pulsed illumination) and the mode of detection.*

4.1 Steady–state Absorption and Emission Spectroscopies

Steady–state absorption and emission spectroscopies are two techniques in which the sample is continuously illuminated during the measurements. In this way, the excited state population remains constant over the entire measurement.

4.1.1 Steady–state absorption

According to the first law of photochemistry (the Grotthus–Draper law)[181], "*only radiation absorbed in a system can produce a chemical change.*" Thus, information on the response of studied molecules to light comes first from their absorption spectra. Absorption of light by molecules is simply measured by letting light pass through a sample and monitoring the intensity difference between the incident I_0 and transmitted light I at each wavelength (Figure 4.1). This produces an absorption spectrum often given as the absorbance as a function of wavelength, with absorption bands at wavelengths determined by the energies of the electronic states involved in the transition and intensities governed by the magnitude of the transition dipole moment, as discussed in chapter 3.

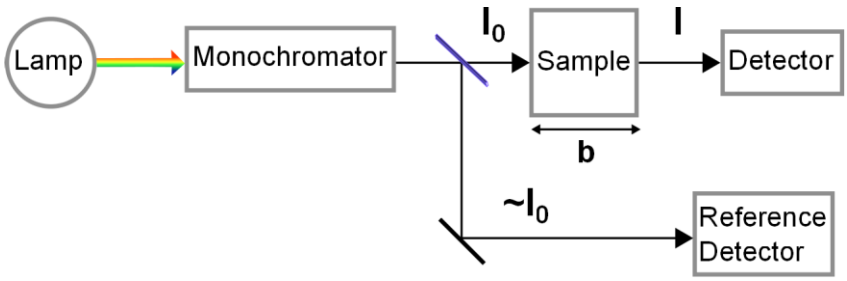

Figure 4.1 Schematic block diagram of a spectrophotometer.

The absorbance of a sample, A, is also related to the number of molecules present in the light path, *b*, by the Beer–Lambert law (equation 4.1).

$$A(\lambda) = -\log_{10}\frac{I}{I_0} = \varepsilon(\lambda)\,cb \qquad 4.1$$

In equation 4.1 $\varepsilon(\lambda)$ is the molar absorptivity of the molecule ($M^{-1}cm^{-1}$), *c* the concentration. The molar absorptivity relates to the probability of transition between two electronic states, $|\vec{\mu}_{fi}|^2$, defined in chapter 3, according to equation 4.2.

$$\int \varepsilon(\bar{\nu})d\bar{\nu} \propto |\vec{\mu}_{fi}|^2 \qquad 4.2$$

In this regard, the molar absorptivity is the practical measure of the strength of electronic transitions between the ground state and any higher electronic excited states. Hence, the molar absorptivity is often used as a quantitative descriptor of the light harvesting power of a chromophore.

Steady–state absorption can provide information on intra–and intermolecular interactions. The Beer–Lambert law is an additive law, which in presence of several distinct species can be expressed as

$$A(\lambda) = -\log_{10}\frac{I}{I_0} = b\sum_i \varepsilon_i(\lambda)\,c_i \qquad 4.3$$

The observed absorption spectrum is the sum of the individual absorption spectra of the species contained in the sample. This aspect is particularly useful, as it enables the use of absorption to follow reactions between chromophores such as the formation of dimers of conjugated porphyrin oligomers described in chapter 5. In supramolecular systems such as donor–bridge–acceptor systems, it provides information on the ground–state electronic interaction between the different components. For D–B–A systems, the absorption spectrum should ideally be a linear combination of the individual spectra (D, B, A) for the donor, bridge, acceptor molecular identity and functions to be retained.

4.1.2 Steady–state emission

In steady–state emission, this is the reverse process to absorption which is measured; that is the emission of a photon induced by the transition of a molecule from an electronic excited state to its ground state. This means that as in absorption, the emission wavelength is related to the energies of the two electronic states involved in the transition. However, although absorption and emission may arise from transitions between the same electronic states (e.g. S_0–S_1), emission of a fluorophore is typically observed at longer wavelengths than absorption. Such difference in wavelength between the maxima of the absorption and emission bands is called Stokes shift.[182] This energy loss is often due to higher vibrational levels of S_0 being populated upon emission, but may also result from solvent effects, formation of excited–state complexes. The

fluorescence rate constant, k_f, is related to the probability of the transition to occur or molar absorptivity via the Strickler–Berg relation given in equation 4.4.[183]

$$k_f = 2.88 \times 10^{-9} \times \bar{\nu}^2 \times \int \varepsilon(\bar{\nu})\, d\bar{\nu} \qquad 4.4$$

In the above equation, $\bar{\nu}$ is the transition wave number.

In practice, steady–state emission is measured by exciting the sample with an intense light source and collecting the emitted photons using a photomultiplier tube placed in a direction perpendicular to light excitation (Figure 4.2).

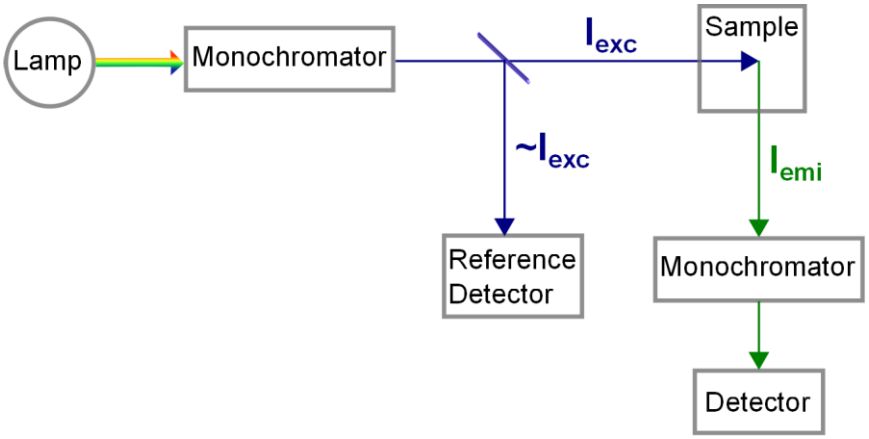

Figure 4.2 Schematic block diagram of a spectrofluorometer.

Setting the excitation wavelength and scanning over the emission wavelengths produces an emission spectrum, i.e. emission intensity as a function of wavelength. The emission intensity represents the number of photons emitted which depends on the number of molecules in the excited states and the radiative rate constant k_f. This means that any non–radiative pathway, such as electron and energy transfer, depopulating the excited state will lower the emission intensity. In this regard, the steady–state integrated emission of a donor–acceptor system provides first evidence of quenching processes in the excited state when compared to a donor reference. From emission spectra, the fluorescence quantum yield of a sample $\Phi_{f,S}$ defined in chapter 3 can also be determined. This requires the use of a reference whose $\Phi_{f,R}$ is known and the measure of its emission spectrum. The fluorescence quantum yield of the sample is then given by,

$$\Phi_{f,S} = \Phi_{f,R} \frac{A_R}{A_S} \frac{I_{f,S}}{I_{f,R}} \left(\frac{n_S}{n_R}\right)^2 \qquad 4.5$$

where $I_{f,S}$ and $I_{f,R}$ are the integrated emission intensities of the sample and the reference, respectively. A_R and A_S are the absorbance of the sample and the reference at the excitation wavelengths, respectively, and n_S and n_R are the refractive indices of the respective solvents. This equation is valid on the assumption that the sample and reference absorbances are low enough to avoid inner–filter effects (e.g. reabsorption of emitted photons by ground–state molecules before reaching the detector).[184]

Another type of measurement is steady–state excitation spectrum. Instead of scanning over the emission wavelengths, one sets the emission wavelength and scans over the excitation wavelengths, i.e. the absorption bands of the sample. This produces an excitation spectrum that reflects the dependence of the emission intensity on the excitation wavelength. In general, most fluorophores have their emission spectra that are independent of the excitation wavelength (Kasha's rule).[157] Consequently, their excitation spectra resemble their absorption spectra. However, in complex fluorophore mixtures (i.e. in presence of several emitting electronic states), steady–state excitation may generate an excitation spectrum that reproduces partially the absorption spectrum of the sample. If the fluorophores have slightly different emission wavelengths, the excitation spectrum will resemble the absorption spectrum of one or another emitting species present in the sample depending on the set emission wavelength. In this regard, steady–state excitation can provide information on the emitting states.

Steady–state methods, absorption and emission, provide both qualitative and quantitative information on the ground state and excited states of molecules, respectively. However they do not permit access to the time dimension of the absorption and emission processes, neither to determine the nature of quenching processes (e.g. electron and/or energy transfer). This requires more sophisticated techniques such as the ones described in the next section.

4.2 TIME–RESOLVED SPECTROSCOPIES

4.2.1 LASERS

An important constraint in the study of excited–state processes is the intrinsic transient character of the excited states and their short lifetimes (sub–nanoseconds to nanoseconds). Thus, to resolve these excited–state processes, a primary requirement is a light source able to excite the sample on a time scale that is faster than its lifetime. Lasers fulfill this requirement, more particularly ultrafast lasers. Developed in the 1980s by Moulton at Lincoln Laboratory, titanium–doped sapphire (Ti: Al_2O_3) lasers produce ultra–short laser pulses with sub–picosecond FWHM ($< 10^{-12}$ s).[185] A second requirement that is equally important to the first one is being able to monitor ultrafast excited–states processes that follow photo–excitation, i.e. electron and energy transfer reactions in this work. By "monitor" one means to time–resolve these processes, i.e. determine their kinetics. This can be done using the pump–probe technique. In particular, this technique was used demonstrated by Prof Ahmed H. Zewail as a means to follow intermediates states of chemical reactions for which he received the Nobel Prize in Chemistry 1999.[186] In this work, we were interested in monitoring electron and energy transfer processes occurring from electronically excited states on the time scale of few picoseconds to hundreds of picoseconds. Thus, we also used a pump–probe technique, namely transient absorption which enables recording of the change in the sample's absorbance induced by light as function of time.

4.2.2 TRANSIENT ABSORPTION

Figure 4.3 shows the experimental set up of pump–probe transient absorption used in this work. This technique is based on the use of two laser pulses, namely the pump and probe pulses. The pump pulse photo–excites the sample, i.e. initiates excited–state reactions. The probe pulse is used, as its name implies, to probe the changes that the reacting molecules undergo following photo–excitation, and hence is delayed in time relative to the pump pulse. In order to achieve high time–resolution ($< 10^{-12}$ s^{-1}), both pump and probe pulses are generated from the same ultrashort laser pulse (FWHM ~ 100 fs). Such ultrashort laser pulse is originally provided by a femtosecond titatinium sapphire laser, also called seed laser. Femtosecond titanium sapphire laser produces femtosecond laser pulses centered at 800 nm at a repetition rate of 80 MHz with ~ 10 nJ pulse energy. However, such pulse energy is generally not enough to achieve sufficiently high concentration of molecules in the electronically excited states that changes in absorption will be detectable. Thus, the femtosecond pulses are often further amplified. Typically, this is realized by chirped pulse amplification (CPA) in a regenerative amplifier. In short, after entering the amplifier, the femtosecond pulses are first stretched in time (typically up to 100 ps) to reduce their peak power in order to avoid damages of the gain medium during amplification. The stretched pulses can then be amplified and enter the gain medium (a Ti:sapphire crystal) that is continuously fed by an additional pump laser. After amplification, the high–intensity stretched pulses are compressed back to their original pulse width. This produces a final fundamental laser pulse train with duration of ca. 100 fs with ca. 1 mJ pulse energy at a repetition rate of 1 kHz, which subsequently splits into pump and probe using a beam splitter. For more details on the generation of ultra–short laser pulses and their amplification, please see e.g. "Laser Fundamentals" by William T. Silfvast.[187]

Taking now a journey in Figure 4.3 on the different optical paths followed by the pump and probe beam. On the pump beam path, one encounters an optical parametric amplifier (OPA). This system, based on non–linear optical processes induced by high–intensity laser pulses, enables tuning of the excitation wavelength of the pump beam (i.e. 800 nm) to a wavelength where the studied sample absorbs, typically in the visible region. This gives access to a wider range of photo–induced reactions that can be studied. Thereafter, a chopper is used to block every second pulse of the pump beam. The pump pulses are then time–delayed relative to the probe pulses by increasing their path length using a computer–controlled optical delay line (range 0–1.6 ns or 0–10 ns). Optical delaying enables here to time–delay the pump and probe pulses with high accuracy, and hence record changes in absorption in steps as small as 100 fs. Note that light travels 0.03 mm in 100 fs. Finally, the pump beam is focused on the sample contained in a 1 mm thick cuvette. Following now the probe beam path, white light is generated by focusing the monochromatic 800 nm probe beam on a 3 mm moving CaF_2 plate. This produces a white light continuum in the region 400–800 nm. Subsequently the probe beam is divided into a reference and probe beam before reaching the sample.

At the sample, the probe beam is superimposed spatially with the pump beam while the reference beam simply passes through the sample unaffected by the pump beam. Both probe and reference beams are then directed to two optical fibers (OF) linked to a CCD camera, which records their intensities as a function of wavelength for each pump–probe time delay. Finally, to avoid any polarization effects on the measured transient absorption that may arise from the use of linearly polarized pump and probe laser pulses, the polarization of the pump pulse is set to 54.7º (magic angle) with respect to the polarization of the probe pulse using a polarizer and a Berek polarization compensator placed before the sample (not represented in Figure 4.3). Also not represented in Figure 4.3 is the possibility to combine femtosecond pumping with picosecond probing using a pulsed laser diode (FWHM ~ 100 ps) as probe light. The time delay between the femtosecond pump pulse and the picosecond probe pulse is then controlled electronically and this is the probe pulse from the laser diode that is electronically delayed relative to the pump pulse. As we will see in chapter 5, this set–up allows for probing long–lived species (> 10 ns).

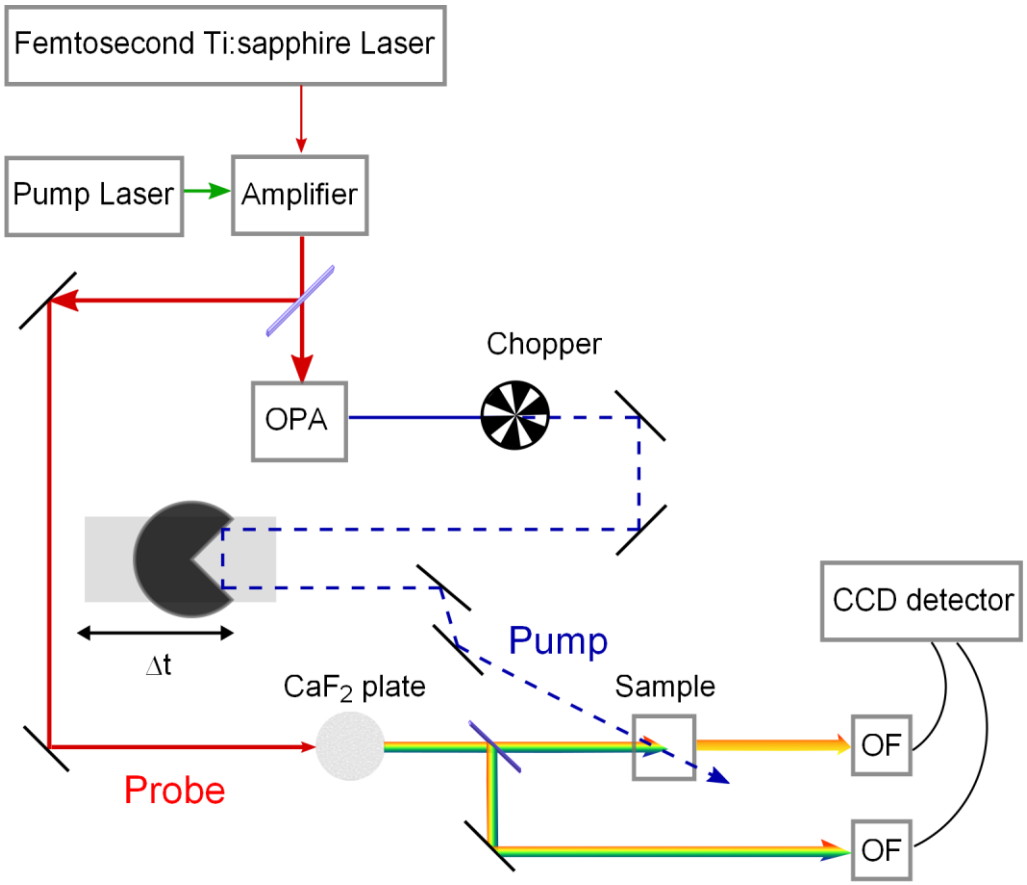

Figure 4.3 Schematic block diagram of the femtosecond transient absorption set up used in this work. The different components and their respective purpose are explained in the text.

From the recorded intensities in presence and absence of pump beam, the differential absorption ΔA between the excited A_{ES} and ground–state A_{GS} absorptions can be determined using the Beer–Lambert law as in equation 4.6.

$$\Delta A(\lambda) = A_{ES}(\lambda) - A_{GS}(\lambda) = \left(-\log_{10} \frac{I(\lambda)^{\frac{p}{on}}}{I(\lambda)_0^{\frac{p}{on}}} \right) - \log_{10} \frac{I(\lambda)^{\frac{p}{off}}}{I(\lambda)_0^{\frac{p}{off}}}$$

$$\Delta A(\lambda) = A_{ES}(\lambda) - A_{GS}(\lambda) = \log_{10} \frac{I(\lambda)^{p/off}}{I(\lambda)_0^{p/off}} \frac{I(\lambda)_0^{p/on}}{I(\lambda)^{p/on}} = \log_{10} \frac{I(\lambda)^{p/off}}{I(\lambda)^{p/on}} \qquad 4.6$$

The intensities I and I_0 are the intensities of the probe and reference beams, respectively. The labels "p/on" and "p/off" designate intensities measured in presence and absence of pump beam, respectively. For a perfectly stable laser, in equation 4.6, measuring the intensities of the reference beams, i.e. $I_0^{p/on}$ and $I_0^{p/off}$ is not required as they cancel out. In reality, they must be used for correction of intensity fluctuations of the laser. Finally, compilation of the transient absorption spectra recorded at different pump–probe time delays may be viewed as a movie of the "life time" of electronically excited states.

Interpretation of the observed ΔA

As ΔA is a differential absorption, both negative and positive peaks can be observed in a transient absorption spectrum. According to equation 4.6, a simple and preliminary interpretation of positive and negative ΔA is the following: positive peaks are observed in regions where excited–state absorption dominates over ground–state absorption, while negative ΔA peaks arise from dominant ground–state absorption. This is the simplest case and the picture may be a bit more complex since other phenomena may also give rise to the observed ΔA. For example, another phenomenon that contributes negatively to the observed ΔA is stimulated emission. Molecules in the excited state relax to the ground state by emission of a photon, similarly as for spontaneous emission, but with the difference that stimulated emission is triggered by the probe beam. Positive contribution to ΔA may also be due to absorption of radical species formed from the excited state. This means that if absorption of these radical species does not overlap with the ones of the excited state or ground state, their formation can be clearly demonstrated by transient absorption and their kinetics monitored. In this regard, transient absorption is a key experiment in photoinduced electron transfer studies providing direct evidence of formed radical species, such as charge–separated states $D^{\bullet+}$–$A^{\bullet-}$ in D–A systems. Hence, it enables to relate lower fluorescence intensities of donor–acceptor systems in steady–state emission to quenching by electron transfer.
Since negative and positive ΔA can originate from different phenomena, it can be difficult to interpret a transient absorption spectrum without any prior knowledge of the studied system. In parallel to transient absorption, spectro–electrochemical measurements are often performed in order to identify the wavelength range in which the radical species are expected to absorb and how strong their molar absorption is.

Quantum mechanical calculations may also be performed to simulate the absorption spectra of the excited state and radical species.

Transient absorption contains more than only qualitative information. From the accumulated transient absorption spectra, transient absorption time profiles at a chosen wavelength (i.e. ΔA_λ as a function of time) can be extracted. The transient absorption time profiles describe how fast a species forms or vanishes, provided that at the chosen wavelength only this species contributes to the transient signal.

4.2.3 TIME–RESOLVED EMISSION

Time–resolved emission spectroscopy is another technique that is based on pulsed laser sources of excitation, fast detection and electronics. This technique enables measurement of fluorescence lifetimes. As in most lifetime measurement techniques, the lifetime is determined by monitoring the number of excited states present over time. In time–resolved emission spectroscopy, it is the emission intensity or number of emitted photons from the excited state which is recorded as function of time. Indeed the number of emitted photons from a sample at any time is directly proportional to the number of excited states present. As discussed in chapter 3, the number of excited states is expected to follow first–order decay kinetics, and so is its emission intensity,

$$\frac{dI(t)}{dt} = -\sum_j k_j\, I(t) \qquad 4.7$$

where $\sum_j k_j$ is the sum over all the rate constants that depopulate the excited state. This equation solve to a mono–exponential expression for one emitting state: $I(t) = I_0 \exp(-t/\tau)$. Thus, the fluorescence decay of a sample ($I(t)$ vs. t) is often plotted on a semi–logarithmic scale and describes a straight line with a slope of $-\tau$. Representation of fluorescence decays on a semi–logarithmic scale enables also to identify the presence of several emitting states in a sample. In that case, the fluorescence decay does not describe a straight line anymore and instead, a multi-exponential expression reproduces the fluorescence decay,

$$I(t) = I_0 \sum_i^n \alpha_i \exp(-t/\tau_i) \qquad 4.8$$

Here, I_0 is the intensity at time zero, α_i the amplitude contribution of the excited state *i*, τ_i its corresponding lifetime and *n* the number of distinct excited states.

Single photon counting is one of most used methods to record fluorescence decays. In this work, two techniques based on single photon counting have been used to measure fluorescence lifetimes: Time Correlated Single Photon Counting (TCSPC) and a streak camera system. Both techniques used the same source of excitation and differ only in the system of photon detection and the mode of data collection. These differences and

their implications in term of time and wavelength resolutions are explained in the paragraphs below. In this work, the fluorescence lifetimes of the studied systems range from tens of picoseconds to few nanoseconds. As in pump–probe transient absorption, this put some requirements on the excitation source and electronics. The pulses of laser light used to excite the sample should be shorter or of similar time duration as the lifetime to be resolved. This requires the use of ultrafast lasers. Here, a picosecond titanium:sapphire laser was used as excitation source that generates short light pulses of 1–2 ps full–width at half maximum (FWHM) at a repetition rate of 82 MHz. Its output wavelength was tunable between 720 nm to 1000 nm. Both the repetition rate and the excitation wavelength could be further modified. By letting the laser pulse through a pulse picker, the repetition rate could be reduced. The desired excitation wavelength could be obtained by subsequent frequency doubling or tripling of the initial wavelength in a generator of wavelength harmonics (GWH). Detection of the emitted photons was done using a photomultiplier tube in TCSPC, while in the streak camera set–up, a spectrometer and a CCD camera were combined to detect photons. In both experimental set–ups, as in steady–state emission, photon collection is in a direction perpendicular to light excitation. As for transient absorption, to avoid any polarization effects on the decay, a polarizer set at 54.7º (magic angle) relative to the polarization plane of the excitation light is placed in between the sample and the detector. By polarization effects, one refers to the production of polarized emission which arises from preferential excitation of the molecules having their absorption transition dipole moments in line with the polarization direction of the excitation laser pulse. Such effects are used in fluorescence anisotropy to study rotation and energy migration studies in molecules (*vide infra*).

Time correlated single photon counting

Figure 4.4 shows a schematic of the TCSPC set up used in this work. Here, the time resolution is obtained electronically by recording the time difference, Δt, between the excitation pulse and the detection of a single photon by the photomultiplier tube (PMT). This is done by having the excitation pulse that both excites the sample and triggers a Time to Amplitude Converter (TAC) through a photodiode. The triggering of the TAC constitutes the START signal for time counting. The TAC voltage increases then linearly with time. When the first photon emitted by the sample hits the PMT, the voltage ramping of the TAC stops and the PMT becomes in some way "blind" until the START signal of another cycle of excitation–emission. The acquired voltage is then converted into a time difference Δt by an Analog to Digital Converter (ADC). This Δt is then stored in one of the time channels of a Multi Channel Analyzer (MCA). Such cycle of excitation–emission is repeated many times and every measured Δt is stored in the corresponding channels of the MCA (Figure 4.5). From the information stored in the MCA, a histogram can be build that represents how many times a single photon has been detected at a given Δt. This histogram reproduces the fluorescence intensity decay of the sample. However this measured fluorescence decay is a convolution of the real fluorescence intensity decay of the sample and the Instrument Response Function (IRF)

which represents how the excitation pulse appears to the detector. The shape of the IRF depends on the type of detector and the width of the excitation pulse. For example, the NIR detector (R3809U–50, Hamamatsu) used in TCSPC measurements of Paper II produces an IRF width of ca. 110 ps for laser excitation pulses in the wavelength range 730 – 840 nm. Thus, two sets of data are generally measured in a TCSPC measurement: one is the fluorescence decay of the sample and the other one is the IRF which is measured at the excitation wavelength by directing the laser pulse to the detector using a scattering solution. In that way, the real decay of the sample can be obtained by deconvolution of the measured data with the IRF.

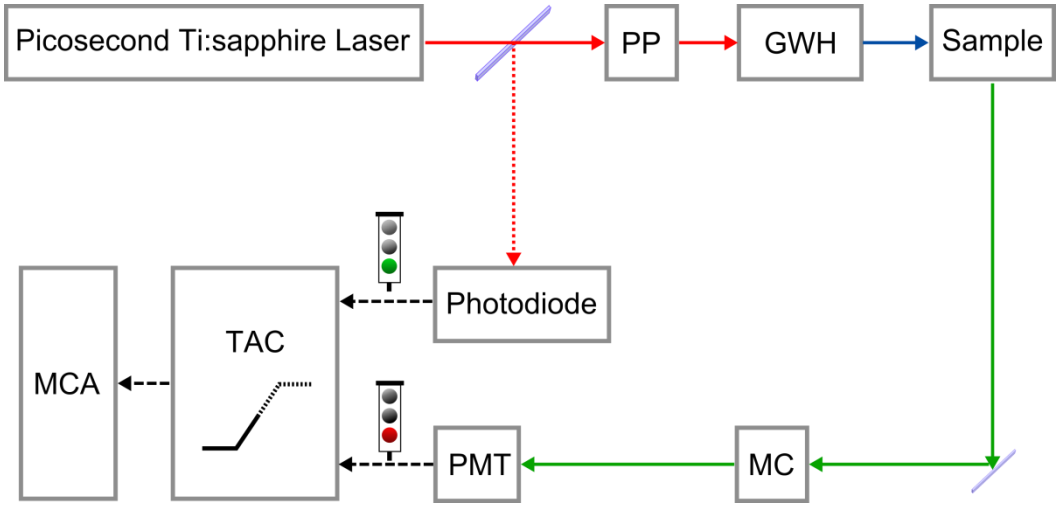

Figure 4.4 Schematic block diagram of the experimental set up for time correlated single photon counting consisting of a Pulse Picker (PP), a Trigger (Tr), a Time–to–Amplitude Converter (TAC), a Multi–Channel Analyzer (MCA), a Monochromator (MC) and a Photomultiplier Tube (PMT).

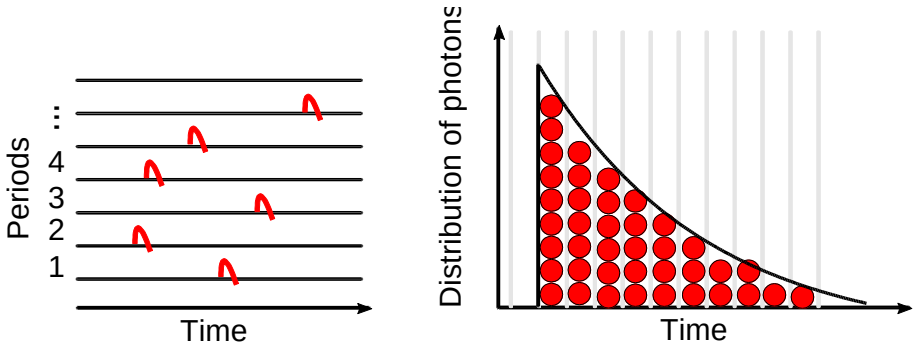

Figure 4.5 Schematic representations showing (left) how the photons are randomly detected after a certain time delay and (right) how the detected photons are stored in the MCA to obtain a histogram representation of the intensity decay.

Typically, for good statistical quality, excitation–emission cycles are repeated until 10 000 photons are counted in the top channel. Another important criterion of this technique is that only one photon is detected per excitation pulse. This requires adjusting the measurement conditions (e.g. intensity of the excitation pulse, emission bandwidth of the monochromator). Indeed at high emission intensity, two photons

originating from the same excitation event may eventually hit the PMT. This will not be a problem if the electronics were fast enough to correlate all photons in time. However, this is not the case. They need to reset after each photon detected which take time. If two photons reach the detector, only the earliest photon will be counted. This is the so–called "pile–up" effect where early photons are preferentially detected. In consequence, the measured fluorescence decay is biased toward early time. To avoid this, the emission intensity at the PMT is reduced so that a photon is counted for no more than about 1 % of the excitation–emission cycles.

Streak camera system

This technique differs from TCSPC by the system of photon detection and presents two strong advantages. The streak camera system combines a spectrometer and a CCD camera. The first advantage of such system is the higher time resolution down to few ps that can be achieved. The second advantage is that in contrast to TCSPC, measurement of the complete emission spectrum as a function of time is possible within a single experiment. This produces 2D–images of the fluorescence emission with time along the vertical axis, the wavelength along the horizontal axis and the intensity along the z–axis. In short, this is done by first dispersing the emitted photons by wavelength using a spectrometer in a line on a photocathode. Thereafter, in the streak tube, the produced photoelectrons are deflected at different angles in the vertical direction depending on their arrival time before hitting a phosphor screen and readout is made by the CCD camera.[188]

4.3 FLUORESCENCE ANISOTROPY SPECTROSCOPY

Much more information can be obtained from the emission of a sample than its simple lifetime. In time–resolved fluorescence spectroscopy, effects of polarization due to the polarized laser excitation source are voluntarily avoided using polarizers at magic angle. In fluorescence anisotropy, polarization of the excitation source is put "at work". By illuminating the sample with polarized light, molecules which have their absorption transition dipole moments oriented in the same direction as the excitation source are preferentially excited (see in chapter 3, the second criteria for light absorption). Emission may then also occur in a preferential direction, i.e. may be polarized. However, this directional information is only conserved if the molecules are not free to rotate or if their rotation is much slower than their lifetime. Indeed any rotation of a molecule during its lifetime will randomize the direction of its emission.
This brings us to the definition of fundamental fluorescence anisotropy, denoted r_0, in absence of any depolarization processes

$$r_0 = \frac{2}{5}\left(\frac{3\cos^2\beta - 1}{2}\right) \qquad 4.9$$

where β is the angle between the absorption and emission transition dipole moments. From equation 4.9, the maximum anisotropy value is 0.4 that corresponds to collinear absorption and emission transition dipole moments (β = 0º). As mentioned earlier for random distributions of linear molecules in solution, a polarized excitation source excites preferentially molecules oriented in the direction of polarization resulting in a polarization of the emission. However, if emission collection is done at 54.7º (i.e. magic angle) relative to the polarization of excitation, equation 4.9 applies at a macroscopic scale gives $r_0 = 0$, hence the choice for the magic angle conditions to eliminate polarization effects in time–resolved emission and transient absorption measurements (*vide supra*). For any fluorophore, lower anisotropy values observed than the one predicted by equation 4.9 will suggest a depolarization of its emission. As mentioned previously, one common cause of depolarization is rotational diffusion of the molecules during their excited–state lifetime. In this regard, fluorescence anisotropy spectroscopy has been used to get structural information such as binding of ligands. Indeed any changes in the size and/or shape and/or surrounding environment of a molecule will affect its rotation, and hence the depolarization of its emission and its fluorescence anisotropy. However other processes may also induce a depolarization of the emission. Depolarization can result from excitation energy migration if accompanied by a change in the direction of the emission transition dipole moments. In this work, it is this application of fluorescence anisotropy that has been of interest.

In practice, both steady–state and time–resolved fluorescence anisotropy may be measured using the respective experimental set–ups described above. Additional polarizers are used to control polarization of the excitation and emission light. In steady–state, excitation anisotropy spectra, i.e. plots of the anisotropy as a function of the excitation wavelength, are usually measured since anisotropy is often independent of the emission wavelength (Kasha's rule).[157] Excitation anisotropy spectra are calculated from the excitation spectra recorded at both vertical (V) and horizontal (H) polarization, using both vertically and horizontally polarized light excitation,

$$r(\lambda) = \frac{I_{VV}(\lambda) - GI_{VH}(\lambda)}{I_{VV}(\lambda) + 2GI_{VH}(\lambda)} \qquad 4.10$$

G is a correction factor that is dependent on the instrument. It corrects for the difference in sensitivity of the detection system to vertical and horizontal polarized light,

$$G = \frac{I_{HV}}{I_{HH}} \qquad 4.11$$

Steady–state anisotropy measurements reveal the average anisotropy value, i.e. the average angular displacement between the absorption and emission transition dipole moments. Comparing the measured steady–state anisotropy value to the predicted value (equation 4.9) gives some hints on the presence/absence of depolarization processes, although quite limited information on their nature. In this regard, time–resolved fluorescence anisotropy provides further information. Using a similar equation to

equation 4.10, the fluorescence anisotropy decay, r(t), can be determined from the fluorescence intensity decays $I_{VV}(t)$ and $I_{VH}(t)$ measured with the emission polarizer parallel or perpendicular to the vertically polarized excitation pulse, respectively. The correction factor G is then given by $\langle I_{HV}(t)/I_{HH}(t)\rangle$ where $I_{HV}(t)$ and $I_{HH}(t)$ are the fluorescence intensity decays with the emission polarizer parallel or perpendicular to the horizontally polarized excitation pulse, respectively. Following pulsed excitation, the fluorescence anisotropy decay is often reproduced by a sum of exponentials

$$r(t) = \sum_j r_{0,j} \exp(-t/\theta_j) \qquad 4.12$$

where $r_{0,j}$ is the fractional amplitude anisotropy at time zero and θ_j are the rotational correlation times. Note that if $\sum_j r_{0,j}$ does not sum up to the r_0 value (equation 4.9); all processes that contribute to emission depolarization have not been time–resolved. Depolarization by excitation energy migration in addition to the natural rotational motion of the fluorophore will also lead to a multi–exponential fluorescence anisotropy decay. These effects can be distinguished by adjusting the experimental conditions in order to prevent occurrence of one of them. Typically this is rotational motion of the fluorophores which is inhibited using high–viscosity solvents (e.g. glycerol) or solvents that form glass at low temperature (e.g. 2–MTHF (T_{glass}~90 K)[189]). Under these conditions, the fluorophores are stationary, and hence only excitation energy migration may contribute to the anisotropy decay.

4.4 DATA ANALYSIS

In order to get meaningful information (rate constants, lifetimes) from transient absorption spectra ($\Delta A(t, \lambda)$) and time–resolved fluorescence decays ($I(t, \lambda)$), one needs to have a model that interconnects real components (e.g. population of excited states, ground–state, charge–separated states,…) via a kinetic scheme so that it is possible to relate the variation of their concentration with time to the measured time–dependent values, $\Delta A(t, \lambda)$ or $I(t, \lambda)$. Simulated data generated according to this model can then be compared to the raw data. If sufficient agreement between the two sets of data is found, reaction rate constants (e.g. ET or EET rates) and lifetimes may be extracted. In this work, data fitting has been done with Matlab for transient absorption and 2D time–resolved fluorescence data.

As mentioned earlier, all reactions investigated in this work are intramolecular, and hence are assumed to be first–order. This means that in general, the overall concentration C (i.e. of all contributing states) at any time *t* is given by solving the master equation,

$$\frac{dC}{dt} = KC \qquad 4.13$$

where K is a matrix containing the relevant combination of rate constants (according to the kinetic model used) and C is a concentration matrix containing the concentration of each individual state. The K matrix off–diagonal elements are the rate constants that populate each individual state while the diagonal elements are the rate constants by which it is depopulated.

4.4.1 INDIVIDUAL FITTING

When fitting fluorescence decays or transient absorption time profiles at wavelengths where the signal arises from a single electronic state *i*, the data are generally fitted individually (i.e. independently). Indeed equation 4.13 simplifies then to a one dimensional equation. The solution of such equation is a mono–exponential function,

$$c_i(t) = c_i(0)\exp(-t/\tau_i) \qquad 4.14$$

where $c_i(0)$ is the population of the state *i* at time zero and τ_i is equal to the inverse of the sum of the rate constants of all depopulating paths (*vide infra*).

Equation 4.14 is general. To fit transient absorption time profiles, this equation needs to be slightly modified. Likewise measured fluorescence intensity decays which are a convolution of the fluorescence intensity decay of the sample and the instrument response function (IRF), measured transient absorption time profiles contain both the real transient absorption time profile and a "certain" temporal response function. This temporal response function arises from the fact that both pump and probe pulses possess a temporal width. In the experimental data, this result in a rise in the absorption time profile of the excited state. This temporal response function is usually approximate by a Gaussian function F(t) with a FWHM equal to $2\sqrt{2\ln 2}\,\sigma$ in the fitting procedure (equation 4.15).

$$F(t) = \frac{1}{\sigma\sqrt{2\pi}}\exp\left(\frac{(t-t_0)^2}{2\sigma^2}\right) \qquad 4.15$$

This leads to the expression for the simulated transient absorption time profiles $\Delta A_{\lambda,fit}(t)$,

$$\Delta A_{\lambda,fit}(t) = \frac{1}{2}\sum \alpha_i \exp\left(\frac{\sigma^2}{2\tau_i^2}\right)\exp\left(\frac{-(t-t_0)}{\tau_i}\right)\operatorname{erfc}\left(\left(\frac{\sigma}{\tau_i} - \frac{(t-t_0)}{\sigma}\right)\frac{1}{\sqrt{2}}\right) \qquad 4.16$$

where erfc designates the complementary error function.

4.4.2 GLOBAL DECAY FITTING

Some molecular systems can display more complex fluorescence intensity decays or transient absorption time profiles or spectra. For example, 2D time–resolved

fluorescence may reveal multi–exponential fluorescence decays that vary across the emission spectrum of a sample. This often results from the presence of more than one emitting states along with several processes correlating their respective populations. In this case, individual fitting is not an option and a global decay fitting may be more appropriate. By global decay fitting, several individual fluorescence decays at different emission wavelengths are fitted simultaneously with the same parameters. Moreover in such data sets, it is often difficult to estimate the relevant number of states that contribute to the signal.

One way to identify the minimum number of emitting states that is needed to describe the entire set of data, is by singular value decomposition (SVD) of the data set. SVD is a general mathematical tool that enables factorization of a rectangular matrix in matrices of orthogonal components. This method is applicable to any two dimensional data sets, e.g 2D transient absorption data. In this work, this method is applied to 2D time–resolved fluorescence data (Paper II), and hence is described in this context. By SVD, if A is a rectangular *n* x *m* matrix containing the fluorescence data where *n* refers to the wavelengths points and *m* the time points, this matrix may be decomposed as,

$$A = U \cdot S \cdot V^T \qquad 4.17$$

U is a *n x n* matrix consisting of the orthogonal emission spectra, V is a *m* x *m* matrix consisting of the orthogonal fluorescence decay and S is a diagonal *n* x *m* matrix containing the positive singular values arranged in descending order. The singular values reflect how much each respective orthogonal component (spectral or temporal) contributes to the signal. While a 2D time–resolved fluorescence image contains few hundred spectra and time profiles, only few components are needed to describe them. To identify the minimum number of components *l* required to describe the data set (i.e. number of emitting states), one may inspect the singular values or the orthogonal components. For example, some of the spectral orthogonal components will lead to actual spectra; however, most of them will just be noise. The minimum number of components *l* is then given by the number of orthogonal components that lead to actual spectra. Only these components can therefore be retained in the analysis resulting in a data matrix A expressed as,

$$A = U_{red} \cdot V_{red} \qquad 4.18$$

where U_{red} and V_{red} are the reduced *n* x *l* and *l* x *m* matrices, that only contain the *l* relevant orthogonal emission spectra and corresponding fluorescence decay, respectively. The next step is then to construct a suitable kinetic scheme through which populations of these *l* emitting states are related. Note that in other cases, populations may be thermodynamically related and instead a thermodynamic scheme is constructed (e.g. see the SVD analysis performed on absorbance data to determine enthalpy and entropy changes associated to the formation of porphyrin aggregates in Paper III). Here, according to the kinetic scheme, it should then be possible to relate their respective

variation of population with time to the measured variation of the emission spectra with time by optimizing of the reaction rate constants. U_{red} and V_{red} should be related through matrix rotation to the true spectral and time–dependent concentration matrices, T and C,

$$U_{red} = T \cdot R^{-1} \text{ and } V_{red} = R \cdot C \qquad 4.19$$

where R is a square *l* x *l* rotation matrix. In short, the procedure starts by determining the the C matrix by solving equation 4.13 using an initial guess of the K matrix which contains the relevant combination of rate constants (not known *a priori*) determined according to the kinetic scheme. From the obtained C matrix, the R matrix can be determined according to $R = V_{red} \cdot C^{-1}$ and subsequently, T can be obtained: $T = U_{red} \cdot R$. Repeating this procedure many times enables then to find the time–dependent concentration matrix C through non–linear optimization of the rate constants searching for the minimum of the norm, $\|A–TC\|$. Finally from the optimized rate constants, the lifetime of each emitting state can be determined as well as their individual emission spectra and their respective fluorescence decays.

5 Photoinduced Electron Transfer in Porphyrin Oligomer–Based Donor–Acceptor Systems

The central theme of this chapter is photoinduced electron transfer reactions in donor–acceptor systems, in which butadiyne–linked zinc porphyrin oligomers $\mathbf{P_n}$ *(n = 1–4, 6) act as a photo–active primary donor. After introducing the butadiyne–linked zinc porphyrin oligomers, this chapter describes the original work in Papers I–III. In general, this work aims at creating valuable knowledge to design molecular systems with pre–determined electron transfer properties, i.e. wire–like, controllable charge transport in solution and self–assembled systems. In Paper I, ET processes in triads,* $\mathbf{Fc–P_n–C_{60}}$*, are discussed while Paper II concers ET reactions in simpler dyad systems,* $\mathbf{P_n–C_{60}}$*. In both studies, the electron transfer reactions are initiated by photo–excitation of the porphyrin oligomers, forming the porphyrin excited states* $\mathbf{Fc–{}^1P_n{}^*–C_{60}}$ *and* $\mathbf{{}^1P_n{}^*–C_{60}}$*, respectively. Although both papers involve photoinduced electron transfer, different aspects of the ET process have been investigated.*

In Paper I, the triads $\mathbf{Fc–P_n–C_{60}}$ *are referred to as molecular wires and it is the ability to transport charge over long distances (nanometers) that is of interest (vide supra). In the last decades, much research efforts have been devoted to relate the appearance of a wire–like behavior (i.e. weakly distance dependent charge transport) to the mechanistic nature of the charge transport (i.e. tunneling or hopping). As in the natural photosynthesis (Figure 2.1), it was thought that in synthetic D–B–A systems, charge transport in the incoherent hopping regime will promote wire–like behavior. However, is this always the case and is this a necessary condition for wire–like charge transport? In particular, a recent paper by the group of Wasielewski has recently revived the discussion on the mechanistic requirements for wire–like charge transport in D–B–A systems. In their D–B–A systems, charge transport occurs in the incoherent hopping regime but is surprisingly characterized by a fairly large β–value (β = 0.34 Å^{-1}).*[87] *From this study, one may also ask: is it possible "or even relevant" to establish general mechanistic rules for wire–like charge transport in D–B–A systems? Here, in Paper I, we investigate the charge recombination mechanism in the series of long–range charge–separated states* $\mathbf{Fc^{\bullet+}–P_n–C_{60}^{\bullet-}}$ *(n = 1–4). A previous study by Winters et al.*[93] *revealed similar recombination rates for the dimer and the tetramer with an apparent β–value of 0.003 Å^{-1} at room temperature. However, the distance–dependence information at room temperature was not sufficient to conclude on the nature of the charge recombination mechanism behind such low β–value. As a follow–up study, Paper I investigates the influence of temperature on the recombination process in the more complete series* $\mathbf{Fc^{\bullet+}–P_n–C_{60}^{\bullet-}}$ *with n = 1–4, 6.*

In view of applications in practical devices, Paper II investigates potential "knobs" that optimize electron transfer rates and can be used to regulate the electron transfer in the simpler donor–acceptor dyads $\mathbf{P_n–C_{60}}$ *(n = 4, 6). In particular, we are interested in whether the inherent conformational flexibility of the porphyrin chain can be used to control the charge separation rate in* $\mathbf{P_n–C_{60}}$ *(n = 4, 6). In practice, we demonstrate that the conformational states of the porphyrin chain can be controlled either optically by varying the excitation wavelength or chemically by reversible ligand coordination. In*

that regard, Paper III can be put in relation to Paper II, although it does not investigate ET reaction. Both papers II & III propose means to control the conformational distribution of the porphyrin chain. Paper III investigates the influence that the temperature has on the conformational distribution of the porphyrin chain, ***P*****$_n$**.

5.1 THE SYSTEM STUDIED: BUTADIYNE–LINKED PORPHYRIN OLIGOMERS

The porphyrin oligomers used in this work as building block for model systems to investigate photoinduced electron and energy transfer processes are *meso–meso* butadiyne–linked porphyrin oligomers, $\mathbf{P_n}$ (Figure 5.1). Their sizes range from the monomer, $\mathbf{P_1}$, to the octamer, $\mathbf{P_8}$.

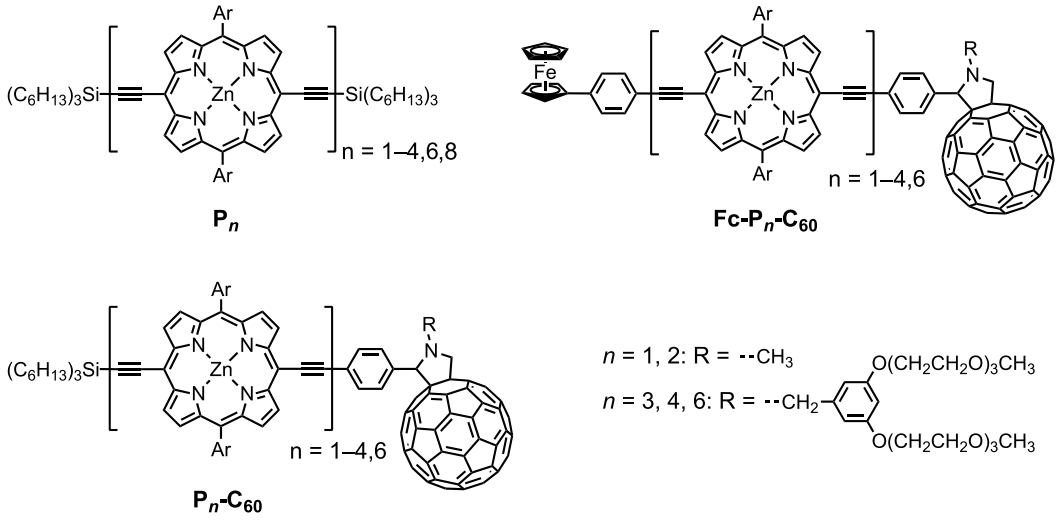

Figure 5.1 Molecular structure of the reference systems $\mathbf{P_n}$, the dyads $\mathbf{P_n–C_{60}}$ and the triads $\mathbf{Fc–P_n–C_{60}}$ studied in this work. The aryl substituents are 3,5–bis(octyloxy)phenyl groups which are used to enhance solubility of the oligomers in organic solvents.

The conjugated porphyrin oligomers, $\mathbf{P_n}$ ($n \geq 2$), possess a rod–like structure but are not free of conformational heterogeneity. At room temperature, owing to the use of alkyne linkers, the energy barrier for rotation of individual porphyrins is very small (ca 0.03 eV for $\mathbf{P_2}$).[190] Consequently, in the longer oligomers ($n \geq 2$), there exists a wide distribution of rotational conformers in the ground state. However, in the excited state, the planar conformers are more stabilized. For example, the perpendicular conformer in $\mathbf{P_2}$ lies at ca. 0.17 eV higher energy than the planar conformer.[190] Influence of this conformational heterogeneity on the photophysical properties of these oligomers has been previously investigated for $\mathbf{P_2}$, both experimentally and via quantum mechanical calculations.[190] It was shown that two spectroscopic species, namely, a planar and a twisted conformer, with distinct electronic transition energies contributed to the absorption spectrum of $\mathbf{P_2}$. In addition, in the excited state, twisted conformers were found to relax almost quantitatively to the more stable planar conformer before emission. Such

conformational effects were used to control photoinduced electron transfer processes in the donor–acceptor fullerene–appended porphyrin dimer, **P_2–C_{60}** (Figure 5.1).[95] Here, in Paper II, we further investigate the conformational aspects of the electron transfer between the porphyrin oligomer and the fullerene in the long **P_n–C_{60}** systems, i.e. the tetramer, **P_4–C_{60}** and the hexamer, **P_6–C_{60}**. The **P_n** systems can also be used as molecular bridge between a donor/acceptor couple by appending a ferrocene group (**Fc**) as electron donor and a fullerene (**C_{60}**) as electron acceptor to the porphyrin oligomer. This results in a series of D–B–A systems, **Fc–P_n–C_{60}** (n = 1–4, 6) with donor–acceptor separation between 24 Å and 92 Å.

5.2 IDENTIFYING THE CHARGE TRANSPORT MECHANISM BEHIND THE "WIRE–LIKE" PROPERTIES OF PORPHYRIN–BRIDGED TRIADS

Determining whether charge tunnels or moves in a step–wise fashion in D–B–A systems is often quite a challenge.[87, 94] Despite their intrinsic experimental difficulties, temperature–dependent studies of electron transfer reactions have often been carried out to gain additional insights in the dominant charge transport.[94, 191-195] In **Fc–P_n–C_{60}** systems, photo–excitation of the porphyrin bridge triggers a sequence of electron transfer steps producing a final, long–range charge–separated state, **$Fc^{\bullet+}$–P_n–$C_{60}^{\bullet-}$** (Figure 5.2). It is this long–range charge–separated state that is of interest and the mechanistic details behind the weakly–distance dependent recombination. As illustrated in Figure 5.2, its formation is limited by several processes that compete with the initial charge separation (CS1) and the charge shift reaction (CSh). Hence, a first query was to ensure that **$Fc^{\bullet+}$–P_n–$C_{60}^{\bullet-}$** is formed for all lengths of the porphyrin oligomer bridge (n = 1–4, 6). Temperature–dependent fluorescence and femtosecond transient absorption were used to follow both charge separation (**Fc–$^1P_n^*$–C_{60}** $\xrightarrow{k_{CS1}}$ **Fc–$P_n^{\cdot+}$–$C_{60}^{\cdot-}$**) and recombination (**$Fc^{\cdot+}$–P_n–$C_{60}^{\cdot-}$** $\xrightarrow{k_{CR2}}$ **Fc–P_n–C_{60}**) processes as a function of temperature. For the formation of the initial charge–separated state, **Fc–$P_n^{\bullet+}$–$C_{60}^{\bullet-}$** , a charge separation scheme similar to the one previously reported in the dyads **P_n–C_{60}** (n = 1–4, 6) was observed.[195] As in the natural photosynthesis, excitation energy may initially localize to some part of the porphyrin bridge far from the electron acceptor and needs to subsequently funnel close to **C_{60}** for charge separation to occur. This implies two possible scenarios for charge separation. If porphyrin units close to the **C_{60}** are initially excited, direct and fast charge separation takes place. Instead, if porphyrins far from the **C_{60}** are excited, migration of the excitation energy along the porphyrin bridge close to **C_{60}** is a prerequisite for charge separation. Formation of the long–range charge–separated state **$Fc^{\bullet+}$–P_n–$C_{60}^{\bullet-}$** was spectroscopically confirmed by following the porphyrin ground–state recovery and the fullerene radical anion transient signals in the regions at 600–800 nm and 1018 nm, respectively. **$Fc^{\bullet+}$–P_n–$C_{60}^{\bullet-}$** only forms in detectable amounts for systems up to the tetramer (n = 1–4) at temperatures above 200 K. Combining femtosecond excitation with picoseconds probing enabled to follow its

recombination by transient absorption. In the long triads (n = 2–4), unusual change in recombination mechanism was observed in the temperature interval 200–300 K. At high temperatures (≥ 280 K), **Fc$^{\bullet+}$–P$_n$–C$_{60}^{\bullet-}$** (n = 1–4) recombines to the ground state via coherent electron tunneling. However, at lower temperatures (< 280 K), the relatively long lifetimes of **Fc$^{\bullet+}$–P$_n$–C$_{60}^{\bullet-}$** (n = 2–4) push surprisingly charge transport into the incoherent hopping regime with the oxidized bridge state **Fc–P$_n^{\bullet+}$–C$_{60}^{\bullet-}$** transiently reformed during recombination.

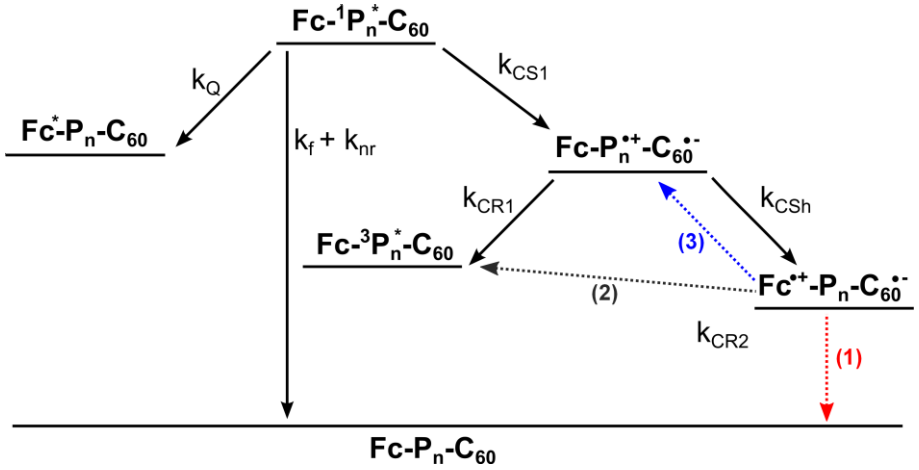

Figure 5.2 Schematic decay scheme of **Fc–^{1}P$_n^*$–C$_{60}$**. The formation of **Fc–P$_n^{\bullet+}$–C$_{60}^{\bullet-}$** (CS1) is limited by the quenching of **Fc–^{1}P$_n^*$–C$_{60}$** by the ferrocene group via energy transfer (Q). Likewise, the formation of **Fc$^{\bullet+}$–P$_n$–C$_{60}^{\bullet-}$** (CSh) is further reduced by recombination of **Fc–P$_n^{\bullet+}$–C$_{60}^{\bullet-}$** to the porphyrin–localized triplet excited state **Fc–^{3}P$_n^*$–C$_{60}$** (CR1). Recombination of **Fc$^{\bullet+}$–P$_n$–C$_{60}^{\bullet-}$** (CR2) may take three different pathways represented in dashed arrows: **(1)** direct recombination to the ground–state via coherent electron tunneling, **(2)** recombination to the porphyrin–localized triplet excited state **Fc–^{3}P$_n^*$–C$_{60}$**, or **(3)** stepwise recombination with first reformation of the oxidized bridge state **Fc–P$_n^{\bullet+}$–C$_{60}^{\bullet-}$** by hole hopping followed then by rapid recombination. Note that the relative positions of the different states are not representing the real relative energies levels and are only indicative.

5.2.1 Direct versus stepwise charge separation in Fc–P$_n$–C$_{60}$

Figure 5.3 compares the ground–state absorption spectra of **Fc–P$_n$–C$_{60}$**, **P$_n$–C$_{60}$** and **P$_n$** for n = 1–4, 6 at room temperature. In general, the visible parts of these spectra are nearly superimposed, despite the additions of the acceptor **C$_{60}$** in **P$_n$–C$_{60}$** and the secondary donor **Fc** in **Fc–P$_n$–C$_{60}$**. This indicates that neither the ferrocene group or the fullerene perturb the electronic ground state of the porphyrin–based bridge.[93, 195] All compounds show the characteristic absorption bands of porphyrins: an intense Soret band ($S_0 \rightarrow S_2$) centered at 450 nm for **Fc–P$_1$–C$_{60}$**, at 466 nm for **Fc–P$_n$–C$_{60}$** (n ≥ 2) with a shoulder at 495 nm and a broad Q–band ($S_0 \rightarrow S_1$) that extends from ~550 nm to 850 nm. The increasingly broad Q–band observed for long porphyrin systems (n ≥ 2) arises from a large distribution of rotational conformers contributing to ground–state absorption. To enable comparison with the previous study on charge separation in **P$_n$–C$_{60}$** by Kahnt et al.[195], the same excitation wavelength in the Soret band was used to

initiate the charge separation reaction (CS1) in **Fc–P$_n$–C$_{60}$**: 450 nm for **Fc–P$_1$–C$_{60}$** and 495 nm for **Fc–P$_n$–C$_{60}$** (n ≥ 2). Thus, in both studies, dyads and triads, virtually identical conformational distributions are initially excited, and in regard to the similar absorption spectra, formation of the initial charge separated state is expected to occur by a similar charge separation scheme in both dyads and triads.

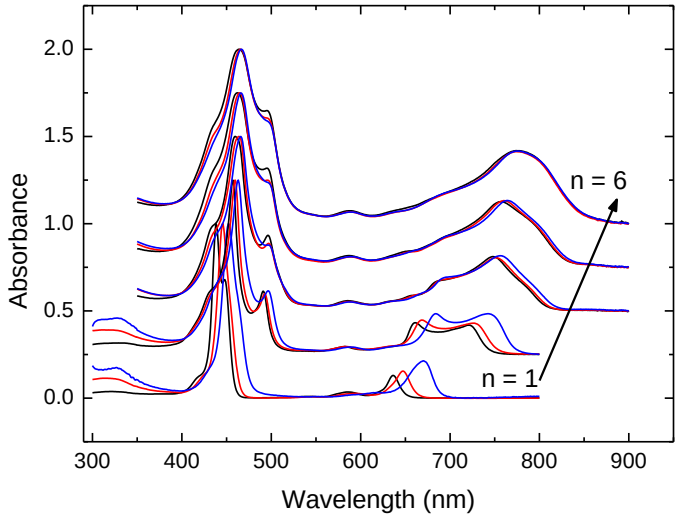

Figure 5.3 Ground–state absorption spectra of **P$_n$** (black), **P$_n$–C$_{60}$** (red) and **Fc–P$_n$–C$_{60}$** (blue) (n = 1–4, 6) at room temperature in 2–MTHF with 1% pyridine added. The spectra have been normalized and offset by (n–1) x 0.25 absorbance units.

Steady–state fluorescence measurements reveal significantly quenched emission of the porphyrin excited state in **Fc–P$_n$–C$_{60}$** compared to their corresponding **P$_n$–C$_{60}$**, **Fc–P$_n$** and reference systems **P$_n$** over the temperature range 180–300 K (see Paper I Figure 4). Despite the competing quenching by energy transfer to the ferrocene group, the initial charge separation is sufficiently efficient that **Fc–P$_n^{\bullet+}$–C$_{60}^{\bullet-}$** is formed for the entire series. Nevertheless, significant differences in the quantum yield for formation of **Fc–P$_n^{\bullet+}$–C$_{60}^{\bullet-}$**, are observed with the length of the porphyrin bridge and/or temperature. When going from **Fc–P$_1$–C$_{60}$** to **Fc–P$_6$–C$_{60}$**, Φ_{CS1} drops from > 0.90 in **Fc–P$_1$–C$_{60}$** to nearly 0.45 in **Fc–P$_6$–C$_{60}$** at room temperature. At lower temperatures, Φ_{CS1} further decreases for the long systems (n ≥ 3). Clear evidence of the similar charge separation scheme in triads and dyads is provided by temperature–dependent fluorescence decays. As mentioned earlier, charge separation may occur via two scenarios: either directly for excitation energy initially localized close to the **C$_{60}$** or in a step–wise fashion with excitation energy migration close to the **C$_{60}$** followed by charge separation. Such charge separation scheme should translate to kinetically more than one rate constant for charge separation. Remarkably, this is confirmed by the measured fluorescence decays for the porphyrin excited states over the temperature range 300–180 K, shown in Figure 5.4. Except for **Fc–P$_1$–C$_{60}$**, all fluorescence decays need to be fitted to bi-exponential expressions. The fitted lifetimes (see Table 5.1) are both shorter than the ones of the corresponding reference compounds **P$_n$** (**P$_1$**: 1450 ps, **P$_2$**:1210 ps, **P$_3$**:1100 ps, **P$_4$**:830 ps and **P$_6$**: 650 ps) and the dyads **Fc–P$_n$** (**Fc–P$_1$**: 7.1 ps and 109 ps, **Fc–P$_2$**: 18 ps and 67 ps,

Fc–P$_4$: 27 ps and 243 ps), confirming the efficient quenching of **Fc–^{1}P$_n^*$–C$_{60}$** by **C$_{60}$**. Looking at the bridge length dependence, both lifetimes increase with the bridge length with the longer lifetime (τ_2) overall contribution increasing with the oligomer length. Longer triads show strong temperature dependence of their lifetimes which increase with decreasing temperature.

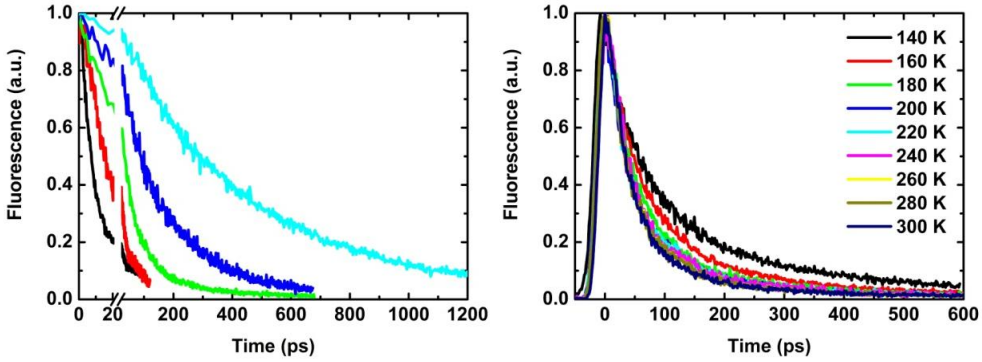

Figure 5.4 (Left) Fluorescence decays for the **Fc–P$_n$–C$_{60}$** compounds at 200 K: **Fc–P$_1$–C$_{60}$** (black), **Fc–P$_2$–C$_{60}$** (red), **Fc–P$_3$–C$_{60}$** (green), **Fc–P$_4$–C$_{60}$** (blue) and **Fc–P$_6$–C$_{60}$** (cyan). (Right) Fluorescence decays for **Fc–P$_3$–C$_{60}$** at different temperatures. All measurements were done in 2–MTHF with 1% of pyridine added. The excitation wavelength was 450 nm for **Fc–P$_1$–C$_{60}$** and 495 nm for **Fc–P$_n$–C$_{60}$** ($n \geq 2$).

Table 5.1 Temperature dependence of the fitted fluorescence lifetimes for Fc–^{1}P$_1^*$–C$_{60}$, Fc–^{1}P$_2^*$–C$_{60}$, Fc–^{1}P$_3^*$–C$_{60}$, Fc–^{1}P$_4^*$–C$_{60}$ and Fc–^{1}P$_6^*$–C$_{60}$ [a]

T / K	Fc–^{1}P$_1^*$–C$_{60}$ [b]	Fc–^{1}P$_2^*$–C$_{60}$		Fc–^{1}P$_3^*$–C$_{60}$		Fc–^{1}P$_4^*$–C$_{60}$		Fc–^{1}P$_6^*$–C$_{60}$	
	τ_1/ps	τ_1/ps	τ_2/ps	τ_1/ps	τ_2/ps	τ_1/ps	τ_2/ps	τ_1/ps	τ_2/ps
300	2.6	8.4	55.3	11.4	58.6	28.4	149.7	N.R.[c]	250.4
280	2.7	8.3	56.6	12.3	60.3	29.2	155.6	53.1	295.7
260	2.7	8.5	57.9	14.0	61.8	31.8	161.0	76.7	301.9
240	2.8	8.6	57.9	14.9	63.7	39.9	175.1	101.6	365.5
220	3.0	9.0	57.9	14.5	64.2	44.1	192.9	119.8	426.9
200	3.4	9.8	73.5	16.8	66.7	49.2	203.0	164.8	475.9
180	3.6	10.0	79.4	19.8	73.9	84.4	242.2	222.2	537.1

[a] The normalized pre–exponential factor are provided in Paper I supporting information Table S2. [b] The lifetimes for **Fc–P$_1$–C$_{60}$** were obtained from single exponential fits. Since the values were below the FWHM of the IRF, femtosecond transient absorption measurements were employed to control the reliability of the fitted values. [c] The notation N.R. refers to lifetimes / pre–exponential that could not be resolved.

Figure 5.5 shows a schematic of the charge separation model in **Fc–P$_n$–C$_{60}$** that can explain the observed bi–exponential and temperature–dependent fluorescence behavior. This model differs from the charge separation model in **P$_n$–C$_{60}$** only by the additional quenching pathway by the ferrocene group (k_Q). Upon photo–excitation of the porphyrin–based bridge, one may distinguish two populations of excited states which differ by where on the bridge excitation energy is initially localized: either far from **C$_{60}$** (i.e. close to the ferrocene) or close to the **C$_{60}$**. The latter population is said to be active and can directly charge–separate, given rise to the short lifetime **τ_1**. However, for the population of porphyrins excited far from the **C$_{60}$**, charge separation is delayed by excitation energy migration, hence the long lifetime **τ_2**. Statistically it gets more and more probable to excite porphyrins moieties far from the **C$_{60}$** as the oligomer length increases. Thus, it is not surprising that **τ_2** makes larger contribution to the fluorescence decay in the longer oligomers ($n \geq 3$). Moreover, **τ_2** shows more pronounced temperature dependence. Pump light of 495 nm primarily excites twisted conformations in the longer oligomers. This means that planarization of the oligomer also occurs in parallel to the charge–separation reaction (*vide supra*). Winters et al.[190] have previously shown that, for **P$_2$**, the perpendicular conformer planarizes within ~100 ps in 2–MTHF at room temperature. Here, excitation energy migration is on the order of 150 ps to 250 ps for long triads ($n \geq 3$) at room temperature, and hence likely to be assisted by planarization of the porphyrin chain. Both lower temperatures and increased solvent viscosity slow down this planarization, and consequently restrain excitation energy migration along the porphyrin chain. This explains the longer **τ_2** observed at low temperatures. Thus, in long **Fc–P$_n$–C$_{60}$**, quenching of **Fc–^{1}P$_n^*$–C$_{60}$** by the ferrocene group and excitation–energy migration significantly limit the outcome of the charge separation reaction (CS1) and explain the lower yield of formed **Fc–P$_n^{\bullet+}$–C$_{60}^{\bullet-}$** measured in steady–state fluorescence.

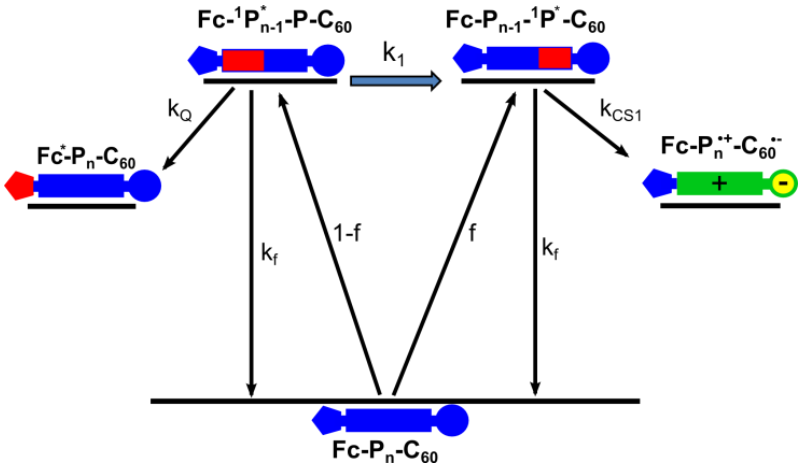

Figure 5.5 Schematic of the charge separation model for the formation of **Fc–P$_n^{\bullet+}$–C$_{60}^{\bullet-}$**. The localized excitation energy is represented in red. k_1 is the rate constant for excitation energy migration and f represents the fraction of excited **Fc–P$_n$–C$_{60}$** molecules which undergo direct charge separation (k_{CS1}). k_Q is the rate constant for the quenching by the ferrocene group.

5.2.2 COMBINING TRANSIENT ABSORPTION WITH TIME–RESOLVED FLUORESCENCE TO INVESTIGATE FORMATION AND DECAY OF RADICAL SPECIES

More direct observation of the formed $\mathbf{Fc–P_n^{\bullet+}–C_{60}^{\bullet-}}$ is the detection of the fullerene anion transient absorption signal in the NIR region. For all $\mathbf{Fc–P_n–C_{60}}$ (n = 1–4, 6), a positive transient at 1018 nm was measured over the entire temperature range 300–180 K. Transient absorption is also a key tool to detect formation and decay of the long–range charge–separated state, $\mathbf{Fc^{\bullet+}–P_n–C_{60}^{\bullet-}}$. Here, the challenge is the absence of transient absorption features that are solely attributed to $\mathbf{Fc^{\bullet+}–P_n–C_{60}^{\bullet-}}$. As the absorption of $\mathbf{Fc^{\bullet+}}$ is very weak,[93, 196-197] $\mathbf{Fc^{\bullet+}–P_n–C_{60}^{\bullet-}}$ and $\mathbf{Fc–P_n^{\bullet+}–C_{60}^{\bullet-}}$ have essentially the same transient absorption features: e.g. for $\mathbf{Fc–P_3–C_{60}}$, a weak positive signal in the region 530–680 nm attributed to both the excited state $\mathbf{^1P_3^*}$ and the radical cation $\mathbf{P_3^{\bullet+}}$ and a strong negative signal at 770 nm dominated by the porphyrin ground–state recovery (see Figure 5.6).[93]

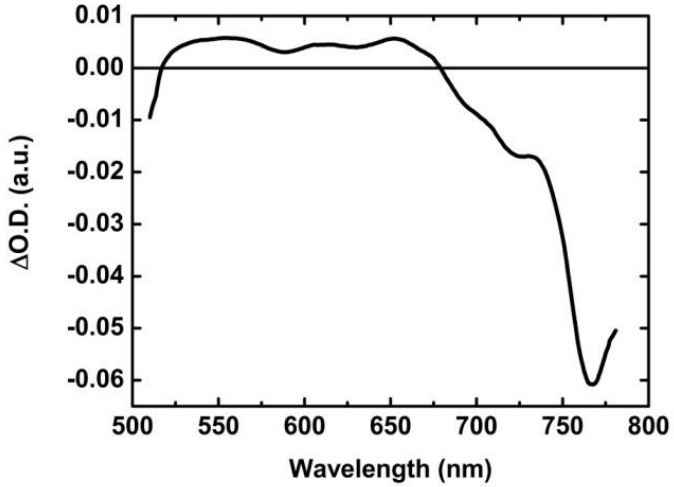

Figure 5.6 Femtosecond transient absorption spectrum of $\mathbf{Fc–P_3–C_{60}}$ in 2–MTHF at 200 K at 75 ps. The pump wavelength was 495 nm.

Since several absorption bands overlap in the region 500–700 nm, this leaves only the porphyrin ground–state bleaching and the transient signal at 1018 nm of $\mathbf{C_{60}^{\bullet-}}$ to follow both charge–separated states. Figure 5.7 shows transient absorption time profiles for the entire series of triads at room temperature. Despite similar absorption features, the two charge–separated states may be distinguished by the time scale on which they form and decay. For all compounds, both transient profiles are multi–exponential. In practice, fitting these transient absorption profiles in an accurate way may be difficult without prior knowledge of the expected lifetimes. However, from time–resolved fluorescence, the lifetimes $\boldsymbol{\tau_1}$ and $\boldsymbol{\tau_2}$ associated with formation of $\mathbf{Fc–P_n^{\bullet+}–C_{60}^{\bullet-}}$ are known and can be used to reduce the number of unknown parameters in the fitting procedure. The porphyrin ground–state recovery contains information on the initial charge separation

reaction as well as the lifetime of **Fc–P$_n^{\bullet+}$–C$_{60}^{\bullet-}$**. Thus, using the lifetimes τ_1 and τ_2 measured in time–resolved fluorescence in the fitting of the porphyrin ground–state recovery enables to extract the lifetime of **Fc–P$_n^{\bullet+}$–C$_{60}^{\bullet-}$**. If the charge shift reaction (CSh) is sufficiently efficient, this lifetime should be shorter than the ones observed for **P$_n^{\bullet+}$–C$_{60}^{\bullet-}$**. This is the case for all **Fc–P$_n$–C$_{60}$** up to the tetramer at room temperature (Table 5.2). Only **Fc–P$_6^{\bullet+}$–C$_{60}^{\bullet-}$** has a lifetime which is nearly the same as for **P$_6^{\bullet+}$–C$_{60}^{\bullet-}$** indicating that the long–range charge–separated state **Fc$^{\bullet+}$–P$_6$–C$_{60}^{\bullet-}$** does not form. Considering now the transient signal at 1018 nm ascribed to **C$_{60}^{\bullet-}$**, its decay must be slower than the porphyrin ground–state recovery if **Fc$^{\bullet+}$–P$_n$–C$_{60}^{\bullet-}$** is formed. At long delay times (> 2 ns), although the porphyrin ground–state absorption is recovered, a small transient absorption is indeed observed that decays according to the lifetime of **Fc$^{\bullet+}$–P$_n$–C$_{60}^{\bullet-}$** (τ_4) in Table 5.3.

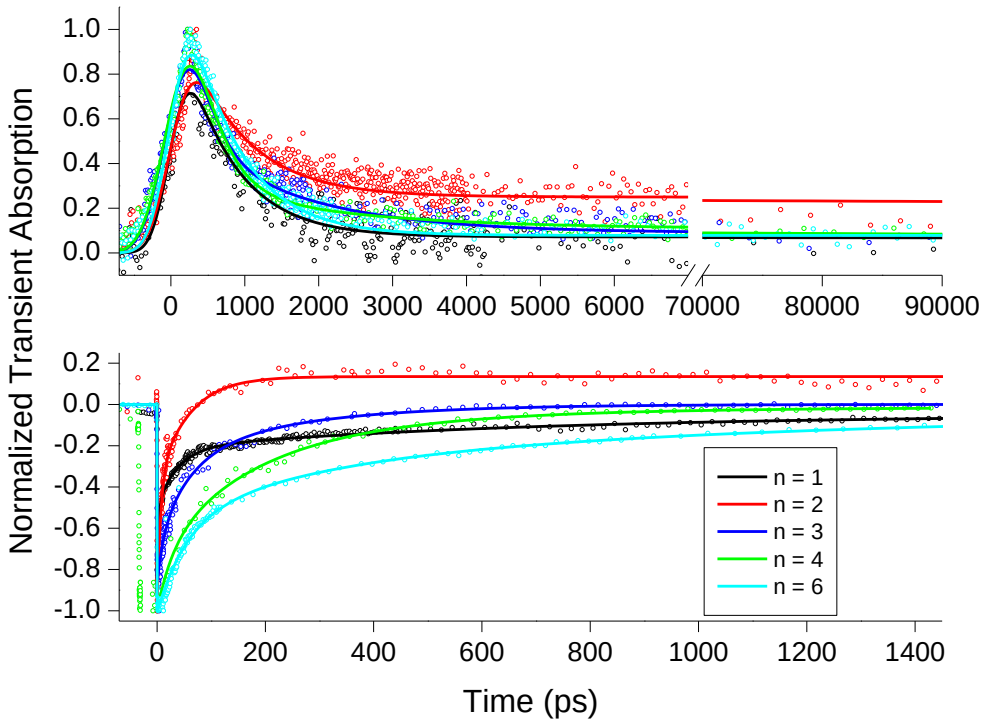

Figure 5.7 Room temperature normalized transient absorption time profiles measured at 1018 nm (top) and in the Q–band (bottom) and their respective fitted curves for **Fc–P$_1$–C$_{60}$** (black), **Fc–P$_2$–C$_{60}$** (red), **Fc–P$_3$–C$_{60}$** (blue), **Fc–P$_4$–C$_{60}$** (green) and **Fc–P$_6$–C$_{60}$** (magenta). The raw data are represented as circles while the fitted curves are shown with solid lines. For more clarity, the transient absorption time profiles measured at 1018 nm are only shown for delay times up to 9 ns but were measured up 800 ns.

Table 5.2 Lifetimes extracted from the fits of time–resolved fluorescence and transient absorption data at room temperature

Lifetime (ps)	n = 1	n = 2	n = 3	n = 4	n = 6
τ ($\mathbf{P_n^*}$)[a]	1450	1210	1100	830	650
τ ($\mathbf{P_{n-1}–P_1^*–C_{60}}$)[a]	4.4	19	20	24	26
τ ($\mathbf{P_{n-1}^*–P_1–C_{60}}$)[a]	–	489	119	216	285
τ ($\mathbf{P_n^{\bullet+}–C_{60}^{\bullet-}}$)[a]	189	276	463	499	643
τ ($\mathbf{Fc–P_{n-1}–P_1^*–C_{60}}$) = $\boldsymbol{\tau_1}$	2.6[b]	8.4[b]	11.4[b]	28.4[b]	N.R.[c]
τ ($\mathbf{Fc–P_{n-1}^*–P_1–C_{60}}$) = $\boldsymbol{\tau_2}$	–	55.3[b]	58.6[b]	149.7[b]	250.4[b]
τ ($\mathbf{Fc–P_n^{\bullet+}–C_{60}^{\bullet-}}$) = $\boldsymbol{\tau_3}$	38	N.R.[c]	237	331	692[d]
τ ($\mathbf{Fc^{\bullet+}–P_n–C_{60}^{\bullet-}}$) = $\boldsymbol{\tau_4}$	687	783	1552	1977	–

[a] From reference [195]. [b] From time–resolved fluorescence measurements. [c] The notation N.R. refers to lifetimes that could not be resolved. [d] For the hexamer **Fc–P$_6$–C$_{60}$**, the fully charge separated state is not formed.

5.2.3 HOPPING VERSUS TUNNELING RECOMBINATION MECHANISMS

The recombination rate constants of the fully charge separated states, k_{CR2}, are simply given by the inverse of the lifetimes $\boldsymbol{\tau_4}$ summarized in Table 5.3. Figure 5.8 shows the plot of ln ($k_{CR2}T^{1/2}$) against the inverse of temperature for **Fc–P$_n$–C$_{60}$** ($n \geq 4$). In case of coherent tunneling, the Marcus equation predicts a linear decrease of ln ($k_{CR2}T^{1/2}$) with T^{-1} (equation 3.20). Here, only data for **Fc–P$_1$–C$_{60}$** describe a straight line that can be fitted to the linearized Marcus equation. The data for longer triads **Fc–P$_n$–C$_{60}$** ($n \geq 2$) clearly deviate from a single straight line and describe seemingly two straight lines with a change in slope above 260 K.

Table 5.3 Lifetimes of $\mathbf{Fc^{\bullet+}–P_n–C_{60}^{\bullet-}}$ obtained from the transient absorption decays at 1018 nm [a]

	τ ($\mathbf{Fc^{\bullet+}–P_n–C_{60}^{\bullet-}}$) = $\boldsymbol{\tau_4}$ / ps			
T/K	n = 1	n = 2	n = 3	n = 4
300	687 ± 94	783 ± 188	1552 ± 147	1977 ± 273
280	749 ± 91	772 ± 184	1822 ± 246	1858 ± 254
260	660 ± 41	1257 ± 304	1888 ± 303	N.R
240	825 ± 70	2510 ± 64	2443 ± 114	4952 ± 1031
220	628 ± 54	2771 ± 34	2843 ± 380	13620 ± 4121
200	1110 ± 178	–	5189 ± 1591	–
180	1261 ± 103	–	–	–

[a] The errors on the lifetimes represent fitting errors. Since a sequential fitting procedure was used, these errors are estimates.

These differences in the temperature dependence of the recombination rates with the porphyrin–bridge length were interpreted by distinct mechanisms governing charge

recombination in **Fc–P$_1$–C$_{60}$** and in long **Fc–P$_n$–C$_{60}$** (n ≥ 2). Detailed analysis of the possible recombination scenarios (Figure 5.2) in accordance to the relevant states energies (see Paper I supporting information Figure S7.1) leads to the conclusion that **Fc$^{\bullet+}$–P$_n$–C$_{60}^{\bullet-}$** recombines to the ground state via coherent electronic tunneling above 280 K for the entire series. Below 280 K, in long triads (n ≥ 2), recombination of **Fc$^{\bullet+}$–P$_n$–C$_{60}^{\bullet-}$** follows a step–wise scheme with first reformation of the oxidized bridge state **Fc–P$_n^{\bullet+}$–C$_{60}^{\bullet-}$** followed by its rapid recombination either to **Fc–^{3}P$_n^*$–C$_{60}$** or to the ground state. This crossover from coherent tunneling at high temperatures to incoherent hopping at low temperatures is rather unusual, especially since incoherent hopping is a thermally activated process and reforming **Fc–P$_n^{\bullet+}$–C$_{60}^{\bullet-}$** is uphill in energy for all triads (n ≥ 2). Nevertheless, it may be rationalized by considering the lifetimes of **Fc$^{\bullet+}$–P$_n$–C$_{60}^{\bullet-}$** (see Table 5.3). Below 260 K, these ones become increasingly long, and hence one may assume that there is a non negligible probability of reforming the oxidized bridge state **Fc–P$_n^{\bullet+}$–C$_{60}^{\bullet-}$** despite the low temperatures.

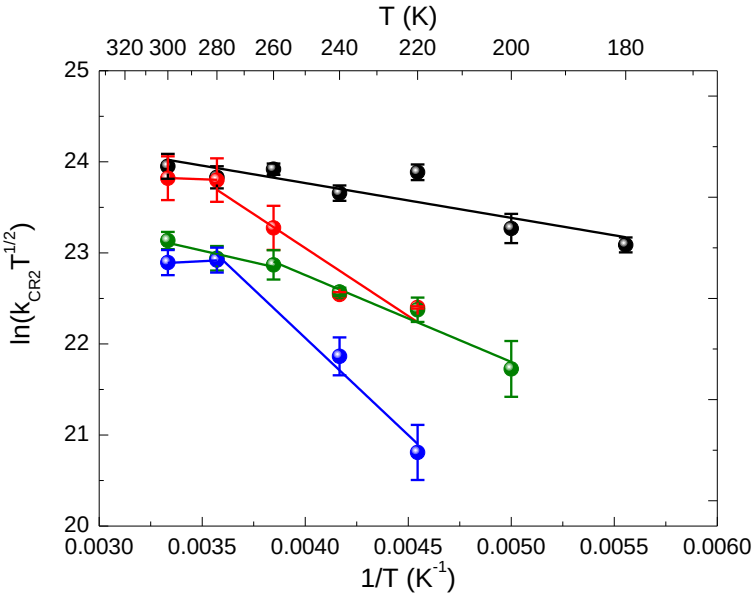

Figure 5.8 Plots of ln(k$_{CR2}$T$^{1/2}$) vs (1/T) for **Fc–P$_1$–C$_{60}$** (black), **Fc–P$_2$–C$_{60}$** (red), **Fc–P$_3$–C$_{60}$** (green) and **Fc–P$_4$–C$_{60}$** (blue). The black solid line for **Fc–P$_1$–C$_{60}$** represents the fit to the linearized form of the Marcus equation, while for other triads **Fc–P$_n$–C$_{60}$** (n ≥ 2), the solid lines are only guides to the reader. The error bars are calculated from the estimated errors on the lifetimes of **Fc$^{\bullet+}$–P$_n$–C$_{60}^{\bullet-}$** reported in Table 5.3.

5.2.4 Concluding remarks

Finally, the distance dependence study (i.e. plot of ln k$_{CR2}$ vs the **Fc**…**C$_{60}$** distance) reaffirms the weakly distance dependent charge transport in **Fc–P$_n$–C$_{60}$** with a β–value of 0.028 Å^{-1} at room temperature (see Paper I Figure 13). Below 280 K, crossover to incoherent hopping translates in empirical β–values higher than for coherent electron tunneling. This work demonstrates that charge transport in the hopping regime does not necessarily lead to wire–like charge transport. In D–B–A systems bridged by strongly

conjugated systems, such as **Fc–P$_n$–C$_{60}$**, charge transport in the tunneling regime may have even weaker distance–dependent charge transport. This example demonstrates again the difficulties in establishing general rules based solely on the charge transport mechanism for the appearance of wire–like properties.[87, 94]

5.3 CONFORMATIONAL CONTROL OF ELECTRON TRANSFER RATES AND EFFICIENCY IN PORPHYRIN–FULLERENE DYADS

A peculiar consequence of the butadiyne linkers in the **P$_n$** systems is a broad distribution of rotational **P$_n$** conformers which spectrally give rise to a broad Q–band (see Figure 5.9). In the donor–acceptor dimer, **P$_2$–C$_{60}$**, Winters et al. have shown that the dihedral angle between the two porphyrin moieties exerts a significant influence on the donor–acceptor electronic coupling (V_{DA}) and the ET rates. By controlling the conformation of the porphyrin chain in **P$_2$–C$_{60}$**, they could tune the rate of electron transfer between the porphyrin and the fullerene. Here, conformational gating of the electron transfer rates in long dyads, i.e. **P$_4$–C$_{60}$** and **P$_6$–C$_{60}$** is investigated.

5.3.1 OPTICAL VS CHEMICAL VS PHYSICAL CONTROL OF CONFORMATION

Several approaches can be envisaged to control the conformational distribution of porphyrin–based systems. Substitution at peripheral positions has been a popular approach to induce geometric control of the torsional angles. For example, McLendon et al. synthesized a series of bis–porphyrin adducts connected at the *meso* positions by a biphenyl group in which they varied the porphyrin–porphyrin dihedral angle by substituting the 2 and 2' positions of the phenyl rings with different groups.[198] In metalloporphyrin–based systems, substitution at the *meso* positions by pyridyl groups has been preferentially used to realize different architectures. In particular, the groups of Kim and Osuka substituted directly linked porphyrin dimers at their *meso* positions with a pyridyl group to form multiporphyrin boxes. Using a similar approach, Aida and co–workers also used *meso*–pyridyl functional groups to induce self–assembly of ethynylene–linked zinc porphyrin dimer into a multiporphyrin box. While this approach enables realization of complex molecular architectures, one disadvantage in regard to device applications is its irreversibility or the absence of the "on demand" function. A more interesting approach to control conformation of supramolecular structures "on demand" is by non–covalent ligand coordination. This approach is particularly adapted to metalloporphyrin oligomers such as the conjugated zinc porphyrin oligomers studied here, for which pyridine or ligands with peripheral pyridyl groups coordinate relatively strongly to the zinc centers. Recently, this approach was successfully employed by Winters et al.[95] to control the electron transfer rate in the dimer **P$_2$–C$_{60}$**. Upon titration with a bipyridyl pyrrole ligand (**L**), **P$_2$–C$_{60}$** forms a strong 1:1 **P$_2$:L–C$_{60}$** complex ($K \sim 4.10^7$ M^{-1} in $CHCl_3$), in which the porphyrin dimer is forced to adopt a planar

conformation. This conformational restriction leads to a significantly reduced rate of electron transfer in the planar **P_2:L–C_{60}** compared to its unconstrained counterpart **P_2–C_{60}** (i.e. with random conformation). In an even simpler approach, they could also control the conformational state of the oligomer using light as an external stimulus. They showed that excitation in the blue–part of the Q–band promoted mostly twisted conformers to the excited state, while excitation in its red–end favored the planar conformer. Applied to the donor–acceptor dimer, **P_2–C_{60}**, this approach produced different initial excited states for charge separation. About four times faster charge separation rates were measured for twisted conformers, due, in part, to an electronic coupling twice as large for these conformers with respect to the planar conformer.

Considering the longer oligomers, **P_4–C_{60}** and **P_6–C_{60}**, a much larger number of rotational conformers exist due to the increasing number of combinations of dihedral angles between the neighboring porphyrin moieties. This renders control of conformation in these long dyads more difficult than in the shorter **P_2–C_{60}**. Nevertheless, the possibility to excite different population of conformers by tuning the excitation wavelength in the Q–band is expected to also prevail for longer oligomers. In particular, time–dependent DFT calculations of the electronic transitions for the planar conformer in the entire series confirm their absorption at long wavelengths in the Q–band (see Paper II Figure 3). Figure 5.9 shows the ground–state absorption spectra of **P_4–C_{60}** and **P_6–C_{60}** with arrows indicating the different excitation wavelengths chosen to prepare different excited states for charge separation. Self–assembly by ligand coordination was also envisaged to restrain the conformational distribution of these long oligomers. In principle, bidentate ligands with pyridyl groups such as the ones used for planarization of **P_2–C_{60}** could have been used. However, these ligands are here far from being ideal since many different complexes could form, i.e. **P_n:L_2–C_{60}**, **P_n:L_1–C_{60}** for $n \geq 4$. Instead multidentate ligands with several pyridyl groups may be used. Here, we used an octa–dentate template with eight axial pyridine groups to prevent rotations of individual porphyrins in **P_4–C_{60}** and **P_6–C_{60}** (Figure 5.16).[199] Upon titration of the porphyrin oligomer with a solution of **T8**, 1:1 **P_n:T8–C_{60}** (n = 4, 6) semi–circular complexes form by coordination of the zinc centers to the pyridyl groups of **T8**. In these complexes, the neighboring porphyrin molecular planes are nearly coplanar. This leads spectrally to a new red–shifted peak growing in at the red–edge of the Q–band and a more structured Q–band, as shown in Figure 5.9. The self–assembled **P_n:T8–C_{60}** dissociate with a large excess of pyridine.[199] The following sections describe how the selected conformation by optical or chemical external stimuli influences the outcome of the charge separation reaction (i.e. kinetics and yield) in long **P_n–C_{60}** (n = 4, 6). In both cases, the charge separation reaction was followed by means of steady–state and time–resolved fluorescence emission. Finally, we demonstrate that temperature may be used as a physical means to control conformational distribution.

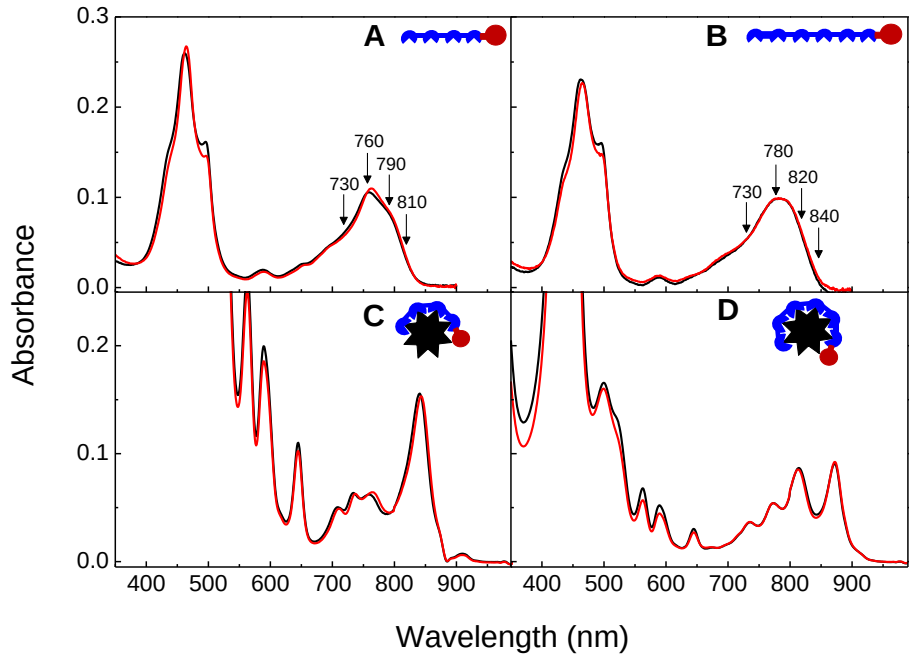

Figure 5.9 Ground–state absorption spectra of the linear systems, (A) $\mathbf{P_4–C_{60}}$ (red) and (B) $\mathbf{P_6–C_{60}}$ (red) in 2–MTHF with 1% pyridine added, and the semi–circular complexes, (C) $\mathbf{P_4}$**:T8–**$\mathbf{C_{60}}$ (red) and (D) $\mathbf{P_6}$**:T8–**$\mathbf{C_{60}}$ (red) in DCM/Toluene (60/40) with 0.1% pyridine added. The absorption spectra of the reference systems, $\mathbf{P_n}$ and $\mathbf{P_n}$**:T8**, are plotted in black. All measurements were done at room temperature. Note that **T8** has only absorption bands in the region from 300 to 650 nm, and hence the absorption bands above 650 nm are exclusively due to the oligomer part of the complexes $\mathbf{P_4}$**:T8–**$\mathbf{C_{60}}$ and $\mathbf{P_6}$**:T8–**$\mathbf{C_{60}}$.

5.3.2 Optical Gating of Electron Transfer

For both $\mathbf{P_4–C_{60}}$ and $\mathbf{P_6–C_{60}}$, as well as their corresponding reference systems $\mathbf{P_n}$ (n = 4, 6), wavelengths in the blue–end of the Q–band (i.e. $\lambda_{exc} < 790$ nm) excite predominantly twisted conformers, while the more planar conformations are excited at excitation wavelengths in the red–end of the Q–band (i.e. $\lambda_{exc} > 790$ nm). In steady–state fluorescence, quenching of the porphyrin emission can be directly related to the charge separation reaction. Small variations of the quantum yield for charge separation, Φ_{CS}, with the excitation wavelength are observed. In general, higher Φ_{CS} values are measured when the conformation initially excited is twisted (e.g. for $\lambda_{exc} = 730$ nm and $\lambda_{exc} = 780$ nm in $\mathbf{P_6–C_{60}}$). However, the information contained in steady–state emission spectra remains limited. 2D time–resolved fluorescence measurements with a streak camera provide more detailed dynamic information on the influence of conformation on the charge separation process. The 2D streak camera emission images of $\mathbf{P_n–C_{60}}$ (n = 4, 6) and respective $\mathbf{P_n}$ systems were recorded with the same excitation wavelengths used in steady–state experiments. As an example, Figure 5.10 shows the 2D streak camera emission images of $\mathbf{P_6–C_{60}}$ at 300 K excited at 730 nm, 780 nm, 820 nm and 840 nm. These images reveal a moderately complex behavior with emission shapes and decays that vary with both excitation and emission wavelength. In agreement with steady–state measurements, fast fluorescence decays are observed at short emission wavelengths

when exciting twisted conformers (λ_{exc} = 730 nm and λ_{exc} = 780 nm), while emissions of more planar conformers (λ_{exc} = 820 nm and λ_{exc} = 840 nm) decay much slower over the entire emission wavelength range. The variation of the fluorescence decays with emission wavelength is highlighted in Figure 5.11, which compares extracted fluorescence decays at different emission wavelengths of **P_6–C_{60}** excited at 780 nm. 2D streak camera emission images of **P_4–C_{60}** measured with λ_{exc} in the range 730–810 nm showed similar excitation and emission wavelength dependency of fluorescence (see Paper II supporting information). Such behavior is rationalized by the combination of processes occurring in the excited state for twisted conformers, i.e. structural relaxation (via planarization) and charge separation.

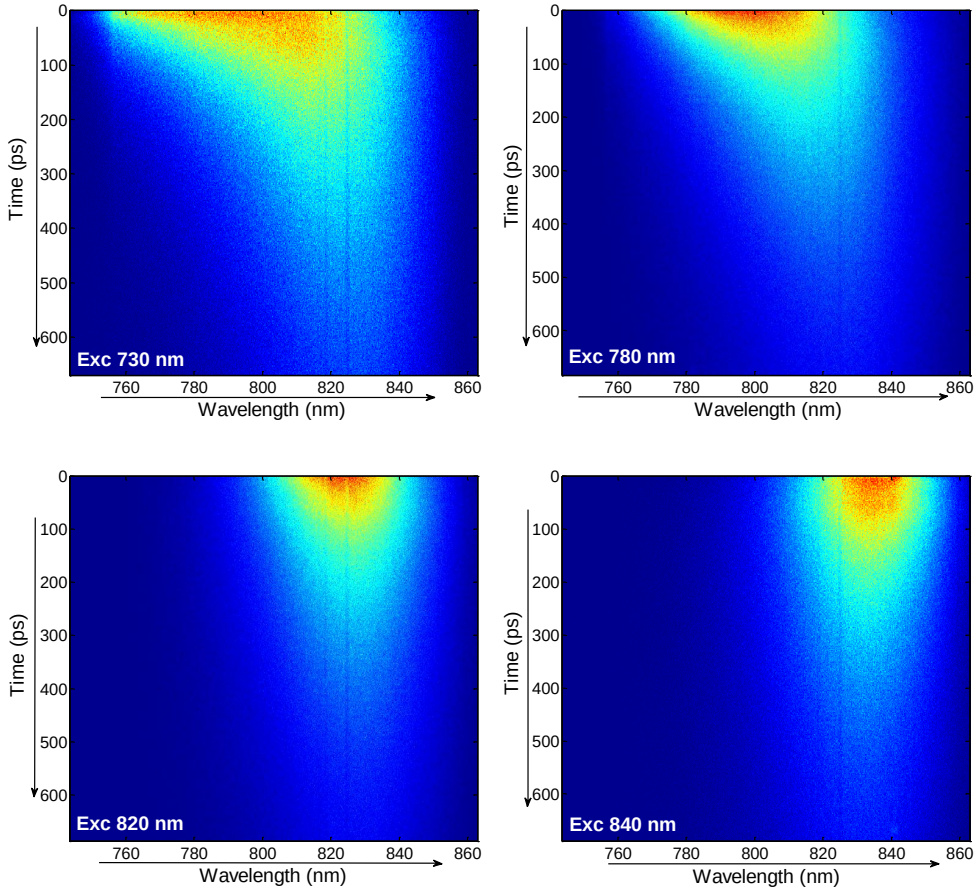

Figure 5.10 2D streak camera emission images of **P_6–C_{60}** at 300 K in 2–MTHF with 1% pyridine excited at 730 nm (top left), 780 nm (top right), 820 nm (bottom left) and 840 nm (bottom right).

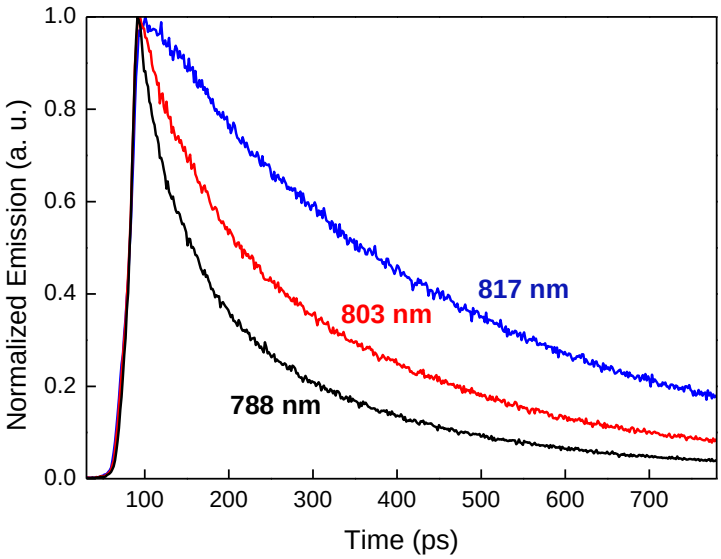

Figure 5.11 Extracted fluorescence decays of $\mathbf{P_6–C_{60}}$ at three emission wavelengths 788 nm, 803 nm and 817 nm. The excitation wavelength was 780 nm.

In practice, separating both processes and extracting the rate constants associated to each process can be difficult. However, by performing a singular–value–decomposition analysis (SVD) of the emission data, we can first determine the number of excited states that significantly contribute to the emission (see Section 4.4.2). In general, when exciting twisted conformers, fitting of the fluorescence decays requires a three–state model in which twisted excited states relax into more planar conformers. Figure 5.12 shows the three–state model describing relaxation of the reference porphyrin oligomers with $P_n^{\#}$, $P_n^{¤}$ and P_n^{*} representing a twisted, intermediately twisted and planarized oligomer in the excited state, respectively. For the donor–acceptor systems, a similar three–state model can be used in which charge separation from either non–relaxed or relaxed states can occur in addition to planarization and natural decays. To reduce the number of unknown parameters, the rates constants related to planarization (k_1, k_2) and natural decays ($k^{\#}$, $k^{¤}$, k^{*}) are assumed to be the same in $\mathbf{P_n}$ and $\mathbf{P_n–C_{60}}$ and are obtained from the fitted fluorescence decays of $\mathbf{P_n}$.

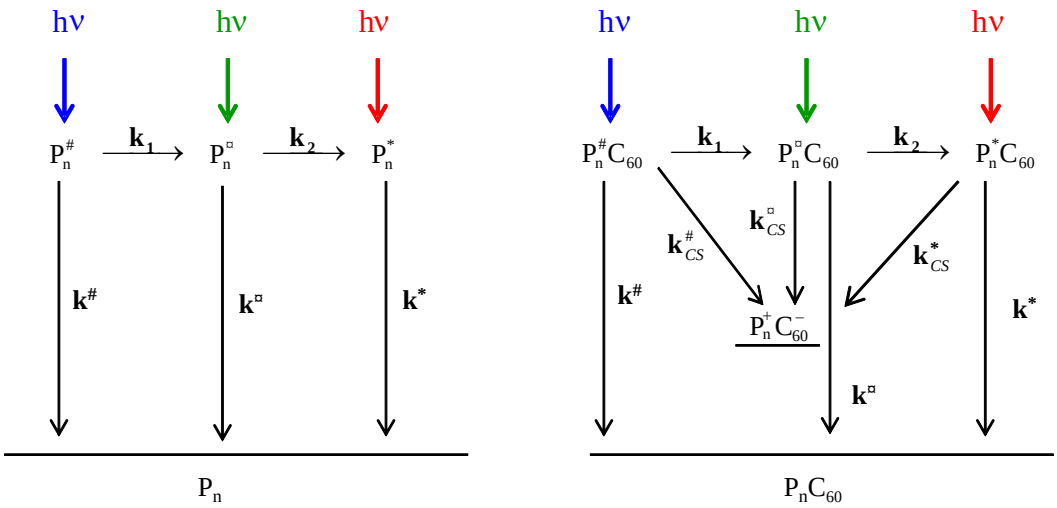

Figure 5.12 Three–state models describing (left) the excited state structural relaxation in the model systems **P_n** and (right) the interplay between excited state structural relaxation and charge separation in the donor–acceptor **P_n–C_{60}**. The different rate constants involved are explained in the text.

This SVD–based analysis enables spectral and temporal resolution of the different conformational populations that contribute to the emission. Figure 5.13 shows an example of this analysis applied to the room temperature 2D streak camera emission image of **P_6–C_{60}** excited at 730 nm. Three populations of conformers contribute to the fluorescence emission in this case (Figure 5.13c). The first population (in blue) emits over nearly the entire wavelength range but dominates the emission at short wavelengths, while the third one (in red) emits mostly at longer wavelengths. Looking at their respective decays (Figure 5.13d), the first population of conformers may be assigned to twisted conformers and decays with a short lifetime, while the third population arises from two consecutive relaxations of twisted conformers and represents the relaxed planar conformer. The measured (Figure 5.13a) and reconstructed (Figure 5.13b) 2D emission images agree reasonably well supporting the validity of the proposed model, although one may discern an overestimation of the fast decays (i.e. charge separation occuring from non–relaxed states). This may be due to the assumption made in the fitting procedure that is an excitation energy initially located close to **C_{60}**. We neglect the fact that in these long oligomers, porphyrin units far from the **C_{60}** may initially be excited (see Figure 5.5 and the discussion of charge separation in the **Fc–P_n–C_{60}** systems *vide supra*).

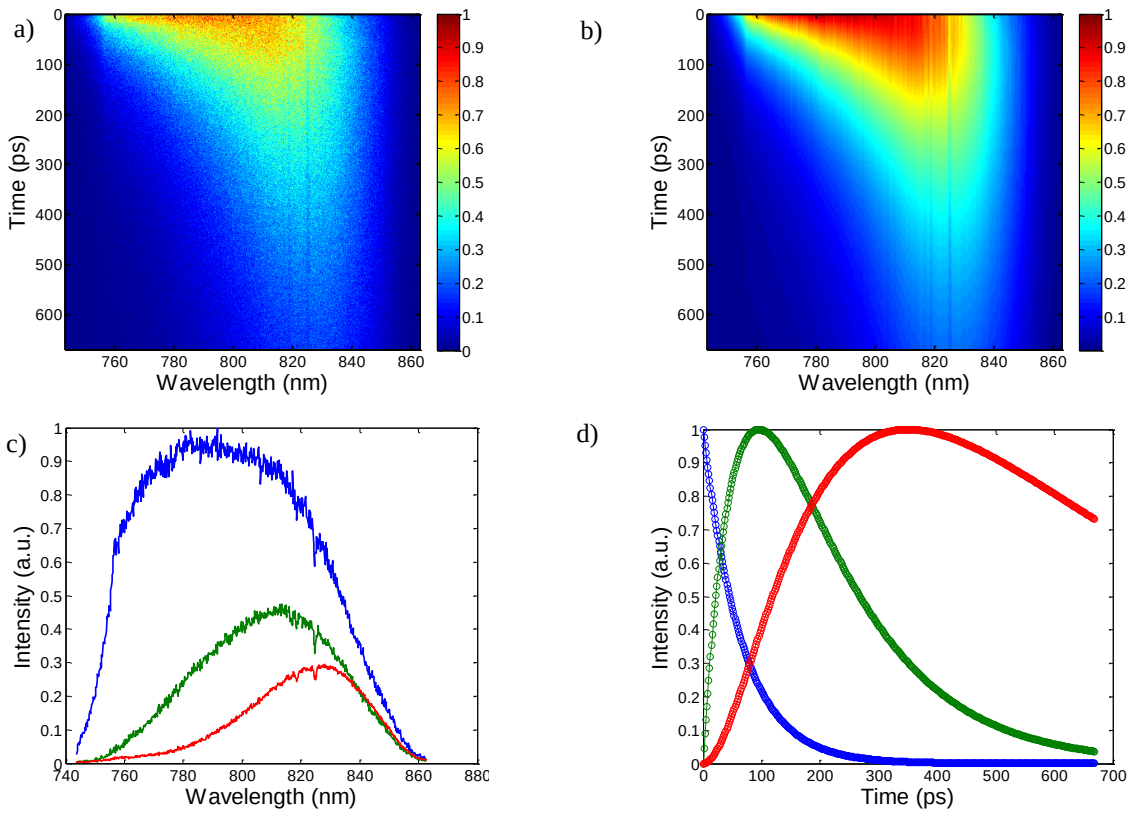

Figure 5.13 a) Normalized 2D streak camera emission image of **P_6–C_{60}** excited at 730 nm at 300 K in 2–MTHF with 1% pyridine. b) Reconstructed 2D emission image of **P_6–C_{60}** excited at 730 nm. This image was built from the data obtained in the fitting procedure. c) Spectral components and d) decays of the 3 species contributing to the fluorescence emission. The color code used in c) and d) is the same, i.e. the fluorescence decay in blue corresponds to the species with the blue emission spectrum etc.

The charge separation rate constants derived from the fitting procedure are summarized as a function of excitation wavelength for **P_4–C_{60}** and **P_6–C_{60}** in Table 5.4. Independently of the excitation wavelength and the size of the oligomer, charge separation is most efficient from non–relaxed states. When exciting twisted conformations of **P_6–C_{60}** (λ_{exc} = 730 nm and λ_{exc} = 780 nm), the charge separation rate constants of the non-relaxed states ($k_{CS}^{\#}$) is at least 20 times larger than the ones from the relaxed planar conformers (k_{CS}^{*}). Direct excitation of more planar conformers (λ_{exc} = 840 nm) leads to very slow charge separation k_{CS}^{*} = 0.9 x 10^9 s^{-1}. This difference in kinetics is well reflected in the calculated charge separation quantum yields, Φ_{CS}, shown in Figure 5.14 as a function of excitation wavelength for **P_6–C_{60}**.

Table 5.4 Wavelength dependence of the charge separation rate constants for P_4–C_{60} and P_6–C_{60} at 300 K[a]

P_4–C_{60}				P_6–C_{60}			
λ_{exc}/nm	$k_{CS}^{\#}$/ns^{-1}	$k_{CS}^{¤}$/ns^{-1}	k_{CS}^{*}/ns^{-1}	λ_{exc}/nm	$k_{CS}^{\#}$ /ns^{-1}	$k_{CS}^{¤}$ /ns^{-1}	k_{CS}^{*} /ns^{-1}
730	13.1	2.7	0.9	730	8.6	0.0	0.3
760	14.9	2.7	0.0	780	8.8	2.8	0.5
790	-	7.4	1.5	820	-	3.3	0.5
810	-	6.0	0.6	840	-	0.0	0.9

[a] Estimated average errors in the fitted rate constants are below $0.5 \cdot 10^9$ s^{-1}.

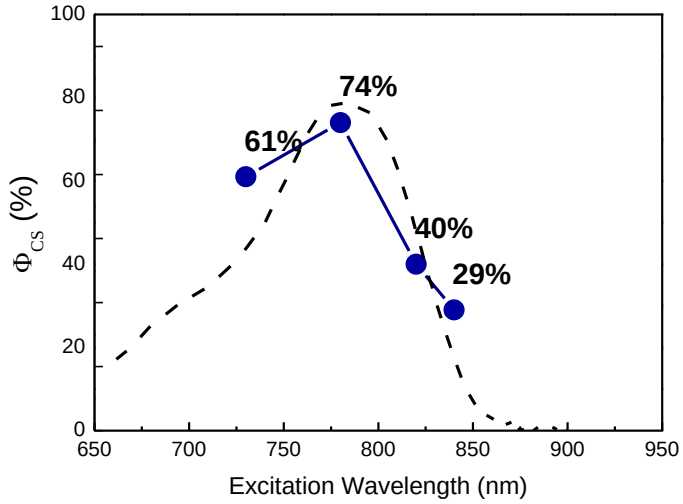

Figure 5.14 Charge separation quantum yield Φ_{CS} as a function of excitation wavelengths within the Q–band based on time–resolved fluorescence measurements for **P_6–C_{60}** in 2–MTHF with 1 % pyridine added at 300 K. The Q–band region of the absorption spectrum of **P_6–C_{60}** is reproduced in grey dashed line for indication to the reader.

The charge–separation rate constant depends on several factors: the electronic coupling, the reorganization energy and the thermodynamic driving force for charge separation (equation 3.20). The driving forces for charge separation between **P_n** and **C_{60}** are quite small. When going from n = 1 to n = 6, the driving force decreases from –0.6 eV to –0.2 eV.[93] Here, the overall rate of charge separation decreases when going from **P_4–C_{60}** to **P_6–C_{60}** in agreement with the decreasing driving forces with increasing oligomer length, confirming that the charge separation process is in the Marcus normal region. Considering driving force differences between different populations of conformers, larger driving forces are expected for non–relaxed twisted conformers since they lie at higher energy in the excited state as shown in Figure 5.15.[95, 190] Planar conformers due to the increased conjugation are more stabilized in the excited state, and hence lie closer

to the charge–separated state energy level. This means that the driving force for charge separation is very small and hence the slow charge separation rate constants observed for more planar conformers. Of course, other factors, such as the reorganization energy and electronic coupling may affect the charge separation rate. Here, the measurements performed at room temperature did not permit access to V_{DA} and λ for the different sets of conformers. A previous study on the temperature dependence of the charge separation in **P_n–C_{60}** revealed nearly length–independent reorganization energies. What cannot be discerned is how electronic coupling varies for different population of conformers. Nevertheless, calculation of the activation energy barrier $\Delta G^{\neq}$ using previously reported λ values gives substantial differences in $\Delta G^{\neq}$ between twisted and planar conformers due to large difference in driving forces. This explains, in part, the distinct charge separation rate constants observed for different excited populations of conformers in long **P_n–C_{60}** (n = 4, 6).

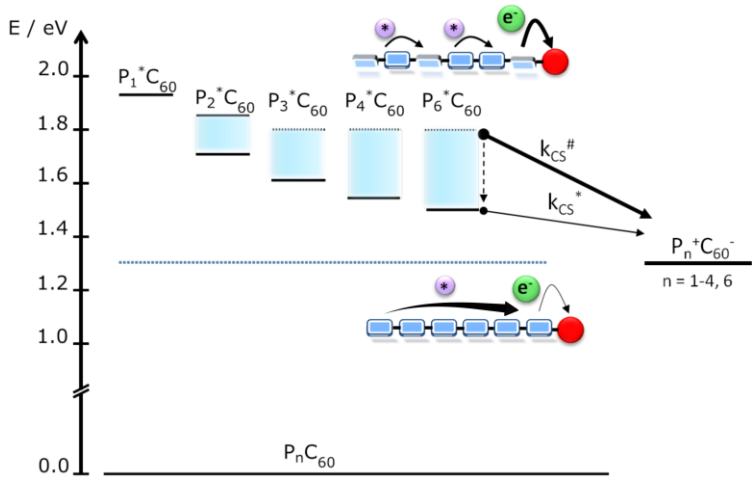

Figure 5.15 Energy diagram for the charge separation process. The distribution of conformers gets broader as the length of the oligomer increases. The methods used to determine the energies of the excited and charge separated states are described in Paper II supporting information.

5.3.3 CHEMICAL GATING OF ELECTRON TRANSFER

Alteration of the conformation in long **P_n–C_{60}** (n = 4, 6) may be realized by ligand coordination. Both **P_n–C_{60}** and **P_n** systems form 1:1 semi–circular complexes with the octadentate ligand **T8** denoted **P_n:T8–C_{60}** and **P_n:T8**, respectively. The molecular structure of **P_6:T8–C_{60}** is shown in Figure 5.16. In contrast to their linear counterparts, these semi-circular complexes have dramatically reduced conformational heterogeneity. Coordination of the pyridyl groups of **T8** to the zinc centers hinders the rotational motions of individual porphyrins and induces a nearly coplanar arrangement of neighboring porphyrins. Since **T8** only absorbs in the wavelength region from 300 nm to 650 nm, this gives use the possibility to excite above 650 nm exclusively the oligomer part of the complexes **P_4:T8–C_{60}** and **P_6:T8–C_{60}** with excitation wavelengths

similar to the ones used for unconstrained systems (*vide supra*). As a result of increased rigidity, no clear excitation wavelength dependence of the charge separation quantum yields was observed in these semi–circular complexes when varying the excitation wavelength within the Q–band (Figure 5.16). Moreover, charge separation was slow and inefficient compared to the linear counterparts (Table 5.5). The charge separation rate constants were comparable to the ones observed for the relaxed (planar) linear conformers (k_{CS}^{*}). The nearly coplanar arrangement of individual porphyrins in **P_n:T8–C_{60}** (n = 4, 6) result in excited states of these complexes that lie very close to the charge–separated state energy level, and hence a small driving force for charge separation can be expected.

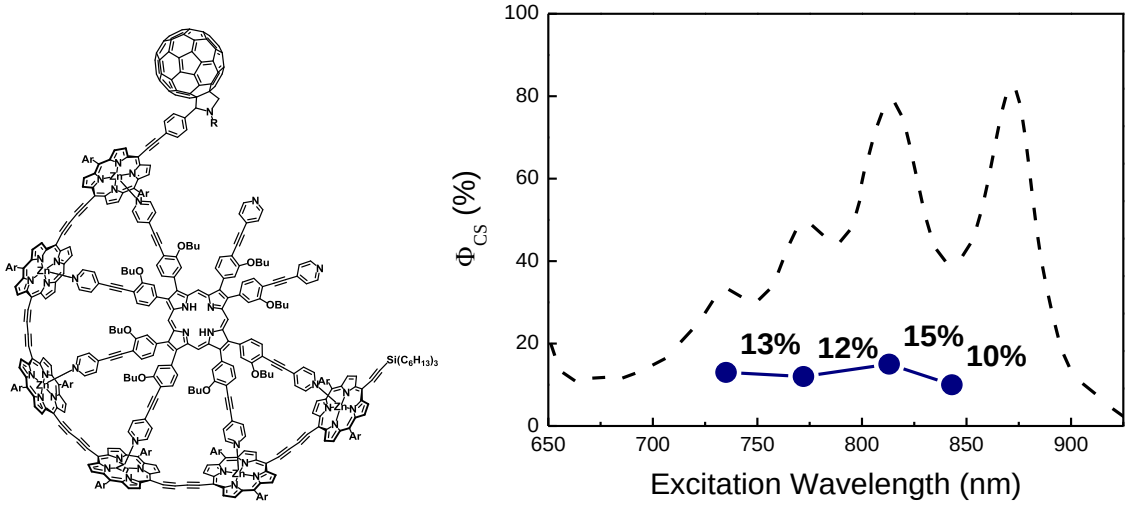

Figure 5.16 (left) Molecular structure of the semi–circular complex **P_6:T8–C_{60}**. (right) Quantum yield for charge separation for excitation wavelengths within the Q–band based on time–resolved fluorescence measurements for **P_6:T8–C_{60}** in DCM/Toluene (60/40) with 0.1 % pyridine added at 300 K. The Q–band region of the absorption spectrum is reproduced in grey dashed line for indication to the reader.

Table 5.5 Fluorescence lifetimes τ_f, rate constants for charge separation k_{CS} and quantum yield for charge separation Φ_{CS} for P_n:T8–C_{60} complexes excited at 735 nm

	τ_f (**P_n:T8**)/ps	τ_f(**P_n:T8−C_{60}**)/ps	k_{CS}/s^{-1} [c]	Φ_{CS} [d]
Tetramer System [a]	499	398	0.51×10^9	0.20
Hexamer System [b]	430	374	0.35×10^9	0.13

[a]The lifetimes for **P_4:T8** and **P_4:T8–C_{60}** were obtained from fitting the fluorescence decays measured using TCSPC. [b]The lifetimes for **P_6:T8** and **P_6:T8–C_{60}** were obtained from fitting the fluorescence decays measured using a streak camera system. [c]The charge separation rate constant k_{CS} was determined using the formula $k_{CS} = 1/\tau_f$ (**P_n:T8–C_{60}**) – $1/\tau_f$ (**P_n:T8**). [d]The quantum yield for charge separation Φ_{CS} was calculated as $\Phi_{CS} = k_{CS} \cdot \tau_f$ (**P_n:T8–C_{60}**).

5.3.4 TEMPERATURE–INDUCED SELF–ASSEMBLY OF P_N, P_N–C_{60}, FC–P_N–C_{60} MOLECULES

Another approach to restrain the conformational distribution in strongly conjugated systems is by using temperature as an external stimulus. The absorption spectra of the entire series $\mathbf{P_n}$ (n = 1–4, 6, 8) are measured upon lowering the temperature. From 300 K to 170 K, not much happens to the absorption spectra. However, below 170 K, drastic changes particularly in the Q–band region are observed for longer oligomers (n ≥ 4). Figure 5.17 shows the temperature–dependent ground–state absorption spectra for $\mathbf{P_8}$, $\mathbf{P_6}$ and $\mathbf{P_4}$. All oligomers show similar changes in their absorption spectra below 170 K: a more structured Q–band and a new absorption band at the red–edge of the Q–band. This new red–shifted peak is similar to the ones observed in semi–circular complexes due to coplanar adjacent porphyrin units (see Figure 5.9), and suggests a planarization of the oligomers below 170 K. These spectral changes also resemble the ones observed in the formation of J–aggregates.[200-201] We concluded that the porphyrin oligomers spontaneously self–assembled at low temperatures into highly ordered planar aggregates. These planar aggregates reversibly disassemble by raising the temperature again. Self–assembly is dependent on the cooling speed, with quick cooking from room temperature to 77 K avoiding their formation.

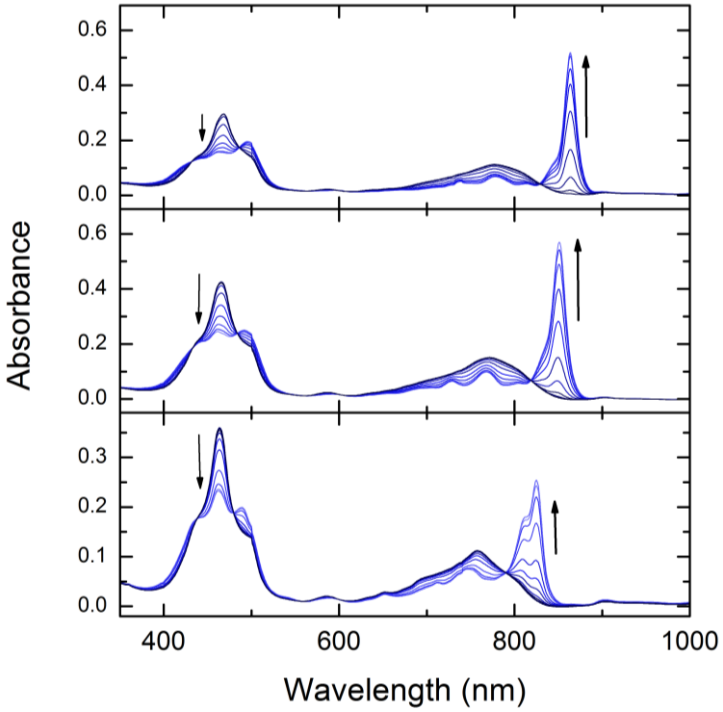

Figure 5.17 Temperature–dependent absorption of $\mathbf{P_8}$ (upper), $\mathbf{P_6}$ (middle) and $\mathbf{P_4}$ (lower) in 2–MTHF. The displayed temperature intervals are 170–150 K for $\mathbf{P_8}$ and $\mathbf{P_6}$ and 165–135 K for $\mathbf{P_4}$. A weak baseline distortion at 900 nm is observed at lower temperature and is attributed to changes in the solvent absorptivity (vibrational overtone absorption).

To relate the observed spectral changes to the structure of these aggregates, a SVD analysis of the absorption data was performed. For all **P_4**, **P_6** and **P_8**, two spectral components contribute to the absorption spectra below 170 K, as shown by several isobestic points in the absorption spectra. Self–assembly could be well described by a two–state model between the free oligomer and the aggregate,

$$2\ P_n \leftrightarrows (P_n)_2 \qquad 5.1$$

Figure 5.18 shows the extracted spectral components for **P_8**, corresponding to free **P_8** (dashed line) and a dimeric array (solid line) along with the evolution of their respective concentration with temperature. Table 5.6 summarizes the optimized enthalpy, entropy changes and melting temperatures associated to the dimerization obtained from the fitting procedure. The enthalpy (ΔH) and entropy (ΔS) changes become more negative and decrease nearly linearly with the oligomer size while the melting temperature (T_m) increases with the length of the oligomer. The large negative ΔS–values point towards highly ordered aggregates. The ΔH–value decreases with ca. – 20 kJ/mol per porphyrin unit added to the oligomer chain. This value is lower than the value reported by Hunter and Sanders for π–π interactions between two zinc porphyrins (i.e. 48 ± 10 kJ/mol).[202] Such difference may lie in the distinct solvent used in these two studies and/or different π–π interactions between the porphyrins. From this analysis, we conclude that self–assembly is likely to result from intermolecular π–π interactions between zinc porphyrin units and produces monodisperse, highly ordered, dimeric **P_n** arrays.

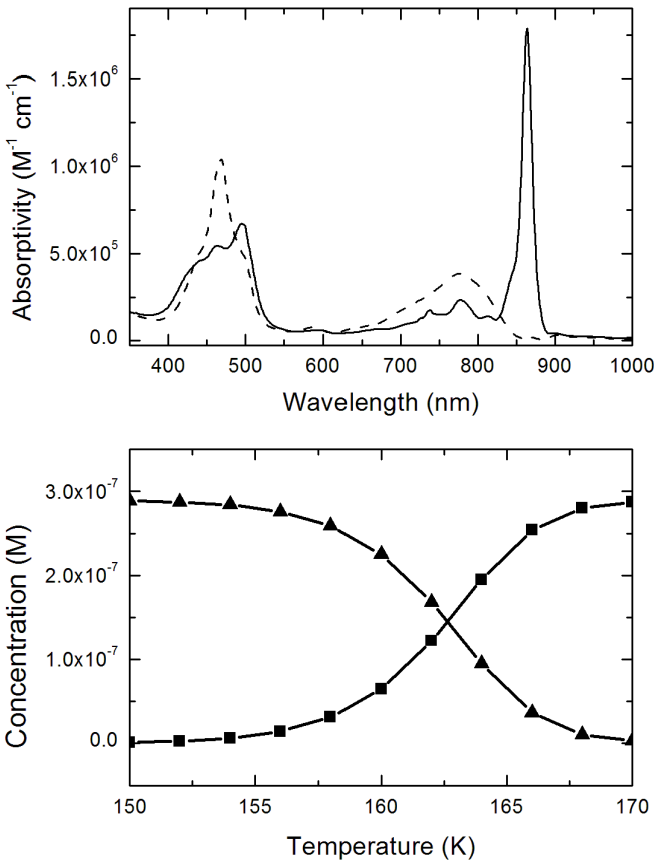

Figure 5.18 (Top) The two most significant spectral components extracted from SVD-analysis of the $\mathbf{P_8}$ dimerization and (Bottom) the corresponding concentration profiles of the monomer (squares) and the dimer (triangles). The spectral profiles and concentration variations correspond to the optimized enthalpy (ΔH) and entropy (ΔS) values in Table 5.6. The dimer concentration is displayed in units of $\mathbf{P_8}$ concentration.

Table 5.6 Optimized enthalpy and entropy changes of the porphyrin oligomer dimerization and melting temperatures extracted from the fit[a]

	ΔH (kJ/mol)	**ΔS (J/mol K)**	**T_m (K)**
Tetramer	-86	-459	146
Hexamer	-137	-749	158
Octamer	-168	-906	163

[a]T_m is the apparent melting temperatures where 50 % of the oligomers have formed aggregates. The total oligomer concentration is 0.19 μM for $\mathbf{P_4}$, 0.48 μM for $\mathbf{P_6}$ and 0.29 μM for $\mathbf{P_8}$.

For supramolecular arrays in solution, small and wide angle X–ray scattering often enable to determine their structures, and hence establish direct structure-property relationship. Here, the low temperature condition for formation of these aggregates prevents us to use these tools to determine their structure and size. Instead, we performed resonance light scattering, dynamic light scattering and steady–state fluorescence anisotropy measurements, that all showed virtually no change in signal

before and after aggregation. Hence, a rather small aggregate can be assumed from these experiments. Another indication of small aggregates arises from the very similar fluorescence rate constants in the free oligomer and the aggregate (see Table 5.7). Note that these measurements are done at 163 K, i.e. a temperature at which both free oligomer and aggregate are present in nearly identical concentrations (see Figure 5.18). This suggests that the transition dipole moments in the free oligomer and the aggregate are comparable in size. This can only be envisioned for a small stack of the oligomers. This is further supported by formation of these aggregates in presence of a small amount of pyridine (1 %) showing similar but red–shifted absorption spectra. An identical red–shift of the absorption spectra is obtained when adding pyridine to a solution of free oligomers as pyridine coordinates to the zinc atoms. If large stacks of porphyrin oligomers form, only few peripheral zinc atoms will be accessible to pyridine. This will give at most a minor red–shift of their absorption spectra. Here, the observed red–shift is clearly non negligible with the strongest absorption peak in the Q–band red–shifted by 12 nm, indicating that most zinc atoms in the stack are exposed to pyridine.

Table 5.7 Fluorescence quantum yields (Φ_f) and lifetimes (τ_f) and radiative rate constant (k_f) of the free and aggregated porphyrin octamer measured at 163 K where approximately half of the oligomers have converted to aggregates.

Compound	Φ_f[a]	τ_f(ps)[b]	k_f(ns^{-1})
Free octamer	10 %	930	0.107
Aggregate	7 %	575	0.122

[a]Optical density of the two species at the excitation wavelength was scaled with their corresponding absorptivities and their individual emission spectra was obtained by subtracting the contribution from the other species. The quantum yield of $\mathbf{P_6}$ in toluene was used as reference.[203] [b]The sample was excited at 495 nm and the emission decay was measured at 800 nm and 867 nm for the free octamer and aggregates respectively.

Finally, the D–A systems, $\mathbf{P_n–C_{60}}$ and $\mathbf{Fc–P_n–C_{60}}$, absorption spectra undergo identical changes to $\mathbf{P_n}$ below 170 K (see Paper III Figure 8). This indicates that low temperature also favors their self–assembly into highly ordered planar aggregates. The formation of such aggregates for $\mathbf{P_n–C_{60}}$ and $\mathbf{Fc–P_n–C_{60}}$ is at first quite surprising since the bulky $\mathbf{C_{60}}$ could impose significant steric hindrance to the stacking. Once more, we conclude that only small stack of $\mathbf{Fc–P_n–C_{60}}$ or $\mathbf{P_n–C_{60}}$ can accommodate such bulky group like $\mathbf{C_{60}}$. We propose a dimeric $\mathbf{P_n–C_{60}}$ array with a structure similar to the one sketched in Figure 5.19.

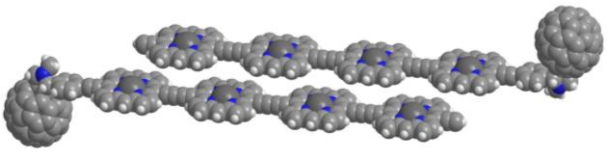

Figure 5.19 Schematic structure of the dimeric $\mathbf{P_4–C_{60}}$ aggregate.

5.3.5 CONCLUDING REMARKS

These arrays of planar $\mathbf{P_n–C_{60}}$ and $\mathbf{Fc–P_n–C_{60}}$ may be of interest for energy migration and charge transport studies in self–assembled non–covalent structures. Practically their formation is easy compared to semi–circular complexes whose multi–dentate ligands require some synthetic work. However, important questions remain: how efficient are intermolecular electronic communication within the stack and photoinduced charge separation in these aggregates? Upon photo–excitation of the stack, does one–electron or two–electron reduction occur? Given our observation of low charge separation efficiency for nearly coplanar porphyrins in semi–circular complexes, we may predict that charge separation in these planar aggregates will also be slow and of low efficiency.

6 EXCITON ENERGY TRANSFER: A COMPARISON BETWEEN WEAKLY AND STRONGLY CONJUGATED MULTICHROMOPHORE SYSTEMS

*Common theme in many areas ranging from nuclear physics to materials science to biology is the transport of energy from one site to another with the question of what govern its kinetics and efficiency. In the context of the natural photosynthesis, this question may be reformulated as how energy is efficiently transferred from the initial location of photon absorption to the reaction center. Even though the crystal structures of some light harvesting complexes are now known,[204-205] it remains difficult to predict kinetics and overall efficiency of the energy transfer from the antenna to the reaction center. Part of this challenge lies in the complexity of the natural light harvesting complexes which involve many subsystems rendering in vivo energy transfer studies difficult. Another difficulty is linked to a broad landscape of electronic couplings between chromophores, from strong to weak, which arises from some chromophores in the light harvesting complexes being very close to each other and other remaining far away from each other. Consequently, excitation energy is not transferred from the antenna to the reaction center via a single mechanism but via a combination of short–range and long–range energy mechanisms (e.g. FRET, exciton coupling). Here, two synthetic multichromophoric systems, i.e. anthracene dendrimers **G1** and **G2** and the butadiyne–linked zinc porphyrin oligomers $\mathbf{P_n}$ (n = 1–4, 6, 8) previously introduced, are used as simple model systems to investigate the influence of linker topology on the inter–chromophore communication and resulting excitation energy transfer (EET). Both systems possess sufficient structural rigidity that enables spatial control of the relative orientation and distance of neighboring chromophores. The results presented in this chapter are from the original work in Papers IV–V. This work attempted to bring some answers to the following questions: to what extent does the linker topology influence the inter–chromophore communication? Do chromophores in the studied systems behave as chromophores in the absence of the others or do they form a new chromophore with distinct properties from the individual chromophoric components?*

In the following sections, after introducing the anthracene dendrimers, we first examine the influence that the linker topology has on the overall photophysical properties of these multichromophoric systems using steady–state absorption and emission, fluorescence lifetimes. In the second part, we investigate excitation energy migration in the anthracene dendrimers and the linear porphyrin oligomers using different spectroscopic methods, fluorescence anisotropy and pump–power dependent transient absorption, respectively.

6.1 ANTHRACENE DENDRIMERS

Two generations of conjugated anthracene dendrimers denoted **G1** and **G2** were investigated as three–dimensional multichromophoric model system for energy transfer. Figure 6.1 shows their molecular structure that contains 3 and 9 anthracene units, respectively. In contrast to the conjugated porphyrin oligomers, these dendrimers are conformationally more constrained due to large steric hindrance preventing the anthracene planes to be co–planar. Their photophysical properties have been characterized and compared to the reference system, 9,10–diphenylanthracene **DPA** (*vide infra*).

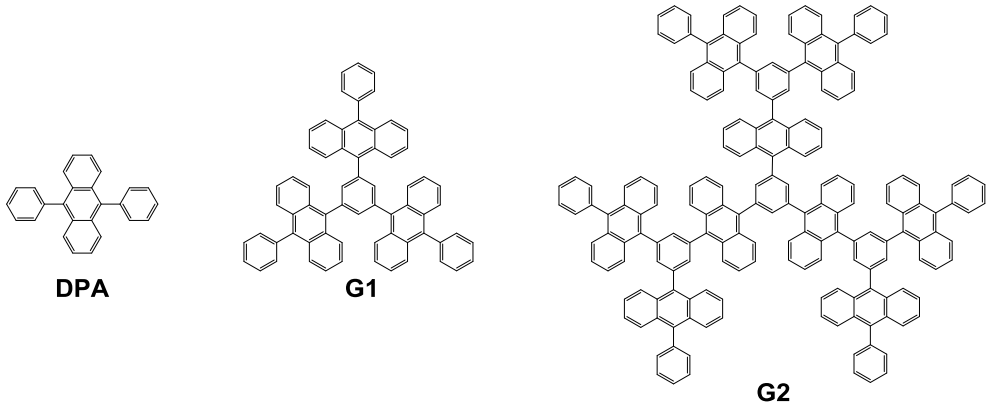

Figure 6.1 Molecular structures of **DPA**, **G1** and **G2**.

6.2 INFLUENCE OF LINKER TOPOLOGY ON THE PHOTOPHYSICAL PROPERTIES: ANTHRACENE DENDRIMERS VS PORPHYRINS OLIGOMERS

A first evidence of through–space and/or through–bond electronic interactions between neighboring chromophores in **G1** and **G2** and in the $\mathbf{P_n}$ systems can be obtained from the comparison of their absorption spectra to the ones of their respective monomer reference, i.e. **DPA** and $\mathbf{P_1}$ (see Figure 6.2).

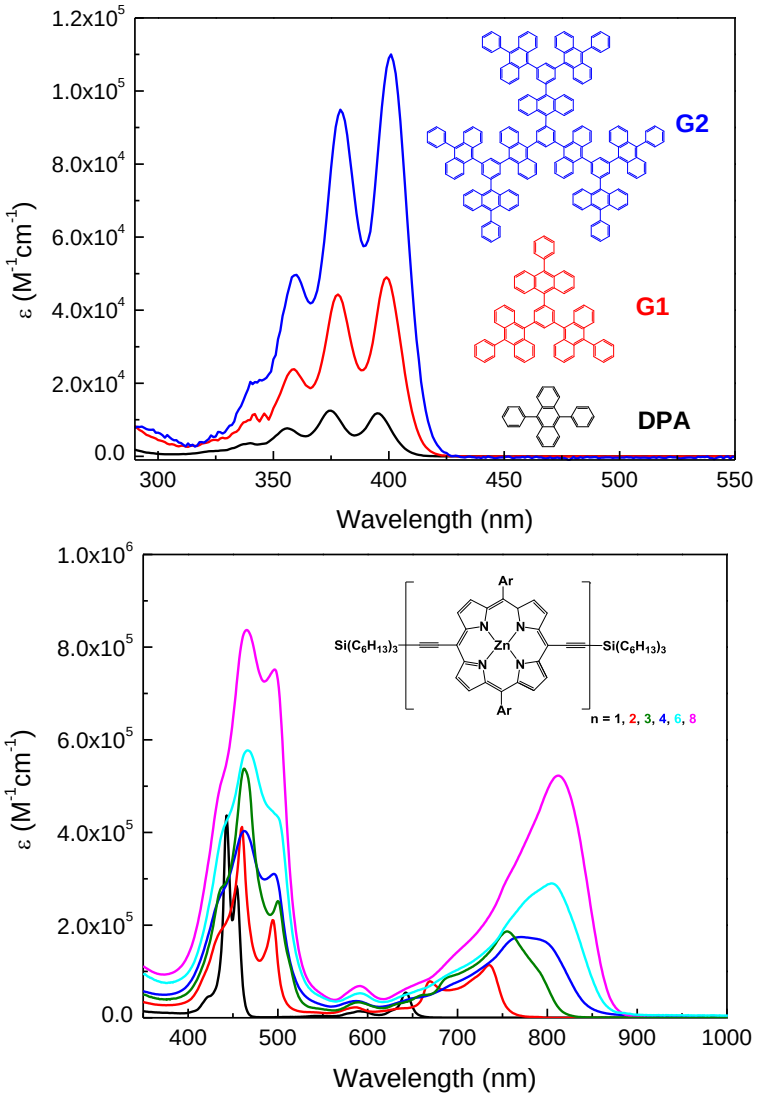

Figure 6.2 (top) Ground–state absorptivities of diphenylanthracene **DPA** (black) and the anthracene dendrimers **G1** (red) and **G2** (blue) in toluene. (bottom) Ground–state absorptivities of the butadiyne–linked porphyrin oligomers $\mathbf{P_n}$ in chloroform with 1% pyridine added: $\mathbf{P_1}$ (black), $\mathbf{P_2}$ (red), $\mathbf{P_3}$ (green), $\mathbf{P_4}$ (blue), $\mathbf{P_6}$ (cyan) and $\mathbf{P_8}$ (magenta).

The ground–state absorption spectra of **G1** and **G2** are similar to the one of DPA and show a linear increase of the molar absorption from **DPA** to **G1** to **G2**. Only minor changes in the ratio of the intensities of the vibronic peaks may be distinguished. In contrast, the ground–state absorption spectra of $\mathbf{P_n}$ (n > 1) clearly do not resemble the one of the monomer. When going from $\mathbf{P_1}$ to $\mathbf{P_8}$, the spectra are markedly altered especially in the lowest absorption band (i.e. the Q–band). The Q–band progressively red–shifts as the number of porphyrin moieties increases. In the Soret–band, further spectral splitting over the 400–500 nm wavelength region is observed. From the presence or absence of these spectral changes, one can already see a clear difference in the strength of the inter–chromophore coupling in the $\mathbf{P_n}$ systems and in the **G1** and **G2** dendrimers. In the $\mathbf{P_n}$ systems, the inter–chromophore coupling seems sufficiently strong that the multiporphyrin systems behave as new chromophores with their own spectral features (i.e. different from the sum of the individual porphyrins). Instead, for

G1 and **G2** dendrimers, their ground–state absorption spectra are a simple addition of the absorption spectra of the individual **DPA** moieties. To go further, it is useful to take a closer look at the linkage topology in these two systems. In the case of **G1** and **G2**, the anthracene moieties are connected to each other using phenyl linkers. Due to steric constraints with the anthracene groups, these phenyl linkers impose relatively large dihedral angles between the **DPA** moieties.[206] Such large dihedral angles disrupt the π–conjugation within the dendrimer structure. This results in a weak through–bond electronic coupling between the individual **DPA** moieties in **G1** and **G2**, hence the observed monomer–like absorption spectra of **G1** and **G2**. One may refer to them as weakly conjugated multichromophoric systems. In contrast, the butadiyne–linked porphyrin oligomers, or at least the planar conformers, are strongly conjugated systems. With the use of alkyne linkers such as butadiyne in $\mathbf{P_n}$, the coplanar arrangement of neighboring porphyrin macrocycles is possible and allows for significant π–overlap between neighboring porphyrins. The increased size of the conjugated system leads to a gradual red–shift of the Q–band with the length of the oligomer as observed in Figure 6.2. Thus, the strong inter–chromophore coupling in the $\mathbf{P_n}$ systems mainly arises in the ground state from electronic delocalization. Note that as discussed in chapter 5, the spectrally broad Q–band observed for $\mathbf{P_n}$ ($n \geq 2$) also arises from the use of butadiyne linkers that allow for nearly barrierless rotation of individual porphyrin macrocycles in and out of the plane at room temperature.

Another manifestation of electronic delocalization in multichromophoric systems is the reduction of the HOMO–LUMO gap with the increasing size of the system which can be estimated from the experimental $E_{0–0}$ energy of the lowest electronic transition.[111] For the porphyrin oligomers, $E_{0–0}$ decreases from 1.9 eV for $\mathbf{P_1}$ to 1.5 eV for $\mathbf{P_8}$ due mainly to an enhanced stabilization of the excited state as the oligomers adopt on average a more planar conformation than in the ground–state.[137-138] In contrast for the dendrimers, minor changes in the $E_{0–0}$ values are observed indicating that electronic delocalization in these systems is negligible: $E_{0–0}$ = 3.09 eV for **DPA**, $E_{0–0}$ = 3.06 eV for **G1** and $E_{0–0}$ = 3.04 eV for **G2**.

Thus, steady–state absorption and emission reveal that the $\mathbf{P_n}$ systems already in the ground state show signs of strong electronic coupling and behave as new chromophores, while in the anthracene dendrimers **G1** and **G2**, the spectroscopic individuality of the monomeric units is retained. However, is it also the case in the excited state? To get a partial answer, it is interesting to look at the radiative rate constants, k_f, of the dendrimers (see Table 6.1). When going from **DPA** to **G1** to **G2**, k_f increases quite substantially, suggesting a more collective emission behavior of the DPA moieties, i.e. exciton coupling within the dendrimer structure.[207]

Table 6.1 Fluorescence quantum yields (Φ_f),[a] lifetimes (τ)[b] and corresponding radiative rate constants (k_f) of DPA and the dendrimers G1 and G2 in argon–purged toluene

	Φ_f	τ (ns)	k_f (s^{-1})
DPA	1.02[c]	7.0	$1.4 \cdot 10^8$
G1	1.03[c]	5.3	$1.9 \cdot 10^8$
G2	0.99	4.5	$2.2 \cdot 10^8$

[a]Fluorescence quantum yields were determined using **DPA** in cyclohexane as reference (Φ_f = 0.97) with λ_{exc} = 354 nm.[208] [b]The lifetimes were measured using a TCSPC set up. The excitation wavelength was 385 nm and photons were collected at 430 nm. [c]The quantum yields for **DPA** and **G1** appear to exceed unity but this is a mere effect of the real quantum yield being very close to unity in combination with minor measurement fluctuations.

6.3 RESOLVING EXCITATION ENERGY TRANSFER IN ANTHRACENE DENDRIMERS AND PORPHYRINS OLIGOMERS

The following sections aim at answering the question of how localized or delocalized (i.e. distributed over multiple chromophores) excitation energy is in the anthracene dendrimers and the butadiyne–linked porphyrin oligomers.

6.3.1 FLUORESCENCE ANISOTROPY AS A PROBE FOR ENERGY MIGRATION IN ANTHRACENE DENDRIMERS

For the anthracene dendrimers **G1** and **G2**, exciton coupling becomes apparent through fluorescence anisotropy. We measured the temperature–dependent steady–state fluorescence excitation anisotropy spectra of **G1** and **G2** and the reference **DPA** (Figure 6.3). At 100 K, the fluorescence anisotropy of **DPA** reaches, as reported previously, a maximum anisotropy close to 0.4 at the red–edge of the absorption, indicating nearly collinear absorption and emission transition dipole moments.[209] At the same temperature, the fluorescence anisotropy spectra of **G1** and **G2** are much more surprising (and interesting) and show oscillations with maxima off resonance with the vibronic peaks of the absorption band. This oscillatory behavior is also accompanied by a decrease of the anisotropy in **G1** and **G2** compared to **DPA**.

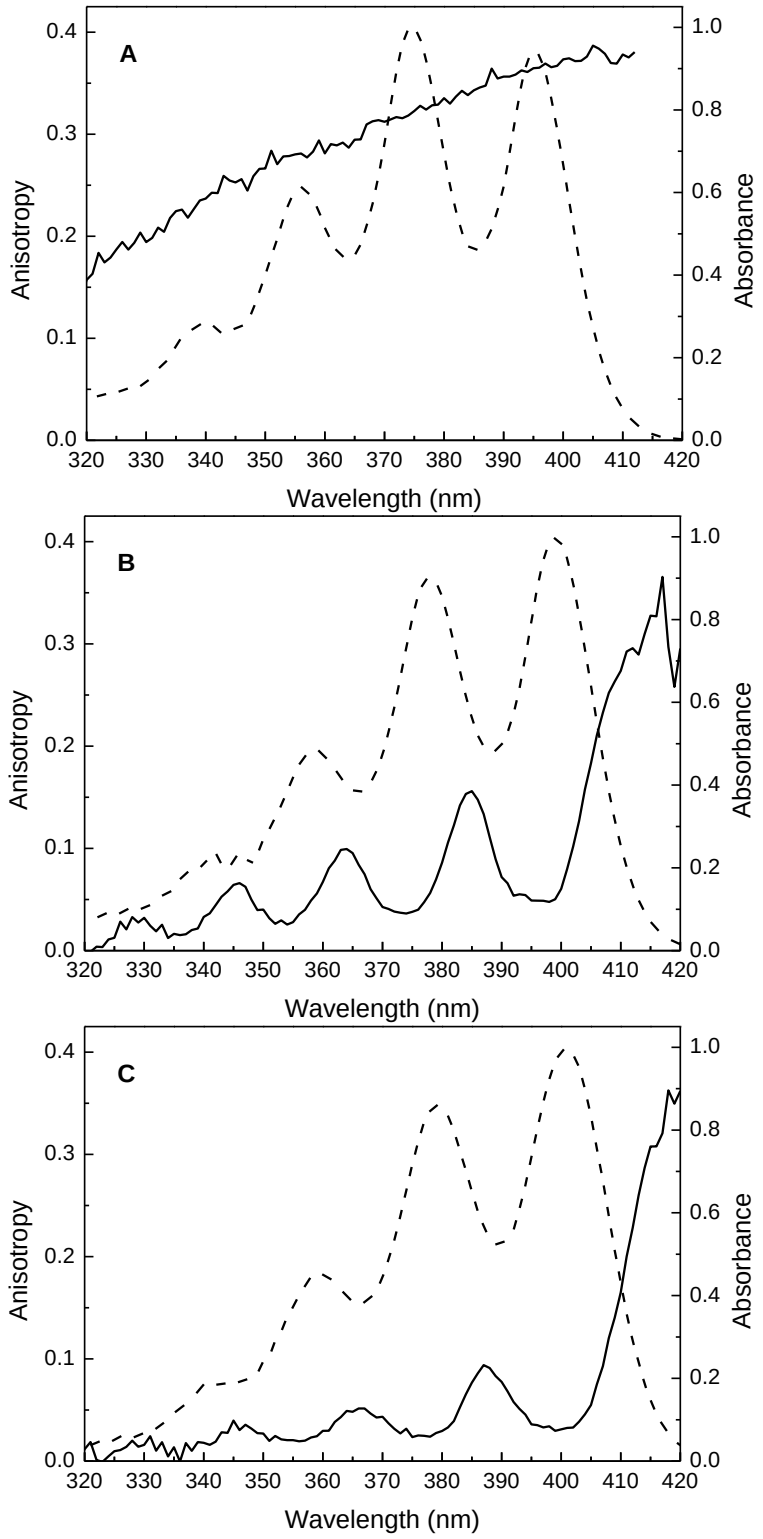

Figure 6.3 Steady–state fluorescence excitation anisotropy (solid lines) and absorption spectra (dashed lines) of (A) **DPA**, (B) **G1** and (C) **G2** in 2–MTHF at 100 K. The emission wavelength was 415 nm for **DPA** and 430 nm for **G1** and **G2**.

Such oscillations in **G1** and **G2** fluorescence anisotropy are clearly not consistent with an excited state localized on a single **DPA** unit that would have, as reported for **DPA**, an emission dipole moment along the phenyls direction (Figure 6.3).[206] However, if one considers a fully delocalized exciton model, taking **G1** as an example, this consists in

assigning a transition dipole moment along the phenyls direction to each **DPA** moiety (Figure 6.4). The overall transition moment is then given by the sum of the individual transition dipole moments. Three combinations of the individual transition dipole moments can be envisaged that lead to only two allowed transitions from the ground state ($\vec{\mu}_{fi} \neq 0$). These allowed transitions are lower in energy and perpendicular to each other in a system with threefold symmetry. Thus the excited state in **G1** splits into 3 new levels: one above forbidden state E' and two degenerate states E'' and E''' below the excited state energy level of three separate **DPA** units (Figure 6.4).

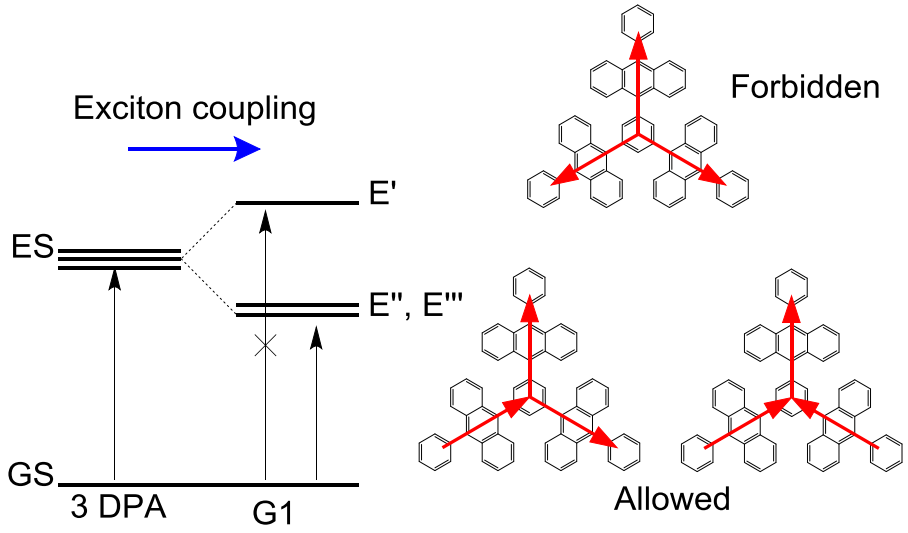

Figure 6.4 Exciton band energy diagram for **G1** in the case of the fully delocalized exciton model.

By considering such a fully delocalized exciton model and assuming that one of the two perpendicular transitions as a limiting anisotropy of 0.3 (i.e. the maximum value observed at the red–edge of the absorption band), one can calculate according to equation 4.9 that the other perpendicular transition has a limiting anisotropy of – 0.15. Since anisotropy follows an additive law, it is then possible to resolve the absorption spectra corresponding to the transition from the ground–state to each of these exciton states E'' and E''' using the excitation anisotropy spectrum of **G1**.[210] The resolved absorption spectra for GS → E'' and GS → E''' transitions are shown in Figure 6.5 along with the absorption spectrum of **G1**.

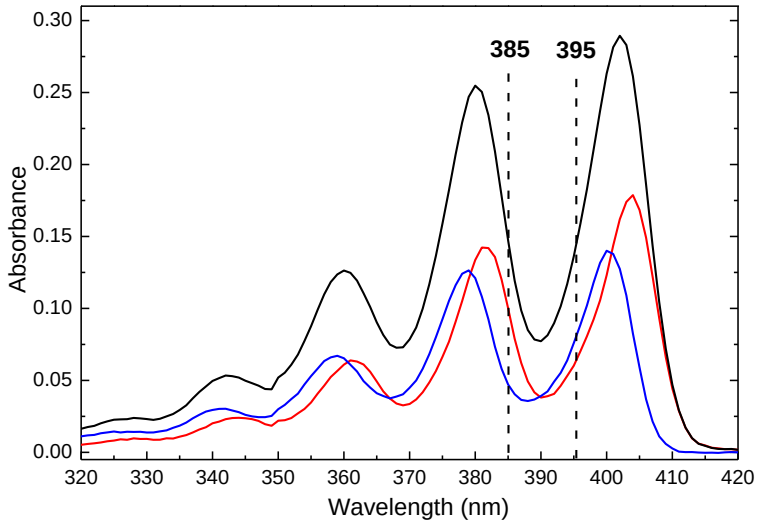

Figure 6.5 Resolved absorption spectra for the transitions GS → E'' and GS → E''' (blue and red). Also shown in black is the absorption spectrum of **G1** at 100 K. The dashed lines indicate the excitation wavelengths chosen for time–resolved anisotropy measurements (*vide infra*).

As seen in Figure 6.5, degeneracy of the lower exciton states (ΔE = 250 cm^{-1}) relaxes due to static and dynamic distortions of the dendrimer geometry. This gives rise to a lower excited state (in red) with high anisotropy (r_0 = 0.30) and a higher excited state (in blue) with low anisotropy (r_0 = – 0.15). Thus, from the resolved absorption spectra, we could successfully explain the oscillating behavior of anisotropy by two nearly degenerate perpendicular transitions, in agreement with a delocalized exciton model. For **G2**, given its similar absorption spectrum to **G1**, the same explanation for the anisotropy oscillations can be proposed, although a more complex exciton structure can be expected since more **DPA** moieties are involved.

The excitation wavelength–dependent fluorescence anisotropy decays further support the presence of two nearly degenerate exciton states with respective populations closely related. Excitation wavelengths λ_{exc} = 385 nm and λ_{exc} = 395 nm were selected approximately in resonance with a local max and min of the excitation anisotropy, respectively (Figure 6.3B). These excitation wavelengths initially populate different excited states. At λ_{exc} = 385 nm, the lowest excited state with high anisotropy is populated, whereas at λ_{exc} = 395 nm, the higher excited state with low anisotropy is predominantly occupied. When measured at room temperature, the fluorescence anisotropies decay mono–exponentially at all excitation wavelengths with as expected increasing correlation times from **DPA** to **G1** to **G2** assigned to rotational motions of the chromophores. However, at 160 K and at 140 K, **G1** exhibits much more interesting excitation wavelength–dependent fluorescence anisotropy decays that needed a bi–exponential fit (Figure 6.6). The anisotropy decays measured at λ_{exc} = 385 nm show an initial fast decay whereas the anisotropy decays measured at λ_{exc} = 395 nm display a corresponding rise time, and a subsequent slow decay as for λ_{exc} = 385 nm.

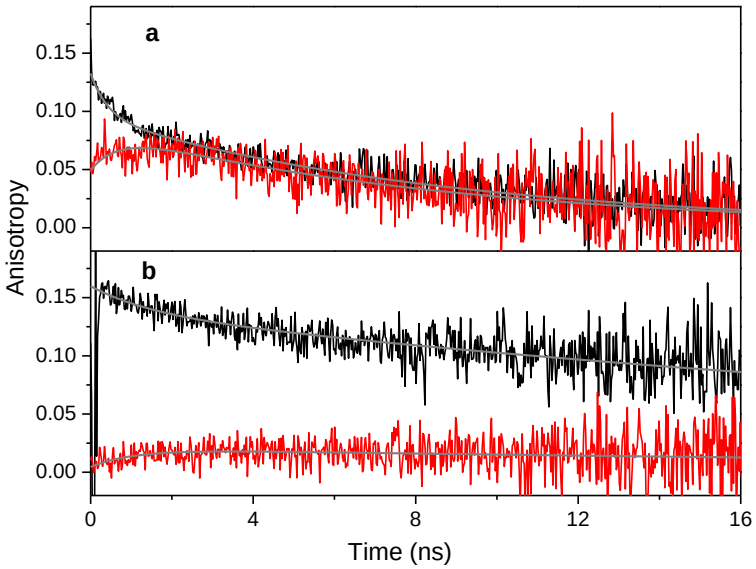

Figure 6.6 Fluorescence anisotropy decays of **G1** in 2–MTHF excited at 385 nm (black) and at 395 nm (red) at (a) 160 K and (b) 140 K. The emission wavelength was 430 nm. The solid gray lines represent the fits to bi–exponential functions $r(t) = r_{0,a}e^{-t/\theta_a} + r_{0,b}e^{-t/\theta_b}$.

For both excitation wavelengths, the long correlation time is 8.6 ns and 34 ns, at 160 K and at 140 K, respectively and agrees well with estimated values for rotational motions of **G1** at these temperatures (Table 6.2). The short correlation time is nearly the same for both excitation wavelengths, i.e. approximately 0.5 ns at 160 K and > 1 ns at 140 K. These short correlation times are, however, quite long compared to the times expected for internal conversion (few ps or less) or incoherent energy transfer processes ($\tau_{EET} \sim$ 100 fs estimated from the FRET model). Instead, we believe that this short correlation time is the time to reach thermal equilibrium of the two emitting states E'' and E'''. The low temperature conditions and one of the reactions being uphill in energy may explain such slow relaxation dynamics. At lower temperatures (100 K and 80 K), the upward reaction becomes too slow to be observed during the lifetime of the excited state. Hence, at these temperatures, as the excitation wavelength is varied, the proportion of high energy (low anisotropy) and low energy (high anisotropy) emitting states populated varies as well and so does the anisotropy, leading to its oscillatory behavior in the steady–state spectra (Figure 6.3).

Table 6.2 Fitted fluorescence anisotropy decay parameters for G1 as a function of temperature and excitation wavelength

T(K)	λ_{exc} (nm)	$r_{0,a}$	θ_a(ns)	$r_{0,b}$	θ_b(ns)	χ^2	θ_{calc}(ns)*
160	385	0.04	0.42	0.09	8.6	1.516	5.8
	395	–0.04	0.66	0.09	8.6	0.879	5.8
140	385	0.02	1.5	0.14	34	1.187	32.8
	395	–0.02	1.04	0.02	34	0.973	32.8

*The rotational correlation time θ_{calc} was estimated using the equation $\theta_{calc}=\eta V/k_B T$ where η is the viscosity of 2–MTHF at the temperature T, V is the volume of the rotating fluorophore[211] and k_B is the Boltzmann constant. For **G1**, the volume of the rotating fluorophore is assumed to scale linearly with the molecular mass, taking the molecular mass of **DPA** as a reference.

Finally, judging from the decrease of the r_0 values (i.e. $r_{0,a} + r_{0,b}$) for **G1** and **G2** compared to **DPA** (r_0 = 0.34 at 160 K and r_0 = 0.36 at 140 K in Paper IV supporting information Table S2), one can assumed the presence of an additional ultrafast depolarization channel in **G1** and **G2**, i.e. excitation energy migration among the **DPA** moieties. However, on the time scale of our experiments (time resolution of 10 ps), the excitation energy distributes immediately within the dendrimer structure.

6.3.2 SINGLET–SINGLET ANNIHILATION AS A PROBE FOR ENERGY MIGRATION IN PORPHYRIN OLIGOMERS

In the $\mathbf{P_n}$ systems, the signs of strong electronic coupling in the ground and excited states (*vide supra*) leave us to predict an ultrafast delocalization of the exciton over the oligomer chain. However, pump intensity–dependent transient absorption measurements performed on the entire series give a slightly different picture with signs of an, at least, partially localized exciton at early times (t < 30 ps). Figure 6.7 shows the intensity–dependent transient absorption time profiles of $\mathbf{P_2}$ and $\mathbf{P_4}$ probed at 540 nm where the transient absorption (TA) signal solely arises from the porphyrin excited states, $^1\mathbf{P_2}^*$ and $^1\mathbf{P_4}^*$.

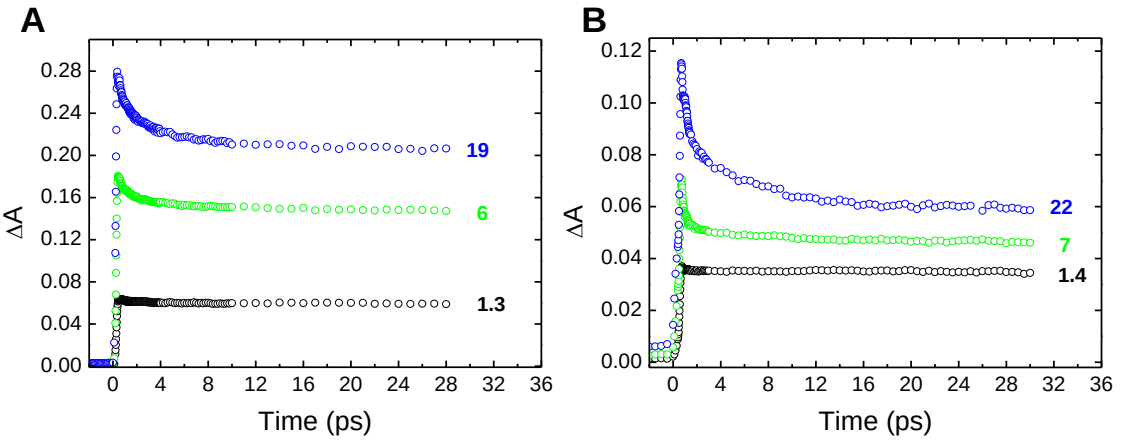

Figure 6.7 Intensity–dependent transient absorption time profiles of (A) $\mathbf{P_2}$ and (B) $\mathbf{P_4}$ probed at 540 nm. The pump intensities *x* x 10^{29} photons/cm^2/s are indicated next to the respective decays. The excitation wavelength was 670 nm for $\mathbf{P_2}$ and 800 nm for $\mathbf{P_4}$.

Both $\mathbf{P_2}$ and $\mathbf{P_4}$ exhibit non–exponential TA–decays with intensity–dependent amplitudes and lifetimes. At low pump intensity, the TA signals remain constant over the first 30 ps following photo–excitation in accord with their much longer singlet excited state lifetimes, i.e. $\tau(^1\mathbf{P_2}^*)$ = 1210 ps and $\tau(^1\mathbf{P_4}^*)$ = 830 ps.[195] However, at higher pump intensity, short intensity–dependent lifetimes precede the natural decay of $^1\mathbf{P_2}^*$ and $^1\mathbf{P_4}^*$. Such pump intensity dependence of the TA signals is observed for all porphyrin oligomers containing more than one porphyrin unit (see Paper V supporting information Figures S1–S3). In contrast for the monomer, this is not seen. The transient signal of $^1\mathbf{P_1}^*$ remains constant over the first 30 ps (see Paper V Figure 3) as expected by its long lifetime (i.e. $\tau(^1\mathbf{P_1}^*)$ = 1450 ps). In the long oligomers (n ≥ 2), we explain this pump intensity dependence of the transient absorption by the presence of singlet–singlet annihilation reactions preceding the natural decay of their excited states. Indeed, at high pump intensity, it becomes possible in the long oligomers to excite simultaneously two or more porphyrin units. This leads to the following excited state reaction applied to the dimer for simplicity:

$$^1P^*–^1P^* \xrightarrow{annihilation} {}^1P^{**}–P \xrightarrow{fast\ non-radiative\ relaxation} {}^1P^*–P \xrightarrow{normal\ decay} P–P \qquad 6.1$$

where $^1P^{**}$ designates a porphyrin unit in a higher singlet excited state. At first, the singlet–singlet annihilation is quite surprising given the strong though–bond electronic communication that exists in the $\mathbf{P_n}$ systems. It implies that there is in these systems either a disruption of the π–conjugation or sufficient structural disorder to enable a temporary localization of the exciton states. The singlet–singlet annihilation is further supported by the increasing contribution of the short lifetime to the overall transient decay with increasing pump intensity.

In order to assess the oligomer size effect on the singlet–singlet annihilation reaction, it is interesting to compare the normalized intensity–dependent TA decays obtained for the entire series at approximately identical pump intensity (Figure 6.8). Upon

lengthening of the oligomer, the contribution of the short lifetime to the overall transient absorption decay increases. This may be explained by the higher probability of multiple excitations in the longer oligomers but also more conformational heterogeneity. Indeed, conformational heterogeneity varies significantly when going from the dimer to the octamer. In particular, these measurements were carried using 800 nm as pump excitation wavelength for $\mathbf{P_n}$ ($n \geq 3$). This promotes different populations of conformers to the excited state. For $\mathbf{P_3}$, this creates a more planar excited state while in $\mathbf{P_8}$, more twisted conformations of the oligomer chain are excited. Such conformational effects render the picture even more complex. In particular, any attempt of full modeling of the excitation migration in these oligomers remains difficult. These transient absorption measurements do not provide a way to estimate the location of the exciton neither their distribution along the oligomer chain that may significantly vary with the oligomer size and its conformation.

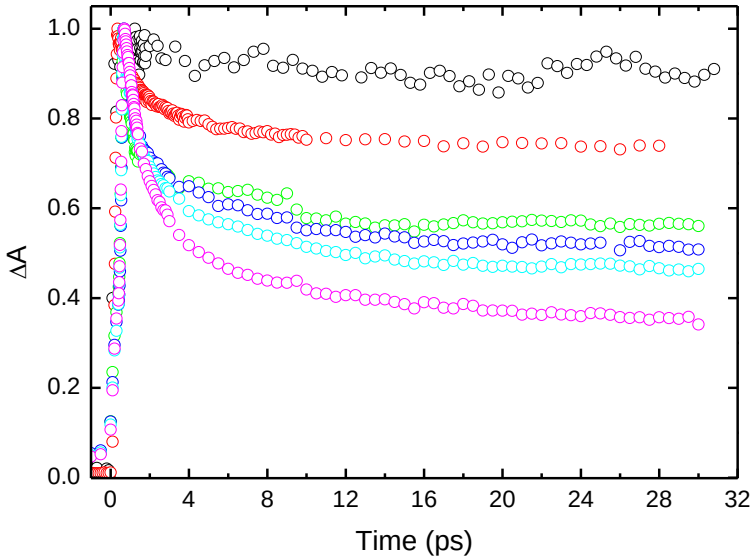

Figure 6.8 Normalized intensity–dependent transient absorption time profiles of the entire series: $\mathbf{P_1}$ (black), $\mathbf{P_2}$ (red), $\mathbf{P_3}$ (green), $\mathbf{P_4}$ (blue), $\mathbf{P_6}$ (cyan) and $\mathbf{P_8}$ (magenta) probed at 540 nm. The excitation intensities was 18 x 10^{29} photons/cm^2/s for $\mathbf{P_1}$, 19 x 10^{29} photons/cm^2/s for $\mathbf{P_2}$ and 22 x 10^{29} photons/cm^2/s for $\mathbf{P_n}$ (n = 3, 4, 6, 8).

In an attempt to probe conformational effects on the singlet–singlet annihilation reaction, we measured the pump intensity dependence of the TA signal of a template–bound hexamer ring of $\mathbf{P_{6R}}$**:T6** that consists of a porphyrin hexamer ring $\mathbf{P_{6R}}$ hold by a hexapyridyl ligand **T6** (Figure 6.9). In this complex, the template **T6** provides a means to structurally constrain adjacent porphyrins into a close–to–planar arrangement. Figure 6.9 compares the normalized pump intensity–dependent TA decays of $\mathbf{P_6}$ and $\mathbf{P_{6R}}$**:T6** probed at 540 nm following photo–excitation of the porphyrin hexamer at 800 nm. At all pump intensities, $\mathbf{P_{6R}}$**:T6** exhibits a short lifetime sign of singlet–singlet annihilation preceding its natural decay ($\tau(^1\mathbf{P_{6R}}^*$**:T6)** = 340 ps).[203] Surprisingly, the more planar arrangement of the neighboring porphyrins in $\mathbf{P_{6R}}$**:T6** do not induce a full delocalization of the exciton. We note that the short lifetime contribution to the overall decay in $\mathbf{P_{6R}}$**:T6** seems reduced compared to the linear

hexamer. However, this may be due to experimental limitations. The time resolution of these experiments (~100 fs) may not be sufficient to resolve the entire fast decay. Nevertheless, these experiments provide first evidence of a localization of the exciton at early times (< 30 ps) in linear and circular strongly conjugated butadiyne–linked porphyrin oligomers.

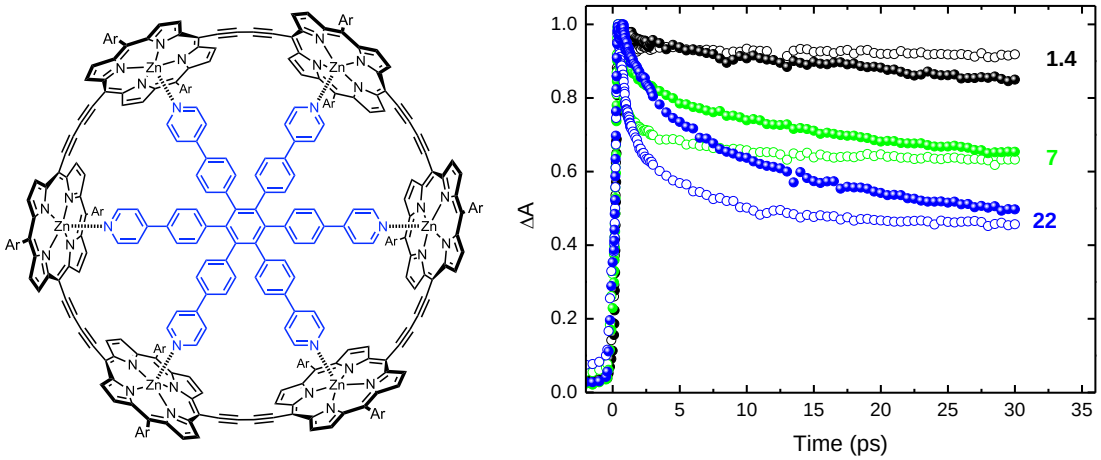

Figure 6.9 Normalized Intensity–dependent transient absorption time profiles of **P_{6R}:T6** (●) and **P_6** (○) probed at 540 nm. The excitation intensities *x* x 10^{29} photons/cm^2/s are indicated next to the respective decays. The excitation wavelength was 800 nm.

6.3.3 Concluding remarks

The comparison of the anthracene dendrimers and the porphyrin linear oligomers reveals significantly different behaviors in term of inter–chromophore communication. In the anthracene dendrimers, in the ground state, **DPA** moieties behave as localized chromophores in the absence of the others. However, in the excited state, evidence of a fast delocalization of the exciton over the entire dendrimer structure is revealed by steady–state and time–resolved fluorescence anisotropy. In contrast, the porphyrin linear oligomers, already in the ground state, form a new chromophore with absorption spectra that due to electronic delocalization strongly differ from the one of the monomer unit. Nevertheless, pump intensity–dependent transient absorption experiments reveal that the individuality of the porphyrin subunit is, in part, retained at early times (> 30 ps) despite the strong electronic coupling.

7 CONCLUSION

In this Thesis, the butadiyne–linked zinc porphyrin oligomers $\mathbf{P_n}$ are versatile model systems that can be used to investigate both photoinduced energy transfer and electron transfer when incorporating in a donor–acceptor couple.

In electron transfer studies (Chapter 5), appending to the $\mathbf{P_n}$ systems (n = 1–4, 6) a ferrocene–fullerene donor–acceptor couple led to the formation of a series of $\mathbf{Fc–P_n–C_{60}}$ D–B–A triads. In these triads, the formation and recombination of the long–range charge separated state $\mathbf{Fc^{\bullet+}–P_n–C_{60}^{\bullet-}}$ generated upon photoexcitation of the porphyrin bridge was studied in detail. The temperature dependence of both its formation and decay probed by combining time–resolved fluorescence and transient absorption experiments provided mechanistic details of the electron transfer in these triads. In particular, we could relate the weakly distance–dependent charge recombination of $\mathbf{Fc^{\bullet+}–P_n–C_{60}^{\bullet-}}$ ($\beta = 0.028$ Å^{-1} at 300 K) to recombination to the ground state via coherent electron tunneling for the entire series. However, at lower temperature, the temperature dependence of the recombination rates revealed an unusual switch in charge transport mechanism from coherent electron tunneling to incoherent hopping in the long triads ($n \geq 2$). Such crossover was evidenced by recombination rates that strongly deviated from the Marcus description with a single set of parameters (ΔG^0, λ, V) and was rationalized by the long lifetimes of the charge separated state that push charge transport into the hopping regime. Overall, the implication of this work is that there is not a single *modus operandi* by which wire–like charge transport may be achieved in highly conjugated systems. [87, 212]

Another aspect investigated in detail is the influence that the conformation of the photoexcited porphyrin oligomer has on the charge separation process in long dyads $\mathbf{P_n–C_{60}}$ (n = 4, 6). In contrast to the previous study, this study can be placed in a more practical context where primary requirement is the control of signal transmission (here electron transfer). By probing the excitation wavelength dependence of the charge separation process in $\mathbf{P_n–C_{60}}$ (n = 4, 6), we showed that exciting twisted conformations led to significantly faster charge separation than excitation of the more planar conformers. Such optical gating of the charge separation could be explained, in part, by differences in driving forces. In addition, we showed that changing the geometry of the porphyrin oligomer from a linear to a semi–circular dyad by ligand coordination nearly shut down the electron transfer between the porphyrin photoexcited state and the fullerene, due to a considerably reduced driving force for charge separation in the semi–circular complexes. This result could be used to create a simple switch device. A potential improvement could be the optical control of the assembly and disassembly of these semi–circular complexes using a photoactive ligand instead.[47] We also demonstrated that temperature could be a simple means to control the conformation of the porphyrin systems. Lowering the temperature induced the reversible self–assembly of the $\mathbf{P_n}$, $\mathbf{P_n–C_{60}}$ and $\mathbf{Fc–P_n–C_{60}}$ systems into planar dimeric arrays. In these dimeric systems, several questions arise that could be the subject of follow–up studies: how strong is the intermolecular communication between the monomers within the stack? Is electron transfer in stack of $\mathbf{P_n–C_{60}}$ as efficient as in the free $\mathbf{P_n–C_{60}}$?

The last part of the Thesis (Chapter 6) has been focused on establishing the relationship between the electronic structure and the photophysical properties in two multichromophore systems: the $\mathbf{P_n}$ systems and the anthracene dendrimers **G1** and **G2**. In both systems, we demonstrated that the linker topology strongly influenced their photophysical properties. In the anthracene dendrimers, collective analysis of their steady–state absorption and emission revealed an apparent conservation of the individuality of the chromophores. However, excited state dynamics probed by steady-state and time-resolved fluorescence anisotropy showed a rather different behavior of the chromophores in the excited state. In the excited states, the anthracene dendrimers can be viewed as single chromophores due to fast delocalization of the exciton within the dendrimer structure. In contrast, in the $\mathbf{P_n}$ systems, pump intensity–dependent transient absorption measurements provided strong indication of singlet–singlet exciton–exciton annihilation reactions in the multiporphyrin systems. This was interpreted as a partial coupling of the porphyrin subunits in the excited state. In addition, qualitative comparison of the pump intensity dependent transient decays of the linear hexamer $\mathbf{P_6}$ and the template–bound hexamer ring $\mathbf{P_{6R}}$**:T6** suggested that the backbone conformation of the oligomer chain influenced the rate and the occurrence of the singlet–singlet annihilation reaction. In the future, complementary experiments could include fluorescence–up conversion anisotropy or singlet–singlet annihilation measurements in the anthracene dendrimers to probe the early times ($t < 10$ ps) following photon absorption while in the $\mathbf{P_n}$ systems, varying the pump wavelength at which the pump intensity dependent transient absorption decay is measured could provide more insights of the importance of conformation in the singlet–singlet annihilation reaction.

8 ACKNOWLEDGEMENTS

First of all, I would like to thank my supervisor Prof. Bo Albinsson. Thank you Bo! Thank you for your scientific guidance and your support. Thank you for your trust when I was working back home in Stockholm. Finally, I will never forget your favorite expression to me “Don’t worry”, making me panicking at times but put things into perspective at end.

I also want to thank Maria Abrahamsson my official co–supervisor and friend. Thank you for your tireless encouragement and always open door. I will not forget your support and help after my little curling accident on my second PhD week. Thank you for introducing me to your colleagues at Uppsala University. Next time, we should plan a home–made Indian–French dinner.

I would also like to thank the past and present “laser” people for the help in the laser labs: Joakim Kärnbratt, Jonas Hannestad, Joachim Hedberg, Damir Dzebo and Valeria Saavedra. To the present people, keep it up running!!

This thesis is also the result of close collaborations with different groups. I want to thank Harry Anderson and his group of organic chemists at Oxford University for synthesizing all porphyrin–based systems. Thanks to Karl Börjesson and Kasper Moth–Poulsen for the nice collaboration on the dendrimer project.

Thanks to my past and present officemates, Moa, Lena, Anke, Lulu, Tamas for the friendly and open–minded atmosphere in our office.

Special thanks to Anke for being a good friend, always there in bad and good times and opened for discussions about everything and nothing.

Thanks to all people at floor 5 for the great atmosphere.

Finally I would like to thank my parents and my brothers for their encouragement and support throughout the years. Big thanks to my husband, Hithesh, for often bringing me back down Earth, for all lunch boxes, including special deliveries at KTH library. I could not have made it without you. What is the next challenge?

9 REFERENCES

(1) *Key World Energy Statistics*; International Energy Agency: 2014.

(2) Hamblyn, R. *The Art of Science: A natural history of ideas*. Pan Macmillan: 2011.

(3) Arrhenius, S. On the Influence of Carbonic Acid in the Air upon the Temperature of the Ground. *Philos. Mag.* **1896**, *41*, 237-276.

(4) Statement of Dr. James Hansen, Director, NASA Goddard Institute for Space Studies. In *Committee on Energy and Natural Resources, U.S. Senate, 100th Congress*, US Government Printing Office: Washington D.C., 1988; pp 39-41.

(5) Shabecoff, P. Global Warming Has Begun, Expert Tells Senate. *New York Times* 24th June 1988, 1988.

(6) Green, M. A.; Emery, K.; Hishikawa, Y.; Warta, W.; Dunlop, E. D. Solar cell efficiency tables (Version 45). *Prog. Photovoltaics Res. Appl.* **2015**, *23*, 1-9.

(7) Hagfeldt, A.; Boschloo, G.; Sun, L.; Kloo, L.; Pettersson, H. Dye-Sensitized Solar Cells. *Chem. Rev.* **2010**, *110*, 6595-6663.

(8) Kloo, L. On the early development of organic dyes for dye-sensitized solar cells. *Chem. Commun.* **2013**, *49*, 6580-6583.

(9) Burschka, J.; Pellet, N.; Moon, S.-J.; Humphry-Baker, R.; Gao, P.; Nazeeruddin, M. K.; Gratzel, M. Sequential deposition as a route to high-performance perovskite-sensitized solar cells. *Nature* **2013**, *499*, 316-319.

(10) http://www.solarimpulse.com/ (accessed 17 March 2015).

(11) Barber, J. Photosynthetic energy conversion: natural and artificial. *Chem. Soc. Rev.* **2009**, *38*, 185-196.

(12) Ciamician, G. The Photochemistry of the Future. *Science* **1912**, *36*, 385-394.

(13) Blankenship, R. E. *Molecular mechanisms of photosynthesis*. John Wiley & Sons: 2013.

(14) van Grondelle, R.; Dekker, J. P.; Gillbro, T.; Sundstrom, V. Energy transfer and trapping in photosynthesis. *Biochimica et Biophysica Acta (BBA) - Bioenergetics* **1994**, *1187*, 1-65.

(15) Sundström, V.; Pullerits, T.; van Grondelle, R. Photosynthetic Light-Harvesting: Reconciling Dynamics and Structure of Purple Bacterial LH2 Reveals Function of Photosynthetic Unit. *J. Phys. Chem. B* **1999**, *103*, 2327-2346.

(16) Scholes, G. D.; Fleming, G. R.; Olaya-Castro, A.; van Grondelle, R. Lessons from nature about solar light harvesting. *Nature Chem.* **2011**, *3*, 763-774.

(17) Concepcion, J. J.; Jurss, J. W.; Brennaman, M. K.; Hoertz, P. G.; Patrocinio, A. O. T.; Murakami Iha, N. Y.; Templeton, J. L.; Meyer, T. J. Making Oxygen with Ruthenium Complexes. *Acc. Chem. Res.* **2009**, *42*, 1954-1965.

(18) Archer, S.; Weinstein, J. A. Charge-separated excited states in platinum(II) chromophores: Photophysics, formation, stabilization and utilization in solar energy conversion. *Coord. Chem. Rev.* **2012**, *256*, 2530-2561.

(19) Magnuson, A.; Anderlund, M.; Johansson, O.; Lindblad, P.; Lomoth, R.; Polivka, T.; Ott, S.; Stensjö, K.; Styring, S.; Sundström, V., et al. Biomimetic and Microbial Approaches to Solar Fuel Generation. *Acc. Chem. Res.* **2009**, *42*, 1899-1909.

(20) Frischmann, P. D.; Mahata, K.; Wurthner, F. Powering the future of molecular artificial photosynthesis with light-harvesting metallosupramolecular dye assemblies. *Chem. Soc. Rev.* **2013**, *42*, 1847-1870.

(21) Gust, D.; Moore, T. A.; Moore, A. L. Realizing Artificial Photosynthesis. *Faraday Discuss.* **2012**, *155*, 9-26.

(22) Guldi, D. M. Fullerene-porphyrin architectures; photosynthetic antenna and reaction center models. *Chem. Soc. Rev.* **2002**, *31*, 22-36.

(23) Gust, D.; Moore, T. A.; Moore, A. L.; Lee, S.-J.; Bittersmann, E.; Luttrull, D. K.; Rehms, A. A.; DeGraziano, J. M.; Ma, X. C.; Gao, F., et al. Efficient Multistep Photoinitiated Electron Transfer in a Molecular Pentad. *Science* **1990**, *248*, 199-201.

(24) Imahori, H.; Sekiguchi, Y.; Kashiwagi, Y.; Sato, T.; Araki, Y.; Ito, O.; Yamada, H.; Fukuzumi, S. Long-Lived Charge-Separated State Generated in a Ferrocene–meso,meso-Linked Porphyrin Trimer–Fullerene Pentad with a High Quantum Yield. *Chem. Eur. J.* **2004**, *10*, 3184-3196.

(25) Borgström, M.; Shaikh, N.; Johansson, O.; Anderlund, M. F.; Styring, S.; Åkermark, B.; Magnuson, A.; Hammarström, L. Light induced manganese oxidation and long-lived charge separation in a Mn-2(II,II)-Ru-II (bpy)(3)-acceptor triad. *J. Am. Chem. Soc.* **2005**, *127*, 17504-17515.

(26) Berardi, S.; La Ganga, G.; Natali, M.; Bazzan, I.; Puntoriero, F.; Sartorel, A.; Scandola, F.; Campagna, S.; Bonchio, M. Photocatalytic Water Oxidation: Tuning Light-Induced Electron Transfer by Molecular Co4O4 Cores. *J. Am. Chem. Soc.* **2012**, *134*, 11104-11107.

(27) Megiatto, J. D.; Antoniuk-Pablant, A.; Sherman, B. D.; Kodis, G.; Gervaldo, M.; Moore, T. A.; Moore, A. L.; Gust, D. Mimicking the electron transfer chain in photosystem II with a molecular triad thermodynamically capable of water oxidation. *Proc. Natl. Acad. Sci. U. S. A.* **2012**, *109*, 15578-15583.

(28) de la Torre, G.; Giacalone, F.; Segura, J. L.; Martin, N.; Guldi, D. M. Electronic Communication through pi-Conjugated Wires in Covalently Linked Porphyrin/C-60 Ensembles. *Chem. Eur. J.* **2005**, *11*, 1267-1280.

(29) Kilså, K.; Kajanus, J.; Macpherson, A. N.; Mårtensson, J.; Albinsson, B. Bridge-Dependent Electron Transfer in Porphyrin-Based Donor−Bridge−Acceptor Systems. *J. Am. Chem. Soc.* **2001**, *123*, 3069-3080.

(30) Petersson, J.; Eklund, M.; Davidsson, J.; Hammarström, L. Variation of Excitation Energy Influences the Product Distribution of a Two-Step Electron Transfer: S2 vs S1 Electron Transfer in a Zn(II)porphyrin−Viologen Complex. *J. Am. Chem. Soc.* **2009**, *131*, 7940-7941.

(31) Fathalla, M.; Barnes, J. C.; Young, R. M.; Hartlieb, K. J.; Dyar, S. M.; Eaton, S. W.; Sarjeant, A. A.; Co, D. T.; Wasielewski, M. R.; Stoddart, J. F. Photoinduced Electron Transfer within a Zinc Porphyrin–Cyclobis(paraquat-p-phenylene) Donor–Acceptor Dyad. *Chem. Eur. J.* **2014**, *20*, 14690-14697.

(32) Göransson, E.; Boixel, J.; Fortage, J.; Jacquemin, D.; Becker, H.-C.; Blart, E.; Hammarström, L.; Odobel, F. Long-Range Electron Transfer in Zinc-Phthalocyanine-Oligo(Phenylene-Ethynylene)-Based Donor-Bridge-Acceptor Dyads. *Inorg. Chem.* **2012**, *51*, 11500-11512.

(33) Weiss, E. A.; Ahrens, M. J.; Sinks, L. E.; Gusev, A. V.; Ratner, M. A.; Wasielewski, M. R. Making a Molecular Wire: Charge and Spin Transport through para-Phenylene Oligomers. *J. Am. Chem. Soc.* **2004**, *126*, 5577-5584.

(34) Goldsmith, R. H.; Sinks, L. E.; Kelley, R. F.; Betzen, L. J.; Liu, W. H.; Weiss, E. A.; Ratner, M. A.; Wasielewski, M. R. Wire-Like Charge Transport at near Constant Bridge Energy through Fluorene Oligomers. *Proc. Natl. Acad. Sci. U. S. A.* **2005**, *102*, 3540-3545.

(35) Scattergood, P. A.; Delor, M.; Sazanovich, I. V.; Bouganov, O. V.; Tikhomirov, S. A.; Stasheuski, A. S.; Parker, A. W.; Greetham, G. M.; Towrie, M.; Davies, E. S., et al. Electron transfer dynamics and excited state branching in a charge-transfer platinum(ii) donor-bridge-acceptor assembly. *Dalton Trans.* **2014**, *43*, 17677-17693.

(36) Sazanovich, I. V.; Best, J.; Scattergood, P. A.; Towrie, M.; Tikhomirov, S. A.; Bouganov, O. V.; Meijer, A. J. H. M.; Weinstein, J. A. Ultrafast photoinduced charge transport in Pt(ii) donor-acceptor assembly bearing naphthalimide electron acceptor and phenothiazine electron donor. *Phys. Chem. Chem. Phys.* **2014**, *16*, 25775-25788.

(37) Hanss, D.; Walther, M. E.; Wenger, O. S. Importance of covalence, conformational effects and tunneling-barrier heights for long-range electron transfer: Insights from dyads with oligo-p-phenylene, oligo-p-xylene and oligo-p-dimethoxybenzene bridges. *Coord. Chem. Rev.* **2010**, *254*, 2584-2592.

(38) Imahori, H.; Sakata, Y. Fullerenes as Novel Acceptors in Photosynthetic Electron Transfer. *Eur. J. Org. Chem.* **1999**, *1999*, 2445-2457.

(39) Giacalone, F.; Segura, J. L.; Martín, N.; Guldi, D. M. Exceptionally Small Attenuation Factors in Molecular Wires. *J. Am. Chem. Soc.* **2004**, *126*, 5340-5341.

(40) Atienza, C.; Martin, N.; Wielopolski, M.; Haworth, N.; Clark, T.; Guldi, D. M. Tuning electron transfer through p-phenyleneethynylene molecular wires. *Chem. Commun.* **2006**, 3202-3204.

(41) D'Souza, F.; Ito, O. Supramolecular donor-acceptor hybrids of porphyrins/phthalocyanines with fullerenes/carbon nanotubes: electron transfer, sensing, switching, and catalytic applications. *Chem. Commun.* **2009**, 4913-4928.

(42) Bandi, V.; Das, S. K.; Awuah, S. G.; You, Y.; D'Souza, F. Thieno-Pyrrole-Fused 4,4-Difluoro-4-bora-3a,4a-diaza-s-indacene–Fullerene Dyads: Utilization of Near-Infrared Sensitizers for Ultrafast Charge Separation in Donor–Acceptor Systems. *J. Am. Chem. Soc.* **2014**, *136*, 7571-7574.

(43) Wojcik, A.; Kamat, P. V. Reduced Graphene Oxide and Porphyrin. An Interactive Affair in 2-D. *ACS Nano* **2010**, *4*, 6697-6706.

(44) Guldi, D. M.; Sgobba, V. Carbon nanostructures for solar energy conversion schemes. *Chem. Commun.* **2011**, *47*, 606-610.

(45) Leary, E.; La Rosa, A.; Gonzalez, M. T.; Rubio-Bollinger, G.; Agrait, N.; Martin, N. Incorporating single molecules into electrical circuits. The role of the chemical anchoring group. *Chem. Soc. Rev.* **2015**, *44*, 920-942.

(46) Perrin, M. L.; Burzuri, E.; van der Zant, H. S. J. Single-molecule transistors. *Chem. Soc. Rev.* **2015**, *44*, 902-919.

(47) Kärnbratt, J.; Hammarson, M.; Li, S.; Anderson, H. L.; Albinsson, B.; Andréasson, J. Photochromic Supramolecular Memory With Nondestructive Readout. *Angew. Chem. Int. Ed.* **2010**, *49*, 1854-1857.

(48) Franco, I.; George, C. B.; Solomon, G. C.; Schatz, G. C.; Ratner, M. A. Mechanically Activated Molecular Switch through Single-Molecule Pulling. *J. Am. Chem. Soc.* **2011**, *133*, 2242-2249.

(49) Aviram, A.; Ratner, M. A. Molecular rectifiers. *Chem. Phys. Lett.* **1974**, *29*, 277-283.

(50) Ball, P. Chemistry Meets Computing. *Nature* **2000**, *406*, 118-120.

(51) Balzani, V.; Credi, A.; Venturi, M. Molecular Logic Circuits. *ChemPhysChem* **2003**, *4*, 49-59.

(52) Balzani, V. Photochemical molecular devices. *Photochem. Photobiol. Sci.* **2003**, *2*, 459-476.

(53) Cheng, Y.-C.; Fleming, G. R. Dynamics of Light Harvesting in Photosynthesis. *Annu. Rev. Phys. Chem.* **2009**, *60*, 241-262.

(54) Tachibana, Y.; Vayssieres, L.; Durrant, J. R. Artificial photosynthesis for solar water-splitting. *Nature Photon.* **2012**, *6*, 511-518.

(55) Björn, L.; Papageorgiou, G.; Blankenship, R.; Govindjee. A viewpoint: Why chlorophyll a? *Photosynth. Res.* **2009**, *99*, 85-98.

(56) van Grondelle, R.; Novoderezhkin, V. I. Energy transfer in photosynthesis: experimental insights and quantitative models. *Phys. Chem. Chem. Phys.* **2006**, *8*, 793-807.

(57) Novoderezhkin, V. I.; van Grondelle, R. Physical origins and models of energy transfer in photosynthetic light-harvesting. *Phys. Chem. Chem. Phys.* **2010**, *12*, 7352-7365.

(58) Fassioli, F.; Olaya-Castro, A.; Scheuring, S.; Sturgis, J. N.; Johnson, N. F. Energy Transfer in Light-Adapted Photosynthetic Membranes: From Active to Saturated Photosynthesis. *Biophys. J.* **2009**, *97*, 2464-2473.

(59) Boekema, E. J.; Hankamer, B.; Bald, D.; Kruip, J.; Nield, J.; Boonstra, A. F.; Barber, J.; Rögner, M. Supramolecular structure of the photosystem II complex from green plants and cyanobacteria. *Proc. Natl. Acad. Sci. U. S. A.* **1995**, *92*, 175-179.

(60) Rhee, K. H.; Morris, E. P.; Barber, J.; Kuhlbrandt, W. Three-dimensional structure of photosystem II reaction centre at 8 Å resolution. *Nature* **1998**, *396*, 283-286.

(61) Nield, J.; Kruse, O.; Ruprecht, J.; da Fonseca, P.; Büchel, C.; Barber, J. 3D structure of chlamydomonas reinhardtii and synechococcus elongatus photosystem II complexes allow for comparison of their OEC organisation. *J. Biol. Chem.* **2000**.

(62) Zouni, A.; Witt, H.-T.; Kern, J.; Fromme, P.; Krauss, N.; Saenger, W.; Orth, P. Crystal structure of photosystem II from Synechococcus elongatus at 3.8 Å resolution. *Nature* **2001**, *409*, 739-743.

(63) Kamiya, N.; Shen, J.-R. Crystal structure of oxygen-evolving photosystem II from Thermosynechococcus vulcanus at 3.7 Å resolution. *Proc. Natl. Acad. Sci. U. S. A.* **2003**, *100*, 98-103.

(64) Biesiadka, J.; Loll, B.; Kern, J.; Irrgang, K.-D.; Zouni, A. Crystal structure of cyanobacterial photosystem II at 3.2 Å resolution: a closer look at the Mn-cluster. *Phys. Chem. Chem. Phys.* **2004**, *6*, 4733-4736.

(65) Loll, B.; Kern, J.; Saenger, W.; Zouni, A.; Biesiadka, J. Towards complete cofactor arrangement in the 3.0 Å resolution structure of photosystem II. *Nature* **2005**, *438*, 1040-1044.

(66) Guskov, A.; Kern, J.; Gabdulkhakov, A.; Broser, M.; Zouni, A.; Saenger, W. Cyanobacterial photosystem II at 2.9 Å resolution and the role of quinones, lipids, channels and chloride. *Nat. Struct. Mol. Biol.* **2009**, *16*, 334-342.

(67) Umena, Y.; Kawakami, K.; Shen, J.-R.; Kamiya, N. Crystal structure of oxygen-evolving photosystem II at a resolution of 1.9 Å. *Nature* **2011**, *473*, 55-60.

(68) Macpherson, A. N.; Liddell, P. A.; Lin, S.; Noss, L.; Seely, G. R.; DeGraziano, J. M.; Moore, A. L.; Moore, T. A.; Gust, D. Ultrafast Photoinduced Electron Transfer in Rigid Porphyrin-Quinone Dyads. *J. Am. Chem. Soc.* **1995**, *117*, 7202-7212.

(69) Moore, T. A.; Gust, D.; Mathis, P.; Mialocq, J.-C.; Chachaty, C.; Bensasson, R. V.; Land, E. J.; Doizi, D.; Liddell, P. A.; Lehman, W. R., et al. Photodriven charge separation in a carotenoporphyrin-quinone triad. *Nature* **1984**, *307*, 630-632.

(70) Sun, L. C.; Hammarström, L.; Åkermark, B.; Styring, S. Towards artificial photosynthesis: ruthenium-manganese chemistry for energy production. *Chem. Soc. Rev.* **2001**, *30*, 36-49.

(71) Abrahamsson, M.; Jäger, M.; Österman, T.; Eriksson, L.; Persson, P.; Becker, H.-C.; Johansson, O.; Hammarström, L. A 3.0 μs Room Temperature Excited State Lifetime of a Bistridentate RuII−Polypyridine Complex for Rod-like Molecular Arrays. *J. Am. Chem. Soc.* **2006**, *128*, 12616-12617.

(72) Fukuzumi, S.; Ohkubo, K.; Suenobu, T. Long-Lived Charge Separation and Applications in Artificial Photosynthesis. *Acc. Chem. Res.* **2014**, *47*, 1455-1464.

(73) Kodis, G.; Terazono, Y.; Liddell, P. A.; Andréasson, J.; Garg, V.; Hambourger, M.; Moore, T. A.; Moore, A. L.; Gust, D. Energy and Photoinduced Electron Transfer in a Wheel-Shaped Artificial Photosynthetic Antenna-Reaction Center Complex. *J. Am. Chem. Soc.* **2006**, *128*, 1818-1827.

(74) Terazono, Y.; Kodis, G.; Liddell, P. A.; Garg, V.; Moore, T. A.; Moore, A. L.; Gust, D. Multiantenna Artificial Photosynthetic Reaction Center Complex. *J. Phys. Chem. B* **2009**, *113*, 7147-7155.

(75) Wenger, O. S. Proton-Coupled Electron Transfer with Photoexcited Metal Complexes. *Acc. Chem. Res.* **2013**, *46*, 1517-1526.

(76) Eisenhart, T. T.; Dempsey, J. L. Photo-induced Proton-Coupled Electron Transfer Reactions of Acridine Orange: Comprehensive Spectral and Kinetics Analysis. *J. Am. Chem. Soc.* **2014**, *136*, 12221-12224.

(77) Bourrez, M.; Steinmetz, R.; Ott, S.; Gloaguen, F.; Hammarström, L. Concerted proton-coupled electron transfer from a metal-hydride complex. *Nature Chem.* **2015**, *7*, 140-145.

(78) Hammarström, L. Accumulative Charge Separation for Solar Fuels Production: Coupling Light-Induced Single Electron Transfer to Multielectron Catalysis. *Acc. Chem. Res.* **2015**, *48*, 840-850.

(79) Gilbert, M.; Albinsson, B. Photoinduced Charge and Energy Transfer in Molecular Wires. *Chem. Soc. Rev.* **2015**, *44*, 845-862.

(80) Davis, W. B.; Svec, W. A.; Ratner, M. A.; Wasielewski, M. R. Molecular-Wire Behaviour in p-Phenylenevinylene Oligomers. *Nature* **1998**, *396*, 60-63.

(81) Pettersson, K.; Wiberg, J.; Ljungdahl, T.; Mårtensson, J.; Albinsson, B. Interplay between Barrier Width and Height in Electron Tunneling: Photoinduced Electron Transfer in Porphyrin-Based Donor−Bridge−Acceptor Systems. *J. Phys. Chem. A* **2005**, *110*, 319-326.

(82) Hanss, D.; Wenger, O. S. Tunneling Barrier Effects on Photoinduced Charge Transfer through Covalent Rigid Rod-Like Bridges. *Inorg. Chem.* **2008**, *48*, 671-680.

(83) Weiss, E. A.; Wasielewski, M. R.; Ratner, M. A. Molecules as wires: Molecule-assisted movement of charge and energy. In *Molecular Wires: From Design to Properties*, DeCola, L., Ed. Springer-Verlag Berlin: Berlin, 2005; Vol. 257, pp 103-133.

(84) Weiss, E. A.; Tauber, M. J.; Kelley, R. F.; Ahrens, M. J.; Ratner, M. A.; Wasielewski, M. R. Conformationally gated switching between superexchange and hopping within oligo-p-phenylene-based molecular wires. *J. Am. Chem. Soc.* **2005**, *127*, 11842-11850.

(85) Miura, T.; Carmieli, R.; Wasielewski, M. R. Time-Resolved EPR Studies of Charge Recombination and Triplet-State Formation within Donor−Bridge−Acceptor Molecules Having Wire-Like Oligofluorene Bridges. *J. Phys. Chem. A* **2010**, *114*, 5769-5778.

(86) Atienza-Castellanos, C.; Wielopolski, M.; Guldi, D. M.; van der Pol, C.; Bryce, M. R.; Filippone, S.; Martin, N. Determination of the attenuation factor in fluorene-based molecular wires. *Chem. Commun.* **2007**, 5164-5166.

(87) Ricks, A. B.; Brown, K. E.; Wenninger, M.; Karlen, S. D.; Berlin, Y. A.; Co, D. T.; Wasielewski, M. R. Exponential Distance Dependence of Photoinitiated Stepwise Electron Transfer in Donor–Bridge–Acceptor Molecules: Implications for Wirelike Behavior. *J. Am. Chem. Soc.* **2012**, *134*, 4581-4588.

(88) Pettersson, K.; Kilså, K.; Mårtensson, J.; Albinsson, B. Intersystem Crossing versus Electron Transfer in Porphyrin-Based Donor−Bridge−Acceptor Systems: Influence of a Paramagnetic Species. *J. Am. Chem. Soc.* **2004**, *126*, 6710-6719.

(89) Wiberg, J.; Guo, L.; Pettersson, K.; Nilsson, D.; Ljungdahl, T.; Mårtensson, J.; Albinsson, B. Charge Recombination versus Charge Separation in Donor−Bridge−Acceptor Systems. *J. Am. Chem. Soc.* **2006**, *129*, 155-163.

(90) Winters, M. U.; Pettersson, K.; Mårtensson, J.; Albinsson, B. Competition between Superexchange-Mediated and Sequential Electron Transfer in a Bridged Donor–Acceptor System. *Chem. Eur. J.* **2005**, *11*, 562-573.

(91) Hanss, D.; Wenger, O. S. Electron Tunneling through Oligo-p-xylene Bridges. *Inorg. Chem.* **2008**, *47*, 9081-9084.

(92) Hanss, D.; Wenger, O. S. Conformational Effects on Long-Range Electron Transfer: Comparison of Oligo-p-phenylene and Oligo-p-xylene Bridges. *Eur. J. Inorg. Chem.* **2009**, *2009*, 3778-3790.

(93) Winters, M. U.; Dahlstedt, E.; Blades, H. E.; Wilson, C. J.; Frampton, M. J.; Anderson, H. L.; Albinsson, B. Probing the Efficiency of Electron Transfer through Porphyrin-Based Molecular Wires. *J. Am. Chem. Soc.* **2007**, *129*, 4291-4297.

(94) Goldsmith, R. H.; DeLeon, O.; Wilson, T. M.; Finkelstein-Shapiro, D.; Ratner, M. A.; Wasielewski, M. R. Challenges in Distinguishing Superexchange and Hopping Mechanisms of Intramolecular Charge Transfer through Fluorene Oligomers. *J. Phys. Chem. A* **2008**, *112*, 4410-4414.

(95) Winters, M. U.; Kärnbratt, J.; Blades, H. E.; Wilson, C. J.; Frampton, M. J.; Anderson, H. L.; Albinsson, B. Control of Electron Transfer in a Conjugated Porphyrin Dimer by Selective Excitation of Planar and Perpendicular Conformers. *Chem. Eur. J.* **2007**, *13*, 7385-7394.

(96) Davis, W. B.; Ratner, M. A.; Wasielewski, M. R. Conformational Gating of Long Distance Electron Transfer through Wire-like Bridges in Donor−Bridge−Acceptor Molecules. *J. Am. Chem. Soc.* **2001**, *123*, 7877-7886.

(97) Walther, M. E.; Grilj, J.; Hanss, D.; Vauthey, E.; Wenger, O. S. Photoinduced Processes in Fluorene-Bridged Rhenium–Phenothiazine Dyads – Comparison of Electron Transfer Across Fluorene, Phenylene, and Xylene Bridges. *Eur. J. Inorg. Chem.* **2010**, *2010*, 4843-4850.

(98) Indelli, M. T.; Chiorboli, C.; Flamigni, L.; De Cola, L.; Scandola, F. Photoinduced Electron Transfer across Oligo-p-phenylene Bridges. Distance and Conformational Effects in Ru(II)−Rh(III) Dyads. *Inorg. Chem.* **2007**, *46*, 5630-5641.

(99) Welter, S.; Salluce, N.; Belser, P.; Groeneveld, M.; De Cola, L. Photoinduced electronic energy transfer in modular, conjugated, dinuclear Ru(II)/Os(II) complexes. *Coord. Chem. Rev.* **2005**, *249*, 1360-1371.

(100) Benniston, A. C.; Harriman, A.; Li, P.; Sams, C. A.; Ward, M. D. Orientational Control of Electronic Coupling in Mixed-Valence, Binuclear Ruthenium(II)−Bis(2,2‘:6‘,2‘ ‘-Terpyridine) Complexes. *J. Am. Chem. Soc.* **2004**, *126*, 13630-13631.

(101) Benniston, A. C.; Harriman, A.; Li, P.; Patel, P. V.; Sams, C. A. The effect of torsion angle on the rate of intramolecular triplet energy transfer. *Phys. Chem. Chem. Phys.* **2005**, *7*, 3677-3679.

(102) Eng, M. P.; Mårtensson, J.; Albinsson, B. Temperature Dependence of Electronic Coupling through Oligo-p-phenyleneethynylene Bridges. *Chem. Eur. J.* **2008**, *14*, 2819-2826.

(103) Eng, M. P.; Albinsson, B. The dependence of the electronic coupling on energy gap and bridge conformation – Towards prediction of the distance dependence of electron transfer reactions. *Chem. Phys.* **2009**, *357*, 132-139.

(104) Ahn, T. K.; Kim, K. S.; Kim, D. Y.; Noh, S. B.; Aratani, N.; Ikeda, C.; Osuka, A.; Kim, D. Relationship between Two-Photon Absorption and the π-

Conjugation Pathway in Porphyrin Arrays through Dihedral Angle Control. *J. Am. Chem. Soc.* **2006**, *128*, 1700-1704.

(105) Ahn, T. K.; Yoon, Z. S.; Hwang, I.-W.; Lim, J. K.; Rhee, H.; Joo, T.; Sim, E.; Kim, S. K.; Aratani, N.; Osuka, A., et al. Effect of Conformational Heterogeneity on Excitation Energy Transfer Efficiency in Directly meso−meso Linked Zn(II) Porphyrin Arrays. *J. Phys. Chem. B* **2005**, *109*, 11223-11230.

(106) Eng, M. P.; Albinsson, B. Non-Exponential Distance Dependence of Bridge-Mediated Electronic Coupling. *Angew. Chem. Int. Ed.* **2006**, *118*, 5754-5757.

(107) Eng, M. P.; Ljungdahl, T.; Mårtensson, J.; Albinsson, B. Triplet Excitation Energy Transfer in Porphyrin-Based Donor−Bridge−Acceptor Systems with Conjugated Bridges of Varying Length: An Experimental and DFT Study. *J. Phys. Chem. B* **2006**, *110*, 6483-6491.

(108) N. Taylor, P.; Huuskonen, J.; T. Aplin, R.; L. Anderson, H.; Rumbles, G.; Williams, E. Conjugated porphyrin oligomers from monomer to hexamer. *Chem. Commun.* **1998**, 909-910.

(109) Hensel, V.; Schlüter, A. D. A Cyclotetraicosaphenylene. *Chem. Eur. J.* **1999**, *5*, 421-429.

(110) Aratani, N.; Takagi, A.; Yanagawa, Y.; Matsumoto, T.; Kawai, T.; Yoon, Z. S.; Kim, D.; Osuka, A. Giant meso–meso-Linked Porphyrin Arrays of Micrometer Molecular Length and Their Fabrication. *Chem. Eur. J.* **2005**, *11*, 3389-3404.

(111) Ikeda, T.; Aratani, N.; Osuka, A. Synthesis of Extremely π-Extended Porphyrin Tapes from Hybrid meso-meso Linked Porphyrin Arrays: An Approach Towards the Conjugation Length. *Chem. Asian J.* **2009**, *4*, 1248-1256.

(112) Kondratuk, D. V.; Perdigao, L. M. A.; O'Sullivan, M. C.; Svatek, S.; Smith, G.; O'Shea, J. N.; Beton, P. H.; Anderson, H. L. Two Vernier-Templated Routes to a 24-Porphyrin Nanoring. *Angew. Chem. Int. Ed.* **2012**, *51*, 6696-6699.

(113) Liu, S.; Kondratuk, D. V.; Rousseaux, S. A. L.; Gil-Ramírez, G.; O'Sullivan, M. C.; Cremers, J.; Claridge, T. D. W.; Anderson, H. L. Caterpillar Track Complexes in Template-Directed Synthesis and Correlated Molecular Motion. *Angew. Chem. Int. Ed.* **2015**, *127*, 5445-5449.

(114) Kim, D.; Osuka, A. Directly Linked Porphyrin Arrays with Tunable Excitonic Interactions. *Acc. Chem. Res.* **2004**, *37*, 735-745.

(115) Lehn, J.-M. Toward Self-Organization and Complex Matter. *Science* **2002**, *295*, 2400-2403.

(116) Whitesides, G. M.; Grzybowski, B. Self-Assembly at All Scales. *Science* **2002**, *295*, 2418-2421.

(117) Shipman, L. L.; Cotton, T. M.; Norris, J. R.; Katz, J. J. New proposal for structure of special-pair chlorophyll. *Proc. Natl. Acad. Sci. U. S. A.* **1976**, *73*, 1791-1794.

(118) Watson, J. D.; Crick, F. H. C. A Structure for Deoxyribose Nucleic Acid. *Nature* **1953**, *171*, 737-738.

(119) Wasielewski, M. R. Self-Assembly Strategies for Integrating Light Harvesting and Charge Separation in Artificial Photosynthetic Systems. *Acc. Chem. Res.* **2009**, *42*, 1910-1921.

(120) Ahrens, M. J.; Sinks, L. E.; Rybtchinski, B.; Liu, W.; Jones, B. A.; Giaimo, J. M.; Gusev, A. V.; Goshe, A. J.; Tiede, D. M.; Wasielewski, M. R. Self-Assembly of Supramolecular Light-Harvesting Arrays from Covalent Multi-Chromophore Perylene-3,4:9,10-bis(dicarboximide) Building Blocks. *J. Am. Chem. Soc.* **2004**, *126*, 8284-8294.

(121) Rybtchinski, B.; Sinks, L. E.; Wasielewski, M. R. Combining Light-Harvesting and Charge Separation in a Self-Assembled Artificial Photosynthetic System Based on Perylenediimide Chromophores. *J. Am. Chem. Soc.* **2004**, *126*, 12268-12269.

(122) Tanaka, T.; Osuka, A. Conjugated porphyrin arrays: synthesis, properties and applications for functional materials. *Chem. Soc. Rev.* **2014**.

(123) Nakamura, Y.; Aratani, N.; Osuka, A. Cyclic porphyrin arrays as artificial photosynthetic antenna: synthesis and excitation energy transfer. *Chem. Soc. Rev.* **2007**, *36*, 831-845.

(124) Hwang, I.-W.; Cho, H. S.; Jeong, D. H.; Kim, D.; Tsuda, A.; Nakamura, T.; Osuka, A. Photophysical Properties of a Three-Dimensional Zinc(II) Porphyrin Box. *J. Phys. Chem. B* **2003**, *107*, 9977-9988.

(125) Hwang, I.-W.; Kamada, T.; Ahn, T. K.; Ko, D. M.; Nakamura, T.; Tsuda, A.; Osuka, A.; Kim, D. Porphyrin Boxes Constructed by Homochiral Self-Sorting Assembly: Optical Separation, Exciton Coupling, and Efficient Excitation Energy Migration. *J. Am. Chem. Soc.* **2004**, *126*, 16187-16198.

(126) Tsuda, A.; Hu, H.; Watanabe, R.; Aida, T. π-Conjugated multiporphyrin box via self-assembly of an ethynylene-bridged zinc porphyrin dimer. *J. Porphyrins Phthalocyanines* **2003**, *07*, 388-393.

(127) Osuka, A.; Nakajima, S.; Maruyama, K.; Mataga, N.; Asahi, T.; Yamazaki, I.; Nishimura, Y.; Ohno, T.; Nozaki, K. 1,2-Phenylene-bridged diporphyrin linked with porphyrin monomer and pyromellitimide as a model for a photosynthetic reaction center: synthesis and photoinduced charge separation. *J. Am. Chem. Soc.* **1993**, *115*, 4577-4589.

(128) Wagner, R. W.; Lindsey, J. S. A molecular photonic wire. *J. Am. Chem. Soc.* **1994**, *116*, 9759-9760.

(129) Senge, M. O.; Gerzevske, K. R.; Vicente, M. G. H.; Forsyth, T. P.; Smith, K. M. Models for the Photosynthetic Reaction Center—Synthesis and Structure of Porphyrin Dimers with cis- and trans-Ethene and Skewed Hydroxymethylene Bridges. *Angew. Chem. Int. Ed. Engl.* **1993**, *32*, 750-753.

(130) Lin, V.; DiMagno, S.; Therien, M. Highly conjugated, acetylenyl bridged porphyrins: new models for light-harvesting antenna systems. *Science* **1994**, *264*, 1105-1111.

(131) Anderson, H. L.; Martin, S. J.; Bradley, D. D. C. Synthesis and Third-Order Nonlinear Optical Properties of a Conjugated Porphyrin Polymer. *Angew. Chem. Int. Ed. Engl.* **1994**, *33*, 655-657.

(132) Lin, V. S. Y.; Therien, M. J. The Role of Porphyrin-to-Porphyrin Linkage Topology in the Extensive Modulation of the Absorptive and Emissive Properties of a Series of Ethynyl- and Butadiynyl-Bridged Bis- and Tris(porphinato)zinc Chromophores. *Chem. Eur. J.* **1995**, *1*, 645-651.

(133) Kim, D.; Osuka, A. Photophysical Properties of Directly Linked Linear Porphyrin Arrays. *J. Phys. Chem. A* **2003**, *107*, 8791-8816.

(134) Kasha, M.; Rawls, H.; El-Bayoumi, M. A. The exciton model in molecular spectroscopy. *Pure Appl. Chem.* **1965**, *11*, 371-392.

(135) Aratani, N.; Kim, D.; Osuka, A. Discrete Cyclic Porphyrin Arrays as Artificial Light-Harvesting Antenna. *Acc. Chem. Res.* **2009**, *42*, 1922-1934.

(136) Holten, D.; Bocian, D. F.; Lindsey, J. S. Probing Electronic Communication in Covalently Linked Multiporphyrin Arrays. A Guide to the Rational Design of Molecular Photonic Devices. *Acc. Chem. Res.* **2001**, *35*, 57-69.

(137) Beljonne, D.; O'Keefe, G. E.; Hamer, P. J.; Friend, R. H.; Anderson, H. L.; Brédas, J. L. Investigation of the linear and nonlinear optical response of edge-linked conjugated zinc porphyrin oligomers by optical spectroscopy and configuration interaction techniques. *J. Chem. Phys.* **1997**, *106*, 9439-9460.

(138) Anderson, H. L. Building Molecular Wires from the Colours of Life: Conjugated Porphyrin Oligomers. *Chem. Commun.* **1999**, 2323-2330.

(139) Tsuda, A.; Osuka, A. Fully Conjugated Porphyrin Tapes with Electronic Absorption Bands That Reach into Infrared. *Science* **2001**, *293*, 79-82.

(140) Khoury, T.; Crossley, M. J. A strategy for the stepwise ring annulation of all four pyrrolic rings of a porphyrin. *Chem. Commun.* **2007**, 4851-4853.

(141) Pawlicki, M.; Morisue, M.; Davis, N. K. S.; McLean, D. G.; Haley, J. E.; Beuerman, E.; Drobizhev, M.; Rebane, A.; Thompson, A. L.; Pascu, S. I., et al. Engineering conjugation in para-phenylene-bridged porphyrin tapes. *Chem. Sci.* **2012**, *3*, 1541-1547.

(142) Susumu, K.; Frail, P. R.; Angiolillo, P. J.; Therien, M. J. Conjugated Chromophore Arrays with Unusually Large Hole Polaron Delocalization Lengths. *J. Am. Chem. Soc.* **2006**, *128*, 8380-8381.

(143) Sedghi, G.; Sawada, K.; Esdaile, L. J.; Hoffmann, M.; Anderson, H. L.; Bethell, D.; Haiss, W.; Higgins, S. J.; Nichols, R. J. Single Molecule Conductance of

Porphyrin Wires with Ultralow Attenuation. *J. Am. Chem. Soc.* **2008**, *130*, 8582-8583.

(144) Sedghi, G.; Garcia-Suarez, V. M.; Esdaile, L. J.; Anderson, H. L.; Lambert, C. J.; Martin, S.; Bethell, D.; Higgins, S. J.; Elliott, M.; Bennett, N., et al. Long-Range Electron Tunnelling in Oligo-Porphyrin Molecular Wires. *Nature Nanotech.* **2011**, *6*, 517-523.

(145) Sedghi, G.; Esdaile, L. J.; Anderson, H. L.; Martin, S.; Bethell, D.; Higgins, S. J.; Nichols, R. J. Comparison of the Conductance of Three Types of Porphyrin-Based Molecular Wires: β,meso,β-Fused Tapes, meso-Butadiyne-Linked and Twisted meso-meso Linked Oligomers. *Adv. Mater.* **2012**, *24*, 653-657.

(146) Li, Z.; Park, T.-H.; Rawson, J.; Therien, M. J.; Borguet, E. Quasi-Ohmic Single Molecule Charge Transport through Highly Conjugated meso-to-meso Ethyne-Bridged Porphyrin Wires. *Nano Lett.* **2012**, *12*, 2722-2727.

(147) Haiss, W.; van Zalinge, H.; Higgins, S. J.; Bethell, D.; Höbenreich, H.; Schiffrin, D. J.; Nichols, R. J. Redox State Dependence of Single Molecule Conductivity. *J. Am. Chem. Soc.* **2003**, *125*, 15294-15295.

(148) Haiss, W.; Nichols, R. J.; van Zalinge, H.; Higgins, S. J.; Bethell, D.; Schiffrin, D. J. Measurement of single molecule conductivity using the spontaneous formation of molecular wires. *Phys. Chem. Chem. Phys.* **2004**, *6*, 4330-4337.

(149) Solomon, G. C.; Andrews, D. Q.; Van Duyne, R. P.; Ratner, M. A. When Things Are Not as They Seem: Quantum Interference Turns Molecular Electron Transfer "Rules" Upside Down. *J. Am. Chem. Soc.* **2008**, *130*, 7788-7789.

(150) Visions for a molecular future. *Nature Nanotech.* **2013**, *8*, 385-389.

(151) Hollas, J. M. *Modern Spectroscopy. Fourth Edition.* John Wiley and Sons: Hoboken, NJ, 2004.

(152) Atkins, P.; De Paula, J.; Friedman, R. *Quanta, matter, and change: a molecular approach to physical chemistry*. Oxford University Press: 2009.

(153) Balzani, V.; Ceroni, P.; Juris, A. *Photochemistry and photophysics: concepts, research, applications*. John Wiley & Sons: 2014.

(154) Balzani, V. *Electron transfer in chemistry*. WILEY-VCH Verlag GmbH: 2001.

(155) McNaught, A. D.; Wilkinson, A. *IUPAC. Compendium of Chemical Terminology, 2nd ed. (the "Gold Book").* 2nd ed.; Blackwell Scientific Publications: Oxford, 1997.

(156) Lakowicz, J. R. *Principles of Fluorescence Spectroscopy. Third Edition*. Springer: New-York, NY, 2006.

(157) Kasha, M. Characterization of electronic transitions in complex molecules. *Farad. Discuss.* **1950**, *9*, 14-19.

(158) Huppert, D.; Jortner, J.; Rentzepis, P. M. S2 → S1 emission of azulene in solution. *Chem. Phys. Lett.* **1972**, *13*, 225-228.

(159) Kurabayashi, Y.; Kikuchi, K.; Kokubun, H.; Kaizu, Y.; Kobayashi, H. S2 → S0 fluorescence of some metallotetraphenylporphyrins. *J. Phys. Chem.* **1984**, *88*, 1308-1310.

(160) Kobayashi, N.; Lever, A. B. P. Cation or solvent-induced supermolecular phthalocyanine formation: crown ether substituted phthalocyanines. *J. Am. Chem. Soc.* **1987**, *109*, 7433-7441.

(161) Libby, W. F. Theory of Electron Exchange Reactions in Aqueous Solution. *J. Phys. Chem.* **1952**, *56*, 863-868.

(162) Marcus, R. A. On the Theory of Oxidation-Reduction Reactions Involving Electron Transfer. I. *J. Chem. Phys.* **1956**, *24*, 966-978.

(163) Marcus, R. A. On the Theory of Electron-Transfer Reactions. VI. Unified Treatment for Homogeneous and Electrode Reactions. *J. Chem. Phys.* **1965**, *43*, 679-701.

(164) Marcus, R. A. Exchange reactions and electron transfer reactions including isotopic exchange. Theory of oxidation-reduction reactions involving electron transfer. Part 4.-A statistical-mechanical basis for treating contributions from solvent, ligands, and inert salt. *Farad. Discuss.* **1960**, *29*, 21-31.

(165) Miller, J. R.; Calcaterra, L. T.; Closs, G. L. Intramolecular long-distance electron transfer in radical anions. The effects of free energy and solvent on the reaction rates. *J. Am. Chem. Soc.* **1984**, *106*, 3047-3049.

(166) Closs, G. L.; Miller, J. R. Intramolecular Long-Distance Electron Transfer in Organic Molecules. *Science* **1988**, *240*, 440-447.

(167) Weller, A. Photoinduced Electron Transfer in Solution: Exciplex and Radical Ion Pair Formation Free Enthalpies and their Solvent Dependence. *Zeitschrift für Physikalische Chemie* **1982**, *133*, 93-98.

(168) Hilgendorff, M.; Sundström, V. Ultrafast electron injection and recombination dynamics of dye sensitised TiO2 particles. *Chem. Phys. Lett.* **1998**, *287*, 709-713.

(169) McConnell, H. M. Intramolecular Charge Transfer in Aromatic Free Radicals. *J. Chem. Phys.* **1961**, *35*, 508-515.

(170) Anderson, P. W. New approach to the theory of superexchange interactions. *Phys. Rev.* **1959**, *115*, 2-13.

(171) Halpern, J.; Orgel, L. E. The Theory of Electron Transfer between Metal Ions in Bridged Systems. *Discuss. Faraday Soc.* **1960**, 32-41.

(172) Berlin, Y. A.; Hutchison, G. R.; Rempala, P.; Ratner, M. A.; Michl, J. Charge Hopping in Molecular Wires as a Sequence of Electron-Transfer Reactions. *J. Phys. Chem. A* **2003**, *107*, 3970-3980.

(173) Berlin, Y. A.; Burin, A. L.; Ratner, M. A. Elementary steps for charge transport in DNA: thermal activation vs. tunneling. *Chem. Phys.* **2002**, *275*, 61-74.

(174) Paulson, B. P.; Miller, J. R.; Gan, W. X.; Closs, G. Superexchange and sequential mechanisms in charge transfer with a mediating state between the donor and acceptor. *J. Am. Chem. Soc.* **2005**, *127*, 4860-4868.

(175) McConnell, H. Intramolecular Charge Transfer in Aromatic Free Radicals. *J. Chem. Phys.* **1961**, *35*, 508-515.

(176) Paddon-Row, M. N.; Oliver, A. M.; Warman, J. M.; Smit, K. J.; De Haas, M. P.; Oevering, H.; Verhoeven, J. W. Factors affecting charge separation and recombination in photoexcited rigid donor-insulator-acceptor compounds. *J. Phys. Chem.* **1988**, *92*, 6958-6962.

(177) Förster, T. Energiewanderung und Fluoreszenz. *Naturwissenschaften* **1946**, *33*, 166-175.

(178) Förster, T. Zwischenmolekulare Energiewanderung und Fluoreszenz. *Annalen der Physik* **1948**, *437*, 55-75.

(179) Andrews, D. L.; Li, S.; Rodriguez, J.; Slota, J. Development of the energy flow in light-harvesting dendrimers. *J. Chem. Phys.* **2007**, *127*, 134902.

(180) Dexter, D. L. A Theory of Sensitized Luminescence in Solids. *J. Chem. Phys.* **1953**, *21*, 836-850.

(181) de Grotthuss, C. J. T. Sur la décomposition de l'eau et des corps qu'elle tient en dissolution à l'aide de l'électricité galvanique. *Ann. Chim.* **1806**, *58*, 54-73.

(182) Stokes, G. G. On the Change of Refrangibility of Light. *Philosophical Transactions of the Royal Society of London* **1852**, *142*, 463-562.

(183) Strickler, S. J.; Berg, R. A. Relationship between Absorption Intensity and Fluorescence Lifetime of Molecules. *J. Chem. Phys.* **1962**, *37*, 814-822.

(184) Kubista, M.; Sjoback, R.; Eriksson, S.; Albinsson, B. Experimental correction for the inner-filter effect in fluorescence spectra. *Analyst* **1994**, *119*, 417-419.

(185) Moulton, P. Ti-doped Sapphire Tunable Solid State Laser. *Opt. News* **1982**, 9.

(186) "for his studies of the transition states of chemical reactions using femtosecond spectroscopy","The Nobel Prize in Chemistry 1999". http://www.nobelprize.org/nobel_prizes/chemistry/laureates/1999 (accessed 25 March 2015).

(187) Silfvast, W. T. *Laser Fundamentals*. 2nd ed.; Cambridge University Press: 2008.

(188) Komura, M.; Itoh, S. Fluorescence measurement by a streak camera in a single-photon-counting mode. *Photosynth. Res.* **2009**, *101*, 119-133.

(189) Brocklehurst, B.; Young, R. N. Fluorescence anisotropy decays and viscous behaviour of 2-methyltetrahydrofuran. *J. Chem. Soc., Faraday Trans.* **1994**, *90*, 271-278.

(190) Winters, M. U.; Kärnbratt, J.; Eng, M.; Wilson, C. J.; Anderson, H. L.; Albinsson, B. Photophysics of a Butadiyne-Linked Porphyrin Dimer: Influence of Conformational Flexibility in the Ground and First Singlet Excited State. *J. Phys. Chem. C* **2007**, *111*, 7192-7199.

(191) Kuciauskas, D.; Liddell, P. A.; Lin, S.; Stone, S. G.; Moore, A. L.; Moore, T. A.; Gust, D. Photoinduced Electron Transfer in Carotenoporphyrin−Fullerene Triads: Temperature and Solvent Effects. *J. Phys. Chem. B* **2000**, *104*, 4307-4321.

(192) Kang, Y. K.; Duncan, T. V.; Therien, M. J. Temperature-Dependent Mechanistic Transition for Photoinduced Electron Transfer Modulated by Excited-State Vibrational Relaxation Dynamics. *J. Phys. Chem. B* **2007**, *111*, 6829-6838.

(193) Lemmetyinen, H.; Tkachenko, N. V.; Efimov, A.; Niemi, M. Temperature Independent Ultrafast Photoinduced Charge Transfer in Donor−Acceptor Pairs Forming Exciplexes. *J. Phys. Chem. C* **2009**, *113*, 11475-11483.

(194) Scott, A. M.; Wasielewski, M. R. Temperature Dependence of Spin-Selective Charge Transfer Pathways in Donor−Bridge−Acceptor Molecules with Oligomeric Fluorenone and p-Phenylethynylene Bridges. *J. Am. Chem. Soc.* **2011**, *133*, 3005-3013.

(195) Kahnt, A.; Kärnbratt, J.; Esdaile, L. J.; Hutin, M.; Sawada, K.; Anderson, H. L.; Albinsson, B. Temperature Dependence of Charge Separation and Recombination in Porphyrin Oligomer–Fullerene Donor–Acceptor Systems. *J. Am. Chem. Soc.* **2011**, *133*, 9863-9871.

(196) Rohmer, M.-M.; Veillard, A.; Wood, M. H. Excited states and electronic spectrum of ferrocene. *Chem. Phys. Lett.* **1974**, *29*, 466-468.

(197) Armstrong, A. T.; Smith, F.; Elder, E.; McGlynn, S. P. Electronic Absorption Spectrum of Ferrocene. *J. Chem. Phys.* **1967**, *46*, 4321-4328.

(198) Helms, A.; Heiler, D.; McLendon, G. Dependence of electron transfer rates on donor-acceptor angle in bis-porphyrin adducts. *J. Am. Chem. Soc.* **1991**, *113*, 4325-4327.

(199) Hoffmann, M.; Wilson, C. J.; Odell, B.; Anderson, H. L. Template-Directed Synthesis of a π-Conjugated Porphyrin Nanoring. *Angew. Chem. Int. Ed.* **2007**, *46*, 3122-3125.

(200) Scheibe, G. *Angew. Chem.* **1936**, *49*, 563.

(201) Jelley, E. E. Spectral Absorption and Fluorescence of Dyes in the Molecular State. *Nature* **1936**, *138*, 1009-1010.

(202) Hunter, C. A.; Meah, M. N.; Sanders, J. K. M. Dabco-metalloporphyrin binding: ternary complexes, host-guest chemistry and the measurement of .pi.-.pi. interactions. *J. Am. Chem. Soc.* **1990**, *112*, 5773-5780.

(203) Hoffmann, M.; Karnbratt, J.; Chang, M. H.; Herz, L. M.; Albinsson, B.; Anderson, H. L. Enhanced pi conjugation around a porphyrin 6 nanoring. *Angewandte Chemie-International Edition* **2008**, *47*, 4993-4996.

(204) Kuhlbrandt, W.; Wang, D. N.; Fujiyoshi, Y. Atomic model of plant light-harvesting complex by electron crystallography. *Nature* **1994**, *367*, 614-621.

(205) McDermott, G.; Prince, S. M.; Freer, A. A.; Hawthornthwaite-Lawless, A. M.; Papiz, M. Z.; Cogdell, R. J.; Isaacs, N. W. Crystal structure of an integral membrane light-harvesting complex from photosynthetic bacteria. *Nature* **1995**, *374*, 517-521.

(206) Watanabe, S.; Shimodo, Y.; Morihashi, K. Theoretical investigation of hole mobility in 9,10-diphenylanthracene by density functional calculations. *Theor. Chem. Acc.* **2011**, *130*, 807-813.

(207) Hernando, J.; Hoogenboom, J. P.; van Dijk, E. M. H. P.; García-López, J. J.; Crego-Calama, M.; Reinhoudt, D. N.; van Hulst, N. F.; García-Parajó, M. F. Single Molecule Photobleaching Probes the Exciton Wave Function in a Multichromophoric System. *Phys. Rev. Lett.* **2004**, *93*, 236404.

(208) Suzuki, K.; Kobayashi, A.; Kaneko, S.; Takehira, K.; Yoshihara, T.; Ishida, H.; Shiina, Y.; Oishi, S.; Tobita, S. Reevaluation of absolute luminescence quantum yields of standard solutions using a spectrometer with an integrating sphere and a back-thinned CCD detector. *Phys. Chem. Chem. Phys.* **2009**, *11*, 9850-9860.

(209) Bright, F. V.; McGown, L. B. Three-component determinations using fluorescence anisotropy measurements and wavelength selectivity. *Anal. Chem.* **1986**, *58*, 1424-1427.

(210) Valeur, B.; Weber, G. Resolution of the fluorescence excitation spectrum of indole into the ^1L_a and ^1L_b excitation bands. *Photochem. Photobiol.* **1977**, *25*, 441-444.

(211) Johnson, B. S.; Ediger, M. D.; Yamaguchi, Y.; Matsushita, Y.; Noda, I. Concentration and temperature dependence of molecular motions in polystyrene/tetrahydrofuran solutions. *Polymer* **1992**, *33*, 3916-3924.

(212) Sukegawa, J.; Schubert, C.; Zhu, X.; Tsuji, H.; Guldi, D. M.; Nakamura, E. Electron Transfer through Rigid Organic Molecular Wires Enhanced by Electronic and Electron–Vibration Coupling. *Nature Chem.* **2014**, *6*, 899-905.